



Title	Investigation of Corium/debris field behavior for Decommissioning and Nuclear Safety Assessment
Author(s)	SAHBOUN, Nassim Florian
Citation	北海道大学. 博士(工学) 甲第14231号
Issue Date	2020-09-25
DOI	10.14943/doctoral.k14231
Doc URL	<a href="http://hdl.handle.net/2115/79784">http://hdl.handle.net/2115/79784</a>
Type	theses (doctoral)
File Information	SAHBOUN_Nassim_Florian.pdf



[Instructions for use](#)

# Investigation of Corium/debris field behavior for Decommissioning and Nuclear Safety Assessment

*A Thesis*

*Submitted by*

**Nassim Florian Sahboun**

*For the degree's award*

*Of*

**Doctor of Philosophy**

*In Engineering*

**Division of Energy and Environmental System**

**Laboratory of Nuclear System Safety**

**June 2020**

**Supervised by Prof. Kazuhiro SAWA**

## **Abstract**

One of the most severe accidents for Nuclear Power Plants (NPPs) is called a Loss of Coolant Accident (LOCA). During this kind of accident, the water used to cool down the reactor core is lost. If this coolability is not restored, it often ends with the meltdown of the reactor fuel into what is called, in the Nuclear Energy field, corium. This corium is a mixture of molten steel structure components, and molten fuel debris. Under the effect of its weight, it tends to re-locate to the bottom of the Reactor Pressure Vessel (RPV). If not properly cool when it is there, the corium will melt-through the RPV metallic layer and will spread out of it in the form of a molten material jet. From there, it will impinge and spread on the Primary Containment Vessel (PCV) concrete structures that can be found under the RPV. Thus, the present study focuses on investigating the jet's formation and impingement phenomena involved in such kind of scenario. The purpose of this study is to provide insightful information that will help to improve the Nuclear Safety Assessment and Decommissioning for this accidental scenario.

Firstly, working on the Decommissioning part of the subject, the present study treats the case of Fukushima Daichi Nuclear Power Plant (NPP) and its debris removal project. The project's purpose was to determine the heat transfer and temperature's profile of the reactor building during the 2011's accident, through the use of simulations. This knowledge will allow us to know how deep the radioactive contamination is in the different concrete structures inside the reactor building. The simulation's results revealed that deep contamination, roughly 25 cm depth, is expected in the concrete structure directly under the RPV. As for the other concrete structures, it was found that only superficial radioactive contamination is expected in those areas. This information will help the debris removal planning and also, the decommissioning of Fukushima Daiichi.

Through the above project, it was found that the simulation's results were highly dependent on the debris field geometry used. That geometry was built according to data provided by Tokyo Electric Company (TEPCO) and generated by accidental simulation software, introducing inaccuracy through the assumption using in this software. From that

assessment, it was assumed that a way to improve those simulations will be to deepen the knowledge on debris field formation. Therefore, the present study secondly focuses on creating a formulation which predicts the debris field formation accurately. Through the experimental work realized here, it was possible to build formulation for the maximum spreading ratio  $\xi_{max}$  and finger number  $N$ . Their uses to predict accurately the debris field geometry. In addition, simulations were built to investigate the key parameters for debris field formation simulation. From them, it was found that the surface roughness is a detrimental key parameter for such simulations.

Therefore, through these two works, it was possible to find insightful information that both help the Nuclear Safety Assessment and Decommissioning as they provide new and highly valuable information on debris field formation.

*Keyword: Nuclear safety; CFD; Fuel debris, Heat transfer characteristic, Fukushima NPP, Decommissioning; molten metal; severe accident; rapid solidification*

Thesis Supervisor: Kazuhiro SAWA

Title: Professor

# Acknowledgement

I would like to thank the following people who have helped me undertake this research:

My supervisors Prof. K. Sawa, Assistant Prof. S. Miwa for their enthusiasm for the project, for their supports, encouragement, and patience.

Hokkaido University e3 program and e3 staff members

For their contributions to data collection:

Assistant Prof. Y. Yamamoto, Mr. Y. Watanabe and Mr. T. Ito.

My dear lovely little wife Akari, my family, and her family.

My parents, who set me off on the road to this a long time ago.

And finally, Mr. Matthew Mercer and his team, for their critical role during my long nights working on simulations

## List of Abbreviation

CFD	Computational Fluid Dynamics
VOF	Volume of Fluid
TMI	Three Mile Island
NPP	Nuclear Power Plant
LWR	Light Water Reactor
BWR	Boiling Water Reactor
PWR	Pressurized Water Reactor
PCV	Primary Containment Vessel
RPV	Reactor Pressure Vessel
2D	Two Dimensional
3D	Three Dimensional
KHI	Kelvin-Helmholtz Instability
FCI	Fuel-Coolant Interaction
MCCI	Molten Core-Concrete Interaction
INES	International Nuclear Event Scale
IRID	International Research Institute for Nuclear Decommissioning
TEPCO	Tokyo Electric Power Company
JPDR	Japan Power Demonstration Reactor
LOCA	Loss of Coolant Accident

# Table of Contents

Contents	
<b>Abstract</b> .....	2
<b>Acknowledgement</b> .....	4
<b>List of Abbreviation</b> .....	5
<b>Table of Contents</b> .....	6
<b>List of Figures</b> .....	8
<b>List of Tables</b> .....	11
<b>Chapter 1: Introduction</b> .....	14
<b>Chapter 2: Literature Review</b> .....	16
1. Introduction .....	16
2. Spreading phenomena in the case of corium loss event.....	20
a. Previous experiments on corium spreading.....	20
b. Dominant factors .....	23
c. Models and scaling analysis.....	26
3. Jet Breakup and Fragmentation phenomena in the case of corium loss event.....	30
a. Jet breakup and Fragmentation previous experiments .....	30
b. Dominant factors .....	35
c. Models and scaling analysis.....	38
4. Solidification phenomena in the case of corium loss event .....	40
a. Previous solidification experiments .....	41
b. Solidification impact on fragmentation modeling .....	43
<b>Chapter 3: TEPCO Project</b> .....	51
1. Introduction .....	51

2. Targeted area and simulation set-up.....	54
3. Results and Discussion .....	63
<b>Chapter 4: Experimental Work .....</b>	<b>68</b>
1. Introduction .....	68
2. Experimental Conditions Description .....	74
3. Maximum Spreading Ratio of Molten Metal.....	77
<b>Chapter 5: Simulation Work.....</b>	<b>97</b>
1. Introduction .....	97
2. Simulation Model Description .....	101
3. Results and Discussion .....	110
4. Optional models and Prediction Enhancement .....	119
<b>Conclusions and Future Directions .....</b>	<b>125</b>



## List of Figures

Fig 2.1	Illustration of the different phenomena involved in Corium formation: (a) NPP in normal condition, (b) Melt down and Corium spreading out of the RPV, (c) Melt down and Corium spreading out of the RPV into coolant (Mitsuda et al. 2019).	17
Fig 2.2	(a) Optical micrograph of tin debris from MISTEE test and (b) optical micrograph of PREMIX 18 debris showing angular and spherical pieces. (Tyrprekl et al. 2014)	36
Fig 2.3	Ideal melt fragmentation into droplets (left); melt fragmentation into droplets including possible breakup after melt solidification into angular pieces (right). (Tyrprekl et al. 2014)	37
Fig 2.4	Schematic of linear stability model, including solidification effects. Crust formation at the melt jet-coolant interface (Iwasawa et al. 2015).	44
Fig 2.5	Calculated temporal growth rate against wavelength: (a) Kelvin-Helmholtz instability, (b) solidification effects (Iwasawa et al., 2015).	49
Fig 2.6	Calculated variations in wavelength against relative velocity, and effects of bending stiffness (Nm) (Iwasawa et al., 2015).	50
Fig 3.1	CFD Model for the Current Study (Mitsuda et al. 2019).	54
Fig 3.2	3D Perspective Figure of the Fuel debris (Mitsuda et al. 2019).	55
Fig 3.3	Decay Heat Evolution registered by TEPCO through the F1 Accident (Mitsuda et al. 2019).	57
Fig 3.4	Temperature profiles of the F1 accident simulations	64

Fig 3.5	Probe lines Conceptual scheme	65
Fig 3.6	Temperature profiles for bottom concrete and lateral concrete	65
Fig 3.7	Temperature profiles for lateral concrete at different height along the PCV	67
Fig 4.1	Schematic of the test section for molten metal spread experiment (Matsumoto et al. 2017, Ogura et al. 2018a and b, Sahboun et al. 2020)	72
Fig 4.2	Pictorial view of the test section for molten metal spread experiment (Matsumoto et al. 2017, Ogura et al. 2018a and b, Sahboun et al. 2020)	72
Fig 4.3	Lateral view of the experiment recording (Sahboun et al. 2020)	76
Fig 4.4	Schematic of jet impingement on solid surface (Sahboun et al. 2020)	80
Fig 4.5	Prediction assessment of the different maximum spreading ratio formulations for Copper cases ( $D_n = D_0$ ) (Sahboun et al. 2020)	83
Fig 4.6	Prediction assessment of the different maximum spreading ratio formulations for Tin cases ( $D_n = D_0$ ) (Sahboun et al. 2020)	86
Fig 4.7	Tin Spreading Sample (Sahboun et al. 2020)	89
Fig 4.8	Prediction assessment of the finger number formulations for Copper cases (Sahboun et al. 2020)	91
Fig 4.9	Prediction assessment of the different maximum spreading ratio formulations for Tin cases ( $D_n = D_0$ )	93

Fig 4.10	Prediction assessment of the different maximum spreading ratio formulations for Copper cases ( $D_n = D_0$ )	94
Fig 4.11	Recoil as a function of the accidental coefficient ( $D_n = D_0$ )	95
Fig 5.1	Schematic of the test section for molten metal spread experiment (Matsumoto et al. 2017, Ogura et al. 2018a and b, Sahboun et al. 2020)	98
Fig 5.2	Pictorial view of the test section for molten metal spread experiment (Matsumoto et al. 2017, Ogura et al. 2018a and b, Sahboun et al. 2020)	103
Fig 5.3	Volume Mesh used for Simulation	103
Fig 5.4	Experimental Spreading transient	111
Fig 5.5	Simulations Volume fraction results	112
Fig 5.6a	Comparison between experimental and simulation spreading for Sn	115
Fig 5.6b	Comparison between experimental and simulation spreading for Cu	117
Fig 5.7	Example of splashing through simulation (circled in red).	118

## List of Tables

Table 2.1	Experimental studies on melt spreading	21
Table 2.2	Code for melt spreading simulation (Dinh et al. 2000)	26
Table 2.3	Previous scaling-related considerations (Dinh et al. 2000)	28
Table 2.4	Parameter B (Dinh et al. 2000)	30
Table 2.5	Previous experiments on FCI using oxide/water pairing (Iwasawa and Abe 2018)	32
Table 2.6	Previous experiments on FCI using metal/water pairing (Iwasawa and Abe 2018)	34
Table 2.7	Previous experiments on FCI using other simulant pairing (Iwasawa and Abe 2018)	35
Table 2.8	Previous experiments on solidification effects during FCI (Iwasawa and Abe 2018)	41
Table 3.1	Simulation Set-up (Mitsuda et al. 2019).	57
Table 3.2	Thermo-physical properties under normal pressure when temperature dependence is not considered (Analysis I) (Mitsuda et al. 2019).	59
Table 3.3	Thermo-physical properties of solid at normal pressure (Mitsuda et al. 2019).	59
Table 3.4	Thermo-physical properties of liquid and gas under normal pressure (Mitsuda et al. 2019).	60
Table 3.5	Boundary Condition of Cooling Water and Nitrogen (Analysis I, II) (Mitsuda et al. 2019).	61
Table 3.6	Inflow / outflow locations of stagnant water and nitrogen (Mitsuda et al. 2019).	62

Table 3.7	Simulation Discretization Error Calculations (Mitsuda et al. 2019).	63
Table 4.1	Experimental programs on molten metal spreading (Sahboun et al. 2020)	73
Table 4.2	Experimental parameters for molten metal experiment. (Sahboun et al. 2020)	75
Table 4.3a	Jet-breakup length formulation error assessment for $C = 8.51$ (Tested material: Tin, $D_0 = 4$ mm, $H = 300$ mm, $m_d = 0.35$ kg) (Sahboun et al. 2020)	77
Table 4.3b	Jet-breakup length formulation error assessment for $C = 8.51$ (Tested material: Copper, $D_0 = 4$ mm, $H = 300$ mm, $m_d = 0.35$ kg) (Sahboun et al. 2020)	78
Table 4.4	Experimental coefficient for the empirical function $g_2$ (Sahboun et al. 2020)	87
Table 4.5	Finger formation assessment for $D_0 = 0.004$ m and $m_d = 0.4$ kg (Sahboun et al. 2020)	90
Table 5.1	Experimental programs on molten metal spreading (Dinh et al, 2000)	99
Table 5.2	Experimental parameters for molten metal experiment (Sahboun et al. 2020)	102
Table 5.3	Molten metal spreading Simulation Set-up	104
Table 5.4a	Physical Properties Simulation Set-up for Copper (Cu)	109
Table 5.4b	Physical Properties Simulation Set-up for Tin (Sn)	109
Table 5.5	Simulation Discretization Error Calculations	113

Table 5.6a	Comparison of Maximum Spreading and Thickness between experiments and simulations for Tin (Sn)	114
Table 5.6b	Comparison of Maximum Spreading and Thickness between experiments and simulations for Copper (Cu)	116
Table 5.7	Preliminary results for Jet Breakup Simulation	117
Table 5.8	Model Applicability Ranges	123

# Chapter 1: Introduction

As past events have shown, severe accidents in Nuclear Power Plants (NPPs) often end with the meltdown of the reactor fuel into what is called, in the Nuclear Energy field, corium, a mixture of molten steel structure components and molten fuel debris. As it is the responsibility of the NPP's owner to assure the safety of the population, knowing how the corium will behave, keep it properly contained and cooled, was and still is a prime concern in the Nuclear Energy field. Through the years, research emphasis was put on investigating the corium behavior in the case of a Reactor Pressure Vessel (RPV) melt through. In such a scenario, a wild array of phenomena can be observed and are detrimental for safety assessment and decommissioning such as the molten corium jet formation, its spreading behavior, or fragmentation if an encounter with coolant occurs, its solidification and behavior under confinement.

The purpose of the present study is to improve the decommissioning of damaged NPP, such as Fukushima Daichi, and Nuclear Safety assessment. Through the joined project with TEPCO, it was found that the debris field geometry plays an important part for this purpose. Therefore, the focus of this study was narrowed down to investigate the debris field formation and its geometry. To realize that objective, the work was divided into two parts. First, through experiments, the investigation focuses on providing formulations that will help predict with higher accuracy the debris field geometry, especially its maximum spreading length. Second, through simulations, the investigation attempts to provide insights on the key parameters for debris field formation simulations. Thus, the scope of the present study, to investigate the debris field formation through experiments and simulations, is divided into four chapters.

In chapter 2, a literature review of a selected number of phenomena is provided. The phenomena presented are all impacting the corium behavior and the debris field formation in the case of an RPV's melt-through. The focus was especially put on the jet formation, jet breakup, spreading, fragmentation, and solidification of the corium after such an event.

From there, the goal was to provide the background necessary for the next chapters of this study.

As a special assignment, chapter 3 presents the collaboration project with the Tokyo Electric Power Company (TEPCO) for Fukushima Daichi's decommissioning. To help the decommissioning effort, the project aims to gain knowledge of the thermal behavior of the reactor build through the accident. This knowledge is critical as it will allow knowing how deep is the radioactive contamination inside the concrete surrounding the reactor core. Through the use of simulations built with the commercial CFD software Star CCM+, temperature profiles for the reactor building were obtained that will help Fukushima's decommissioning. Moreover, as mentioned earlier, this project allows us to underline the importance of the debris field geometry and its accurate definition for Decommissioning and Safety Assessment.

In chapter 4, the focus was put on formulating an expression that could be of use for the Nuclear Safety Assessment and Decommissioning in the case of a previously mentioned scenario. To realize this objective, the previously mentioned experimental data was used to devise formulations of the used simulants maximum spreading ratio and finger number in a way suitable for this purpose.

In chapter 5, the focus was put on gaining insights on the key parameters for debris field formation simulations. With the use of Star CCM+, molten metal jet simulations were built and compared to experimental data where Copper and Tin were used as corium's simulants. From that comparison, the key parameter was found as well as potential improvements for such kind of simulations.



## Chapter 2: Literature Review

### 1. Introduction

Following the tragic event of the Fukushima Daiichi Nuclear Power Plant accident, the nuclear industry had to review and improve the safety standard in the case of such a severe accident. Numerous studies were and are still conducted at the present day to realize this important objective, such as a study on the coolability of the molten reactor core or the loss of the confinement function (Sehgal et al. 2006,2012,2016). However, the Fukushima events have shown that it is critical to deepen and re-evaluate the phenomena surrounding the loss of confinement and more precisely, the release of corium outside the reactor vessel. Such event is one of the consequences of a severe accident where the molten corium penetrates through the lower section of the Reactor Pressure Vessel (RPV) and will be released in the lower section of the reactor building. In such a case, the resulting corium jet will impinge on a concrete surface, spread over it and will interact with the concrete and the coolant used in the Nuclear Power Plant (NPP), threatening the structural integrity (Ma et al. 2016, Sehgal et al. 2016, Suzuki et al 2014, Tobita et al. 2016). Therefore, safety assessment should take into account for the jet and spread behavior of the corium in this scenario and assure that a sustainable cooling is performed on the resulting debris bed (Dinh et al. 1999, 2000).

As explained in the previous paragraph, the investigated event can be split into three sequences where sequence 1 would be the jet formation, sequence 2 the jet impact on the spreading surface or in the coolant and sequence 3 the spreading of the dedicated area with or without coolant. Therefore, the different points of interest would be the jet breakup before or after its encounter with the coolant, the spreading over the targeted area and the potential jet fragmentation in the coolant as shown in Fig 2.1.

From this assessment, the main phenomena behind such accident can be classified into two types: (1) jet instabilities and/or the jet fragmentation, and (2) corium spreading. As this division seems simple and obvious, there is an issue that arises in the midst of it as

those phenomena are known to be complex as they involve simultaneously hydrodynamic and thermal interactions (Chu et al. 1995, Sugiyama et al. 1999, Nishimura et al. 2010, Manickam et al. 2017).

As such, through the years, experiments were carried out using a wild array of melt, coolant, spreading conditions and geometries. The present review is aimed to summarize experimental works done so far on corium loss event in the case of Boiling Water Reactor (BWR) and Pressurized Water Reactor (PWR). Based on a thorough literature survey, this article aims to present the dominant factors on the phenomena involved, methodology devised for scaling and prediction.

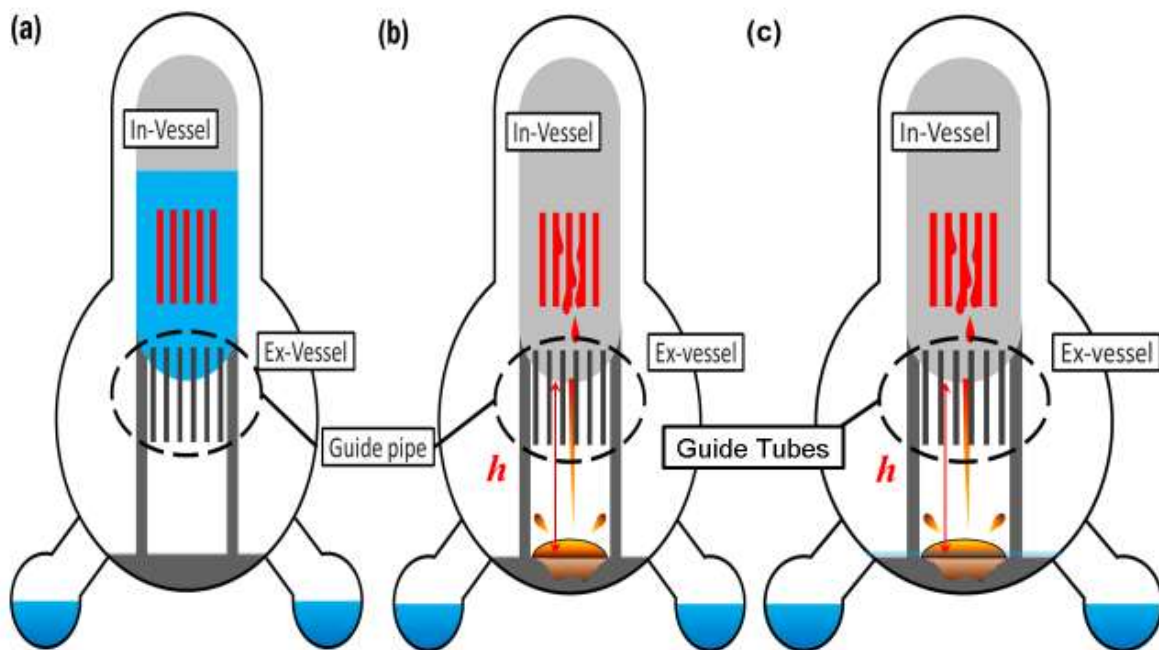


Fig 2.1. Illustration of the different phenomena involved in Corium formation: (a) NPP in normal condition, (b) Melt down and Corium spreading out of the RPV, (c) Melt down and Corium spreading out of the RPV into coolant (Mitsuda et al. 2019).

The remaining parts are organized as follow. In section 2, a review and summary of the past experiments on corium spreading will be provided. Section 3 focuses on the

discovered dominant factors on this phenomenon. Section 4 will aboard the models and scaling method for the spreading main characteristics. Finally, section 5 will be the conclusion of this present review.

## Nomenclature

- A Experimental corrective coefficient for molten metal spreading in two-dimensional channel
- B Experimental corrective coefficient for molten metal spreading from a 1D channel to an open area
- C Experimental coefficient for molten metal spreading
- $C_v$  Experimental coefficient for molten metal spreading with viscous effects
- $C_\alpha$  Experimental coefficient for molten metal spreading in open channel where  $\alpha$  is the channel opening angle
- d Characteristic length
- D Bending stiffness
- $D_j$  Jet Diameter
- $D_{frag}$  Fragment Diameter
- E Young's modulus
- $E_0$  Entrainment coefficient
- Fr Froude number
- g Gravitational acceleration
- k Wave number
- L Dimensionless length
- $L^*$  Modified dimensionless length

$L_{brk}$	Jet-breakup length
$N$	Dimensionless viscous number
$P$	Pressure
$t$	Time
$T$	Dimensionless time scale
$T^*$	Modified dimensionless time scale
$T_i$	Initial interfacial temperature
$\Delta T_c$	Coolant subcooling
$u$	Velocity fluctuation in the horizontal direction
$U$	Velocity average in the horizontal direction
$v$	velocity fluctuation in the vertical direction
$V$	Velocity average in the vertical direction
$v_j$	Jet velocity
$v_{rel}$	Relative velocity
$We$	Weber number
$We_{crit}$	Critical Weber number
$x$	Horizontal direction
$y$	Vertical direction

Greek symbol

$\delta$	Crust thickness
$\varepsilon$	Poisson's ratio

$\gamma_t$	Temporal growth rate
$\gamma_s$	Spatial growth rate
$\phi$	Velocity potential
$\eta$	Interfacial displacement
$\kappa$	Thermal conductivity
$\lambda$	Wavelength
$\lambda_n$	Neutral stable wavelength
$\lambda_m$	Most unstable wavelength
$\rho$	Density
$\sigma$	Interfacial tension or surface tension
$\omega$	Angular frequency

Subscript

0	Initial
j, 1	Melt jet
c, 2	Coolant

2. Spreading phenomena in the case of corium loss event

a. Previous experiments on corium spreading

Past and current experimental programs on corium spreading were and are still conducted to obtain insights into the involved physics and provided data to support model development, simulation building and scaling analysis. Past experiments regroup the following programs: BNL (Greene et al. 1988), SPREAD (Suzuki et al. 1993), CORINE (Veteau et al. 1994,2003), VULCANO (Cognet et al. 1994, Journeau et al. 2003, Journeau

et al. 2006), KATS/ECOKATS (Fieg et al. 1996, Foit et al. 2002,2004 and 2006), COMAS (Steinwarz et al. 1997,2001), FARO (Morris et al. 1997, Cognet et al., 2001), JRC Ispra (Magallon et al. 1997) and RIT/S3E (Sehgal et al. 1997). More recent works included VESTA (Kim et al. 2003 to 2016) and the various projects held at the Faculty of Engineering, Hokkaido University (Kobayashi et al. 2014, Matsumoto et al. 2017, Miwa et al. 2017, Ogura et al. 2018a, b). All of them are summarized in the Table 2.1 for more practicality.

Program/Facility	Country	Geometry	Melt	Temperature	Type of study cases
BNL	USA	2D area	Pb	Low	Dry, wet
SPREAD	Japan	1D, 2D area	Thermite	High	Dry
CORINE	France	2D-channel	Simulants	Low	Dry, wet
VULCANO	France	2D-channel	Corium	High	Dry
KATS	Germany	1D	Thermite	High	Dry, wet
COMAS	Germany	1D,2D-channel	Corium	High	Dry
ISPRA	EU JRC	2D-channel	Corium	High	Dry
S3E	Sweden	1D, 2D area	Simulants	Low to high	Dry, wet
VESTA	Korea	3D volume	Corium	High	Dry, wet
Hokkaido University	Japan	3D volume	Simulants	Low	Dry, wet

Table 2.1: Experimental studies on melt spreading

The BNL experimental program was performed by Greene et al. in 1988 at the Brookhaven National Laboratory. The program used metallic lead as a melt material, both dry and wet spreading experiments were conducted to study the spreading behavior under gravity forces in a BWR drywell geometry.

As for SPREAD program, it was conducted by Suzuki et al. in 1993 in which thermite was used under high-temperature in a first case of a one-dimensional spreading into a concrete-substrate channel and in second case, into an open area.

From 1994 to 2003, Veteau et al. performed at the CEA/DRN/DTP, the CORINE experiments in which low temperature simulant such as water, glycerol and cerrotru were used in 7 m long horizontal spreading section with an inclination angle of 19°.

For KATS/ECOKATS program (Fieg et al. 1996, Foit et al. 2002,2004 and 2006), it was performed at FZK to study the iron-oxide melt spreading into a large area while cooling is provided by water injected from above. Dry experiments were conducted first then followed by wet one. Moreover, the impact of a coating on melt spreading was investigated as well through uncoated and coated set of experiments.

VULCANO objective was to study the dry spreading of the corium under a low flowrate condition (Cognet et al. 1998, Journeau et al. 2003, Journeau et al. 2006). Moreover, this experiment employed UO<sub>2</sub> under condition meant to simulate a discharge from the reactor pit after ablation of the sacrificial gate as devised for the EPR.

In the same way, COMAS project was performed at Siempelkamp (Germany) to investigate the spreading behavior of prototypic corium for the development of the EPR core catcher. Emphasis was put on prototypic corium compositions, realistic temperature levels and large spreading masses as well as testing a wild range of material characteristic (Steinwarz et al. 1997,2001).

As for FARO, prototypical material with a composition typical of a corium discharge in a RPV spread over a steel plate channel with an opening angle of 17° (Morris et al. 1997, Cognaet et al., 2001).

S3E (Scaled Simulant Spreading Experiments) performed at the Laboratory of Nuclear Power Safety at the Royal Institute of Technology in Stockholm, had for objective to map the transition of material physical properties through the different spreading

regimes such as gravity-inertia vs gravity-viscous, dry vs wet (into a coolant) and different heat transfer to substrates (Sehgal et al. 1997).

In the case of VESTA program (Kim et al. 2003 to 2016), the experiment was designed with the core-catcher technology concept in mind and as such, investigated the impingement of a ZrO<sub>2</sub> melt jet on a sacrificial material plate to get information on the ablation characteristics. Two types of melt were therefore used: metallic corium melt with 46% Fe, 31% U, 16% Zr and 7% Cr, and the stainless steel melt.

As for the Hokkaido University projects (Kobayashi et al. 2014, Matsumoto et al. 2017, Miwa et al. 2017, Ogura et al. 2018a, b), similarly to VESTA project, the investigation was focused on a molten metal jet impinging on a spreading metal plate. The selected simulants were copper and zinc, chosen for the physical properties close to the real corium.

In conclusion, those projects have realized an invaluable work to compile on corium spreading. Still, issues exist that should be addressed. First, most of the experiments are done using simulants except the FARO project. Even if they are selected because of their characteristics close to corium's, experimental knowledge drawn from them will need correction and fitting to be applied to real corium. Second, most of the projects were driven by limited purposes such as code validation, geometries or physics. This trend is lessening in the case of more recent projects as knowledge grows on spreading phenomenon.

#### b. Dominant factors

According to the previous works (Dinh et al. 2000), spreading is mainly governed by gravity, inertia and viscosity. Therefore, previous studies were organized in the following regime categorizations: gravity-inertia driven and gravity-viscous driven. Viscosity is a dominant factor in the latter mentioned regime while negligible in the former. Here, the factors highlighted by the different spreading program are summarized.

For the BNL program, the experimental results showed that water-layer height, in the wet spreading case, and initial melt super heat were dominant factors in determining the



spreading regime. Moreover, in the case of spreading under shallow water, useful insights were gained as it was found to be a transient case between dry and deep water pool spreading conditions. This transitional behavior was emphasized by the complete vaporization of the shallow water layer over the spread melt, leading to the change between the spreading regimes driven by the modification of the heat transfer.

As for SPREAD program, the spreading process seemed to be terminated when 55% of the fusion heat is effectively removed from the melt. Moreover, it seemed at first that the melt spreading angle was fixed around the value of  $130^\circ$  but later was rather found to be a function of the flow rate and the melt superheat.

In the CORINE experiments, it is appeared that initial coolant fluid temperature had a significant effect on retarding the bottom crust formation (Alsmeyer et al. 1995). In the case of underwater spreading, it was found that mean melt height was roughly the same as the water layer one in those experiments.

KATS (Fieg et al. 1996) experiments investigated the following parameters: melt phase (oxidic and metallic) through the use of alumina and iron as simulants, melt flow rate, substrate condition (dry or wet) and melt superheat. In the dry case, oxidic and metallic melts shown different spreading characteristics that were later classified as an effect of the gate opening. Nevertheless, follow-up experiments illustrated the melt discharge rate and spreading front propagation velocity impact on the spreading length and therefore on the debris thickness. In the wet configuration however, spreading lengths were found to be shorter than the similar dry spreading experiments. Moving forward with their experiments, KATS researchers reproduced the spreading conditions that are representative of the EPR assumed accidental conditions. In one-dimensional apparatus, different types of spreading surface were evaluated such as concrete, epoxy-coated or ceramic area. Even if the spreading lengths were of the same order of magnitude, the notable differences were attributed to the different heat transfers between melt and area, the formation and percolation of gas in the case of concrete erosion.

As for COMAS (Steinwarz 1997) project, dry spreading was shown to be independent of the substrate materials used, here in this case concrete, ceramic or cast iron. Moreover, intense gas and vapor release were observed in the concrete case but it had little effect on spreading velocity and length.

FARO (Sehgal et al. 1997) tests underlined that radiation heat losses have a strong influence on the melt stopping behavior. Moreover, it seems that there was in this project a correlation between large melt masses and a spreading length increase but nothing proportional.

In the case of S3E program (Sehgal et al. 1997), a large number of experiments was conducted to investigate different pairs of melt/coolant, substrates, one to two dimensional channels, channels into two-dimensional spreading area to gain knowledge on the effects of melt superheat, melt flow rate, eutectic versus non-eutectic and melt volume. As described before, those experiments have shown the same trend where wet spreading is less effective but assure a better heat removal induced by an enhanced heat transfer. Also, porous layer formation, spallation and gas generation/percolation by concrete/melt interaction were significant disturbing factors as shown in those experiments. Concerning the dimension factor, 2D spreading area was found to be a rather effective configuration to enhance spreading.

As for the VESTA project (H.Y. Kim et al. 2010 to 2016), jet impingement was at the core of the project as much as the interaction between the corium melt and the sacrificial material of the core catcher. Following that assessment, the influencing factors were found to be the corium jet composition, the superheat of the melt, the impinging and spreading velocity, and finally the thermophysical properties of the involved materials.

In the case of Hokkaido University projects (Kobayashi et al. 2014, Matsumoto et al. 2017, Miwa et al. 2017, Ogura et al. 2018a, b), the spreading was observed after the impingement of a molten metal jet formed with either Copper or Zinc. The driven factors were assumed to be the melt mass, nozzle diameter, falling height, melt superheat, spreading plate and coolant temperature.

In conclusion, those projects were able to study a large array of dominant factors. Still, there are issues that need to be addressed. Most of the early results are limited by the selected geometries and/or physics. It undermines any knowledge obtained from them. However, that trend is lessening in more recent projects.

c. Models and scaling analysis

Projects reviewed in the previous chapter were not only conducted to collect quantitative or qualitative information on corium spreading but to serve in most cases, as validation data for simulation software or to devise scaling coefficients for the technical design such as for the core catcher technology. Therefore, in the following section, such processes and coefficients will be reviewed.

First, it is necessary to go through the different approaches used by simulation developers to effectively reproduce the physics encountered in the different projects experiments. Those approaches are divided as follows: analytical, semi-empirical, simplified-to-mechanistic transient, and direct approaches. Approaches and codes developed by the different programs are summarized in Table 2.2.

Code	Country	Model characteristics
CORFLOW	Germany	2D-mechanistic
CROCO	France	Simplified (ISPN)
LAVA	Japan	2D-Bingham fluid
MELTSREAD	USA	1D-complex physics and chemistry
MECO	Germany	Mechanistic
RASPLAV/SPREAD	Russia	2D-hydrodynamic
SPREAD	Japan	Simplified
THEMA	France	Phenomenological (CEA/DRN)

Table 2.2: Code for melt spreading simulation (Dinh et al. 2000)

Analytical approach is based on various simplification of the Navier-Stokes equation such as shallow-water approximation or the lubrication theory used in one-dimensional and axisymmetric spreading. Moreover, solidification is neglected in this approach to simplify the search for an analytical solution. Meaning that approach is limited to simple scenario and strict initial condition. In the same way, semi-empirical models are simplified correlations based on experiments but still retained the flaws inerrant to empirical laws. Moreover, those empirical correlations and assumptions were derived from a relatively small amount of small-scale experiments. Therefore, there were limited use of such models in reactor assessments in the past literature.

Models following the past mainstream tendency of using experiments to validate codes, codes such as CORFLOW (Wittmaack, 1997), MELTSPREAD (Farmer et al. 1990), THEMA (Spindler and Veteau 2006a, Spindler and Veteau 2006b), LAVA (Allelein et al., 1999) and the others (in Table 2.2) are what were called simplified to mechanistic transient simulation codes. As it is difficult to simulate the different phenomena involved in spreading easily, assumption and simplification are inevitable. In the case of simplified codes, simplifications are significant and the focus is put on simulating the general behavior of the spreading under those simplifications but in the case of mechanistic models, the assumptions are made with respect to some local physical parameter and property, such as in CORFLOW or MECO for example. As this approach focuses on particular physics and/or geometries, the resulting codes tend to simulate properly when used within the scope they were modeled. Therefore, they are quite useful when trying to simulate accidental scenario they may cope with but they are limited to such use.

Finally, the direct approach is used only on very simple cases of hydrodynamics spreading. The direct numerical simulation (DNS) has most recently shown improvement in its capacities to simulate the different physics implied in the corium spreading. Commercial software such as STAR-CCM+, Fluent and others have shown progress in that sense with the amelioration on Volume of Fluid, Level-Set and Front Tracking models and other algorithms (Wan-SikYeon et al. 2012).

Moving on to the scaling coefficients, it is important to know that those coefficients were developed under particular conditions. According to that approach, numerous authors tried to build scaling formalisms as summarized in Table 2.3. Generally speaking, those past studies reported in Table 2.3, few resulted in full flesh scaling laws but were useful background for Dinh et al. (1999).

Author(s)	Year	Focus	Time and Length Scales
Huppert	1982	Viscous regime	Yes
Greene et al.	1988	Water depth	None
Moody	1989	Heat transfer, $q_{che}$	$\tau_{sol}$ , U (inviscid)
Kazimi	1989	Heat transfer to concrete	None
Find and Griffiths	1990	Morphology	$\tau_{sol}$
No and Ishii	1991	Integral	Dimensionless groups
Theofanous and Yan	1993	Transient, Multi-dimensional	Froude number
Veteau et al.	1995	Geometrical scale	Regime transition
Ehrhard	1996	Flow regimes	Not explicit

Table 2.3: Previous scaling-related considerations (Dinh et al. 2000)

From this publication in 1999, a scaling rationale for melt spreading with solidification was developed at the Royal Institute of Technology. To build out this rationale, two scales were elected: Length and time scales. Dimensionless length and time scale, L and T, were derived. As a result, under the assumption of inviscid and one-dimensional spreading, the relation can be written as follow:

$$L = C * T^{1/2} \quad (2.1)$$

With the comparison to experimental data, the coefficient C was found to be of the order of unity. As for the viscous case, the previous equation is found to be modified as following:

$$L = C_v * N^{1/2} * T^{1/2} \quad (2.2)$$

Where coefficient  $C_v$  is of the order of unity and N is a viscosity number defined as

$$N = \frac{v^{1/2} * V_{tot}^{1/2} * g^{5/24}}{D^{1/3} * G^{13/24}} \quad (2.3)$$

Using the 2D-channel melt spreading experiments, the relation was re-evaluated under those new conditions and modified as following:

$$L = C_\alpha * A^{1/2} * N^{1/2} * T^{1/2} \quad (2.4)$$

Where A is of the order of unity according to the results mentioned previously, meaning that the spreading in that case behaved like a 1D case. Finally, for the open area spreading case, the same relation was improved and rewritten in the following form:

$$L = C_\alpha * B^{1/2} * N^{1/2} * T^{1/2} \quad (2.5)$$

Where B is defined in the following Table 2.4.

	B
Hydrodynamic regime	$\frac{1}{1 + \frac{2R}{D_0}}$
Open channel flow theory	$D_0 \left( \frac{360\delta_{cap}}{\alpha_{ocf}\pi V_{tot}} \right)^{1/2}$

Thermal-control regime	$\frac{1}{1 + \frac{2\tau_{\text{solid}}U_0}{D_0}}$
------------------------	---

Table 2.4: Parameter B (Dinh et al. 2000)

On a more recent note, using the work of Aziz et al (2000) on deposition of metal droplet on steel plate, Hokkaido projects (Miwa et al. 2017, Matsumoto et al. 2017, Ogura et al. 2018a and b) managed to build scaling coefficient for a free-fall induced 3D spreading using redefined length and time scales  $L^*$  and  $T^*$ , formulated as following:

$$L^* = C. T^{*2/3} \quad (2.6)$$

In conclusion, simulation codes and scaling coefficients were built through the use of the data collected by the different projects. However, issues are still emerging from those developments and need to be addressed. First, those codes and coefficients were built under assumptions, geometries and initial conditions chosen by the different project's researchers. Therefore, they are limited by them and it is detrimental to their prediction capabilities. Second, even if the database used is impressive, the codes and coefficients validation is limited to the above-mentioned information selected by the researchers. This renders the use of such codes and/or coefficients inadequate to real accident cases or relevant only in the case of limited scenario.

### 3. Jet Breakup and Fragmentation phenomena in the case of corium loss event

#### a. Jet breakup and Fragmentation previous experiments

In this section, the focus is put on experiments that were devised mainly for investigations on molten jet in the case of Light Water Reactor (LWR). As most of the experimental programs were focused on the fuel-coolant interaction as well, jet breakup and fragmentation of molten corium or simulants in coolant liquid, mostly water or equivalent, were also investigated.

Let first start with programs working with oxide in their jet experiments. According to the information summarized in Table 2.5, FITS (Mitchell et al. 1981, Corradini et al. 1981), CCM (Spencer et al. 1994), MIXA (Denham et al. 1994), ALPHA (Yamano et al. 1995) and ECO (Cherdron et al. 2005) all involved an oxide melt injection using a thermite reaction. In the TVMT installation, IPPE experiments used melt of thermite mixture instead (Zagorul'ko et al. 2008). ZREX experiments (Cho et al. 1997,1998) was mainly focusing on hydrogen generation that follow an injection of zirconia melt. Experiments conducted at the KROTOS facility (Hohmann et al. 1995, Huhtiniemi et al. 1997a, 1997b, 2001), FARO/TREMOS/FAT ones (Magallon et al. 1995, 1997, 1999, 2001) and PREMIX experiments (Huber et al. 1996, Schutz et al 1997, Kaiser et al. 1997, 1999, 2001) all involved injection of real corium (oxide-zirconia) or alumina melt. Those experiment results became an important part of the database and significant insight on actual reactor FCI phenomena.

Organization/Test facility/Program	Melt and Coolant
SNL (FITS)	$\text{Al}_2\text{O}_3 - \text{Fe}/\text{Water}$
UKAEA (MIXA)	$\text{UO}_2 - \text{Mo}/\text{Water}$
ANL (CCM)	$\text{UO}_2 - \text{ZrO}_2 - \text{SS}/\text{Water}$
JAERI (ALPHA)	$\text{Al}_2\text{O}_3 - \text{FeO},$ $\text{Al}_2\text{O}_3 - \text{Fe}_2\text{O}_3/\text{Water}$
ANL (ZREX)	$\text{ZrO}_2, \text{Zr}/\text{Water}$
JRC/CEA (KROTOS)	$\text{Al}_2\text{O}_3, \text{UO}_2 - \text{ZrO}_2/\text{Water}$
JRC (FARO/TERMOS,FAT)	$\text{UO}_2 - \text{ZrO}_2/\text{Water}$
FZK (PREMIX)	$\text{Al}_2\text{O}_3 - \text{Fe}/\text{Water}$
FZK (ECO)	$\text{Al}_2\text{O}_3 - \text{Fe}/\text{Water}$
JAERI (GPM)	$\text{Al}_2\text{O}_3 - \text{ZrO}_2, \text{SS} - \text{C}/\text{Water}$
KTH (MIRA)	$\text{CaO} - \text{B}_2\text{O}_3,$ $\text{MnO}_2 - \text{TiO}_2,$ $\text{WO}_3 - \text{CaO}/\text{Water}$



IPPE (Pluton)	ZrO <sub>2</sub> – Fe/Water
KTH (DEFOR)	CaO – B <sub>2</sub> O <sub>3</sub> , MnO <sub>2</sub> – TiO <sub>2</sub> , WO <sub>3</sub> – CaO, WO <sub>3</sub> – TiO <sub>2</sub> , Bi <sub>2</sub> O <sub>3</sub> – TiO <sub>2</sub> , Bi <sub>2</sub> O <sub>3</sub> – CaO, Bi <sub>2</sub> O <sub>3</sub> – WO <sub>3</sub> , WO <sub>3</sub> – ZrO <sub>2</sub> /Water
KAERI (TROI)	UO <sub>2</sub> – ZrO <sub>2</sub> – Zr, UO <sub>2</sub> – ZrO <sub>2</sub> , ZrO <sub>2</sub> – Zr, ZrO <sub>2</sub> , Al <sub>2</sub> O <sub>3</sub> /Water
KTH (MISTEE-jet/JEBRA)	WO <sub>3</sub> – Bi <sub>2</sub> O <sub>3</sub> , WO <sub>3</sub> – ZrO <sub>2</sub> /Water

Table 2.5: Previous experiments on FCI using oxide/water pairing (Iwasawa and Abe 2018)

JAERI experiments (Moriyama et al. 2005) were conducted while using alumina-zirconia and stainless-carbon injections to investigate a methodology for jet breakup length and fragment size estimation.

MIRA experiments explored a wild array of oxide melts for its injection. In the same facility, DEFOR experiments (Kudinov et al. 2008, 2010, 2013, 2015; Karbojian et al. 2009) had for goal to investigate, through use of various oxide melts, the agglomeration of particulate fragments from a melt jet.

The OECD/NEA SERENA programs focused their analysis on experiments done at KROTOS and TROI facilities on vapor explosion common in such event (Hong et al., 2013). In the same trend, KAERI program studied vapor explosions generated by an injection of corium melt (Park et al., 2001,2008,2013; Song et al., 2002, 2003, 2016, 2017;

Kim et al., 2003,2004,2005,2008,2011; Song et al.,2005; Hong et al., 2013,2015,2016; Na et al., 2014,2016).

The same program also investigated in-vessel corium retention and the external reactor cooling needed in such a case, but the experiments were conducted without the free fall motion of the corium melt inherent to such an event.

Finally, experiments conducted at the MISTEE-jet and JEBRA facility were done to study the fragmentation difference between oxide and metallic melt.

Now, concerning programs working with molten metal in their jet experiments, they are summarized in Table 2.6.

Organization/Test facility/Program	Melt and Coolant
ANL	Wood' metal/Water
IKE	Wood' metal/Water
JRC	Wood' metal/Water
ANL	Al, Al-U/Water
BNL	Wood' metal/Water
PNC (MELT-II)	Wood' metal/Water
KTH	Zn, Sn, Cu/Water
JAERI	Wood' metal/Water
KMU	Wood' metal/Water
KMU (COLDJET)	Wood' metal/Water
UT	Wood' metal/Water
JAEA	Wood' metal/Water
IGCAR	Wood' metal/Water
CH	Al, Pb, Bi/Water
IIT	Pb, Al/Water
TIT	Wood' metal, Ga/Water
UT	Wood' metal/Water

MATE (POSTEC)	Wood' metal/Water
KTH (MISTEE-jet/JEBRA)	Sn, Wood' metal/Water
SJTU (METRIC)	Sn/Water

Table 2.6: Previous experiments on FCI using metal/water pairing (Iwasawa and Abe 2018)

At first, experiments were focused on finding the fundamental phenomena involved in the FCI (Spencer et al. 1986, Cho et al. 1991, Schins et al. 1992, Hall et al. 1995, Dinh et al. 1999, Haraldsson 2000), with a few of them including visualization of melt jet. Experiments done by Hall et al. in 1995 at Berkeley Technology Centre investigate the nozzle geometry, single and multi, impact.

In the other hand, ANL (Gabor et al. 1992,1994), JAERI (Sugiyama et al. 1999, 2000, 2002) Korean Maritime University (Bang et al. 2003,2017; Kim et al. 2016), University of Tsukuba (Abe et al. 2004,2005,2006; Matsuo et al. 2008; Iwasawa et al. 2015a,2015b), JAEA (Matsuba et al. 2013), KTH (Manickam et al. 2014,2016,2017) and Shanghai Jiao Tong University (Li et al. 2017) focused on fragment size and shape measurement while the JAEA project going one step further by investigating the fundamental processes.

Vapor generation around the melt jet and vapor explosion were the main focus of MELT-II facility, Pohang University experiments (Kondo et al. 1995, Jung et al. 2016) and Chongqing University (Lu et al. 2016) respectively.

More recently, agglomeration, sealing method of NPP and the effects of internal structures such as control rods on breakup and fragmentation of the jet were conducted by the Indira Gandhi Centre for Atomic Research and Indian Institute of Technology (Mathai et al. 2015, Pillai et al. 2016) for the first one, Tokyo Institute of Technology and University for the two others (Takahashi et al. 2015, Secareanu et al. 2016, Wei et al. 2016).

Organization/Test facility/Program	Melt and Coolant
PNC (JET-I)	Water/Nitrogen, Freon
ANL (MF5B5)	Wood 'metal/Freon
KTH	Water, Salt, Wood 'metal/ Paraffin oil, Salt

Table 2.7: Previous experiments on FCI using other simulant pairing (Iwasawa and Abe 2018)

Finally, concerning the relevant programs working with other type of simulant materials, they are summarized in Table 2.7. For example, JET-I facility (Saito et al. 1998) and MFSBS program (Schneider et al. 1992,1995) experiments investigated the use of Freon and nitrogen as coolants, vapor generation and fragmentation. Saito et al. (1988) and Dinh et al. (1999) works provided respectively a semi-empirical correlation for jet-breakup length estimation, that will be presented in a later section, and data on effect of variables such as physical properties and phase-changing heat transfer.

#### b. Dominant factors

As the previous section has introduced the different experiments/programs performed on FCI, the following section presents the dominant factors for jet-breakup length and fragmentation.

For the dominant factors behind jet-breakup, it was pointed out by Saito et al. (1988) that the generated vapor film at the tip of the melt jet and immediately surrender it, disturbing the contact between melt and coolant, and promote the insertion of the melt jet in the coolant. Similarly, Schneider et al. (1992) also pointed out that the generated vapor tends to disturb the fragmentation while Epstein et al. (1985) suggested that the vapor film suppresses interfacial instability.

Therefore, a melt jet can be considered to penetrate further into the coolant which leads to an all-around reduction of jet instability and fragmentation, meaning that the vapor generation is a key factor in reducing/retarding jet-breakup of the melt jet. Past experiments shown that high coolant subcooling ( $\Delta T_c$ ) render more effective condensation, meaning that a stable vapor film is less susceptible to be generated.

Therefore,  $\Delta T_c$  could be another dominant factor. But full scope of the effects of vapor on jet-breakup and fragmentation still need clarification as Jung et al. (2016) has pointed out.

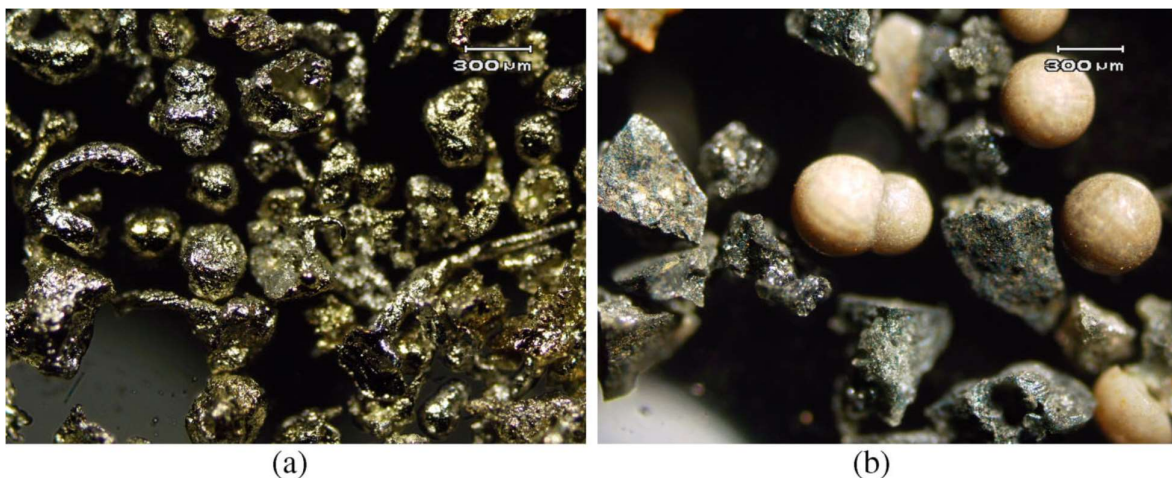


Fig 2.2. (a) Optical micrograph of tin debris from MISTEE test and (b) optical micrograph of PREMIX 18 debris showing angular and spherical pieces. (Tyrprekl et al. 2014)

For the dominant factors behind fragmentation, according to Tyrprekl et al. (2014), through their experiments on oxide and metallic melt injection in water, the shape of the resulting fragments differs from one type of melt to another as shown in Fig 2.2. and 2.3.

Following their assessment through the use of metallographic, analytical and microscopic morphology measurements techniques; the oxide fragments were found to have an angular shape not reproduce by the metallic one, conclusion confirmed by Manickam et al. (2017) recent experiments.

From the different research work, Schins et al. (1986) and Tyrpekl et al. (2014) also concluded that prompt boiling of the coolant can be considered as a factor, which is

dominant in both oxide and metallic melt fragmentation. This will be followed by a prompt fragmentation of the melt into smoother spherical fragments. Moreover, they also presented two more effects linked to oxide melt fragmentation: secondary thermal driven fragmentation that follow the hydrodynamic fragmentation induced by the thermal stress on the melt crust leading to shrinking and cracks, and coolant ingression inside the shrunken and cracked melt that led to the generation of the reported angular fragments.

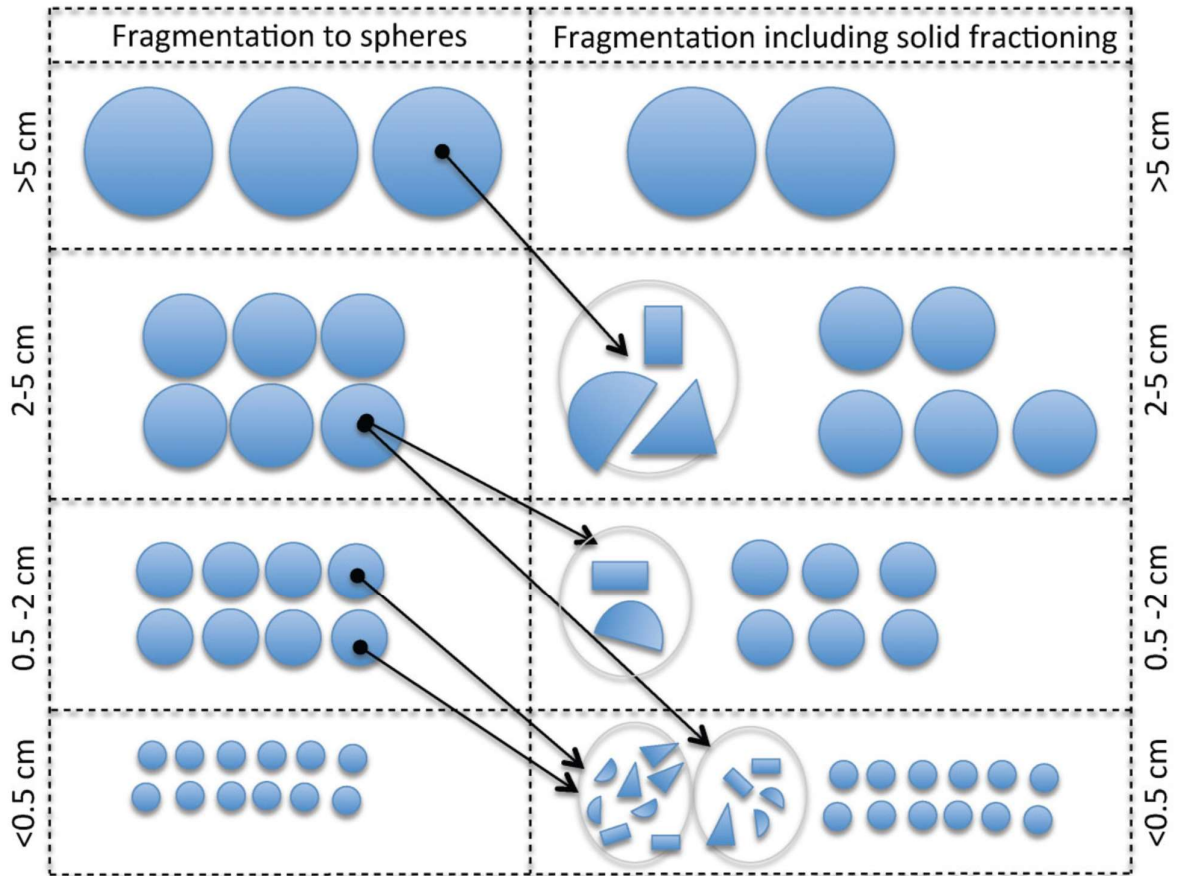


Fig 2.3. Ideal melt fragmentation into droplets (left); melt fragmentation into droplets including possible breakup after melt solidification into angular pieces (right). (Tyrpekl et al. 2014)

On the other hand, as for the metallic melt, Schins et al. (1986) and Tyrpekl et al. (2014) concluded that hydrodynamic fragmentation is dominant as the crust is disturbed by the thermo-elasticity but the thermal stress did not induce breakage as it was the case

for oxide melt. This behavior leads to the formation of the smooth spherical fragments reported in the literature.

To further deepen this analysis, Dombrovsky et al. (2008) mentioned in their work the difference with opaque and semi-transparent melt fragmentation behavior: opaque melt such as corium showed a rapid crust formation governed by the melt surface radiative heat, and semi-transparent melt such as alumina follows a pattern where crust formation is dictated by convective heat transfer and solidification by radiative heat transfer.

Therefore, it is possible to conclude that solidification, crust formation and cracking behavior are also dominant factors for fragmentation. In view of the complexity of those phenomena, solidification will be further more investigated in another section of this paper.

### c. Models and scaling analysis

The different experiments mentioned above were not only done to report quantitative assessments on jet-breakup and fragmentation. The data collected from them was furthermore used to build and devise models to estimate breakup length and fragment size. Therefore, the purpose of this section will be to investigate those models and present the formulations related to them.

First, the jet-breakup modeling. Saito et al. (1988) and Fauske et al. (2001) proposed correlations that are still widely used. First, using the data collected through the experiments, Saito et al. (1988) underlined as reminded in the previous section that the dominant factors for jet-breakup are inertia, buoyancy, thermal and hydrodynamics interactions. Therefore, they developed the following semi-empirical correlation:

$$\frac{L_{brk}}{D_j} = 2.1 * \left(\frac{\rho_j}{\rho_c}\right)^{0.5} * Fr^{0.5} \quad (2.7)$$

$$Fr = \frac{v_j^{0.5}}{gD_j} \quad (2.8)$$

Where  $L_{brk}$  is referenced as the jet-breakup length,  $D_j$  the jet diameter,  $v_j$  the jet velocity,  $\rho$  the concerned fluid density and  $Fr$  the Froude number as defined in Saito et al. (1988) while  $j$  and  $c$  are used to refer to jet and coolant, respectively. Second, Epstein et al. (2001) proposed another semi-empirical correlation based on Ricou et al. (1961) works written as following:

$$\frac{L_{brk}}{D_j} = \frac{1}{2E_0} * \left(\frac{\rho_j}{\rho_c}\right)^{0.5} \quad (2.9)$$

Where  $E_0$  is defined as a tuning parameter called “ entrainment coefficient” ranging from 0.05 to 0.1. Important point to note, current benefit of this Taylor type correlation over the one proposed by Saito et al.(1988) is its independence to the jet velocity  $v_j$ .

Moving on the fragmentation, there are several theories for the fragment sizes estimation such as Kelvin-Helmholtz instability (KHI) or the critical Weber number theory (CWT). As those classical theories take into account only hydrodynamics interactions, numerous previously mentioned works (Dinh et al. 1999, Abe et al. 2006, Bang et al. 2003, Matsuo et al. 2008, Iwasawa et al. 2015a,2015b, Li et al. 2017) underline the effectiveness of those theories at estimating fragment sizes but not reporting actual interface phenomena in their full complex and non-linear behavior.

First, a little more details overview of KHI theory. As presented in 1995’s JSME report, two-dimensions KHI is a linear stability theory that investigates the balance between interfacial tension force and pressure difference resulting from the velocity



discrepancy between the two involved phases. From that investigation, the following characteristic wavelengths were obtained:

$$\lambda_{KHn} = \frac{2\pi\sigma(\rho_1 + \rho_2)}{\rho_1\rho_2v_{rel}^2} \quad (2.10)$$

$$\lambda_{KHm} = \frac{3\pi\sigma(\rho_1 + \rho_2)}{\rho_1\rho_2v_{rel}^2} \quad (2.11)$$

Where  $\lambda_{KHn}$  and  $\lambda_{KHm}$  respectively represent neutral-stable and most-unstable wavelength (Itoh et al. 2004, Matsuo et al. 2008, Iwasawa et al. 2015b) while  $\rho$  refer to the density,  $\sigma$  interfacial tension and  $v_{rel}$  the relative velocity between the two-phases, assumed to be the jet velocity as the ambient coolant is believed to be motionless (Matsuo et al. 2008, Iwasawa et al. 2015b).

As for the critical Weber theory, it is assumed if the Weber number linked to a liquid droplet cross a critical value ranging from 12 to 18 in most studies, the droplet will break up into smaller and much stable droplets under the action of hydrodynamic and interfacial forces as illustrated by Eq (2.12) (Pilch et al. 1987, Uršič et al. 2010 and 2011, Moriyama et al. 2005, Matsuo et al. 2008, Iwasawa et al. 2015b, Manickam et al. 2016 and 2017).

$$D_{frag} = \frac{We_{crit}\sigma}{\rho_2v_{rel}^2} \quad (2.12)$$

Where  $We_{crit}$  is the critical Weber Number mentioned previously.

#### 4. Solidification phenomena in the case of corium loss event

a. Previous solidification experiments

This section will present the previously performed experimental works on solidification during FCI listed in Table 2.8. They are ranging from simple droplet injection experiments with only few grams of simulant to full jet experiments using up until hundreds of kilograms of melt.

According to those works, solidification can be referred either as surface freezing (Fauske et al. 2002) and/or surface solidification (Yang et al. 1987, Cao et al. 2002, Iwasawa et al. 2015a,2015b). As mentioned previously in the fragmentation section, shrinkage and crack formation are induced by the crust formation on the melt surface in most of the experiments using oxide as a melt (Schins et al. 1986, Tyrpekl et al. 2014). As jet-breakup, fragmentation and solidification are deeply linked to each (Burger et al. 1985, 1986), it is a complex process to investigate them all together.

Therefore, most of the studies have elected to view solidification as a separate entity and treat its impact on the two others. Following this simplistic yet effective approach, previous programs and their findings are reviewed in this section.

Organization	Melt/Coolant	Experiment
IKE	Wood's metal/Water	Droplet Injection
NU	Wood's metal/Water	Droplet Injection
JAERI	Sn, Tin/Water	Jet Injection
KTH	Pb-Bi/Water	Droplet Injection

Table 2.8: Previous experiments on solidification effects during FCI (Iwasawa and Abe 2018)

First, Burger et al. (1985 and 1986), Yang and Bankoff (1987) respectively from IKE and NU programs measured through their experiments the shape and size of the fragment of a melt droplet injected into streaming water, reported the impact of solidification on the nullification of fragmentation, and classified the fragmentation into various modes based on those observations.

Experiments of the same caliber but into static water were performed by KTH (Li et al. 1998, Haraldsson et al. 2001) and Hokkaido University project (Sugiyama et al., 1999,2000,2002). From there, KTH team (Li et al. 1998) pointed out a stronger fragmentation for eutectic melt compared to non-eutectic one as well as underlined that non-eutectic melts in the mushy transient saw an increase in viscosity, preventing further fragmentation. It is moreover especially true in cases with small melt superheat. In the same time, NU (Yang et al. 1987) and another portion of KTH (Haraldsson et al. 2001) teams developed a criterion for the breakup behavior of a melt droplet under the assumption developed in Epstein work (1977).

Following that, Nishimura et al. (2002), Zhang et al. (2009) and Sugiyama et al. (2010,2011,2012) reported in their respective studies the impact of solidification on fragmentation in their experiments and from there, proposed an empirical correlation for fragment size estimation. Stepping further, Sugiyama et al. (1999) performed a melt jet experiment with a simulant where the sediment generated were found to be cylindrical meaning that the crust of those fragment was formed by the melt surface solidification before jet breakup.

Following that discovery, Nishimura et al. (2005,2010) and Iwasawa et al. (2015a,2015b) reported the presence of sheet- and filament-shaped sediments in addition to the previously mentioned cylindrical on in their experiments, while they added that despite solidification taking the priority in the melt behavior, the formed jet still broke up under the condition of high jet velocity and high coolant temperature. From those observation, Iwasawa et al. (2015a,2015b) conjectured that Epstein et al. (2001) correlation could be used to estimate the jet breakup length  $L_{brk}$ .

In the same time, Nishimura et al. (2010) proposed another correlation for fragment size estimation under dominant hydrodynamic interaction conditions characterized by high Weber number values. One of the conclusions from those works is that solidification is dominant when the initial interfacial temperature is lower than the melting point of the material used for the melt (Fauske et al. 1973).

## b. Solidification impact on fragmentation modeling

As mentioned in the previous section, the best way to quantify and take into account the effects of solidification on FCI would be to estimate properly the fragment size. Therefore, this section will aboard an up-to-date model proposed by Iwasawa et al. (2015b) for fragment size estimation that also includes solidification effects on the melt jet.

### i. Assumptions and governing equations

Based on previous works done by Epstein et al. (1977), Haraldsson et al. (2001) and the simplification consideration that the jet-coolant interface is infinity in the vertical direction as shown in Fig 2.4., Iwasawa et al. (2015b) built a model using linear stability theory to calculate the growth of jet-coolant interface fluctuation as they are supposed to be small enough to allow that consideration. To complete this model selection, the following assumptions were made:

- Negligible viscosity compared to interfacial tension and crust stiffness
- Inertia neglected as the crust is assumed to be thin enough.
- Fluids are assumed to be incompressible and irrotational allowing the use of potential flow.
- Thermal stress due to temperature gradient neglected
- Crust assumed to be edgeless, infinite size and of constant thickness.

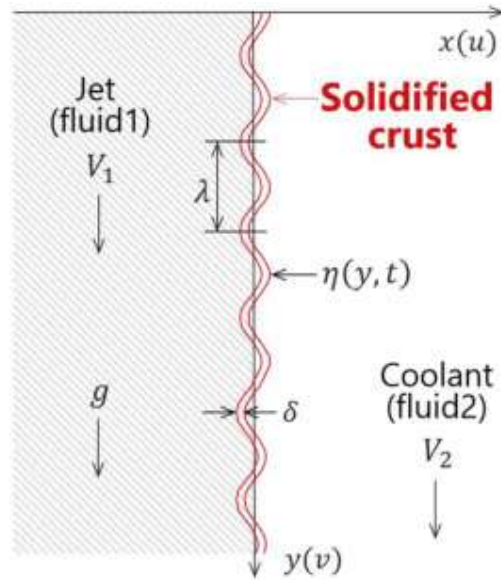


Fig 2.4. Schematic of linear stability model, including solidification effects. Crust formation at the melt jet-coolant interface (Iwasawa et al. 2015).

Following those assumptions, Iwasawa et al. (2015b) employed continuity and Euler equations in a two- dimensional geometry as following:

$$\frac{\partial u}{\partial x} + \frac{\partial v}{\partial y} = 0 \quad (2.13)$$

$$\frac{\partial u}{\partial t} + V \frac{\partial u}{\partial y} = - \frac{1}{\rho} \frac{\partial P}{\partial x} \quad (2.14)$$

$$\frac{\partial v}{\partial t} + V \frac{\partial v}{\partial y} = - \frac{1}{\rho} \frac{\partial P}{\partial y} + g \quad (2.15)$$

Where  $P$  refers to pressure and  $g$  to gravitational acceleration. This set of equations is therefore applied to the melt jet and the coolant. As the interface fluctuation is assumed to be small enough, the non-linear term in Euler equations can be neglected and allow the interface displacement to be formulated as follow:

$$\eta(t, y) = \eta_0 e^{i(\omega t - ky)} \quad (2.16)$$

As interfacial fluctuation is linked to the variation of velocities  $u$  and  $v$ , it is important to provide an equation to quantify that link. That relationship can be written as follows:

$$u = \frac{d\eta}{dt} = \frac{\partial \eta}{\partial t} + V \frac{\partial \eta}{\partial y} \quad (2.17)$$

To complete the model by considering the solidification effects, the following modified Laplace law (Epstein et al. 1977, Haraldsson et al. 2001) is used:

$$D \frac{\partial^4 \eta}{\partial y^4} - \sigma \frac{\partial^2 \eta}{\partial y^2} = P_1 - P_2 \quad (2.18)$$

Where  $\sigma$  refers to interfacial tension, defined as  $\sigma = \sigma_1 + \sigma_2$  (Epstein et al. 1977) where  $\sigma_1$  symbolizes the interfacial force between melt and crust,  $\sigma_2$  the interfacial force between coolant and crust, and finally  $D$  the bending stiffness.

In this equation, the left-hand side summarizes the elastic force due to mechanical strength of the crust with the first term and the interfacial force acting on the crust with the second term.

Using the potential flow assumption, the velocities  $u$  and  $v$  can be expressed using a potential function  $\phi$ :

$$u = -\frac{\partial \phi}{\partial x} ; v = -\frac{\partial \phi}{\partial y} \quad (2.19)$$

Moreover, boundary conditions and continuity equation for  $\phi$  can be defined and written as follows:

$$\frac{\partial \phi_1}{\partial y}(t, -\alpha, y) = 0 ; \frac{\partial \phi_2}{\partial y}(t, \alpha, y) = 0 \quad (2.20)$$

$$\frac{\partial^2 \phi}{\partial x^2} + \frac{\partial^2 \phi}{\partial y^2} = 0 \quad (2.21)$$

Where subscripts 1 and 2 refer to the jet and the coolant, respectively.

ii. Derivation of the interface growth rate (Itoh et al., 2004; Matsuo et al., 2008)

To complete the set of equations previously shown, it is necessary to calculate the characteristic wavelengths used in the linear stability theory and therefore the growth rate of the interface displacement. As mentioned, the temporal and spatial growth rates, respectively  $\gamma_t$  and  $\gamma_s$ , are defined by the following equations:

$$\gamma_t = \text{Re} \left( \frac{1}{\eta} \frac{d\eta}{dt} \right) = \text{Re}(i\omega) = -\omega_i \quad (2.22)$$

$$\gamma_s = \text{Re} \left( \frac{1}{\eta} \frac{d\eta}{dy} \right) = \text{Re}(ik) = -k_i \quad (2.23)$$

To determine these growth rates, it is necessary to go even deeper and provide an expression for the angular frequency  $\omega$  and wave number  $k$ . To do so, a good starting point is to rewrite and integrate the Eq. (2.13) along the x-direction after replacing  $u$  and  $v$  by  $\phi$ :

$$P = \rho \frac{\partial \phi}{\partial t} + \rho V \frac{\partial \phi}{\partial y} \quad (2.24)$$

Assuming that  $\varphi$  can be rewritten as:  $\phi_1(t, x, y) = \phi_{01}e^{kx}e^{i(\varpi t - ky)}$  and  $\phi_2(t, x, y) = \phi_{02}e^{-kx}e^{i(\varpi t - ky)}$  corresponding to wave propagation functions, the previous equation (Eq. (2.23)) could be expressed in the following way:

$$P_1 - P_2 = \phi_{01}\rho_1(\varpi - kV_1)ie^{kx}e^{i(\varpi t - ky)} - \phi_{02}\rho_2(\varpi - kV_2)ie^{-kx}e^{i(\varpi t - ky)} \quad (2.25)$$

Next step is to substitute Eqs. (2.15), (2.18) and (2.24) into Eq (2.16) to obtain the following formulations:

$$\phi_{01}ke^{kx} = -\eta_0(\varpi - kV_1)i \quad (2.26)$$

$$\phi_{02}ke^{kx} = -\eta_0(\varpi - kV_2)i \quad (2.27)$$

In addition, by substituting Eq. (2.15) into Eq. (2.17), the following equation is obtained:

$$Dk^4 + \sigma k^2 \eta_0 e^{i(\varpi t - kx)} = P_1 - P_2 \quad (2.28)$$

Finally, the dispersion relation used in the present is obtained by substituting Eq. (2.24) into Eq. (2.27) and eliminating  $e^{\pm ky}$  using Eqs. (2.25) and (2.26). This operation results in the following formulation:

$$(\rho_1 + \rho_2)\varpi^2 - 2k(\rho_1 V_1 + \rho_2 V_2)\varpi - Dk^5 - \sigma k^3 + (\rho_1 V_1^2 + \rho_2 V_2^2)k^2 = 0 \quad (2.29)$$

As this equation can be considered as a polynomial function of the second order for  $\varpi$ , it can be easily solved as following:

$$\varpi = \frac{(\rho_1 V_1 + \rho_2 V_2)k}{(\rho_1 + \rho_2)} \pm \sqrt{\frac{Dk^5}{\rho_1 + \rho_2} + \frac{\sigma k^3}{\rho_1 + \rho_2} - \frac{\rho_1 \rho_2 (V_1 - V_2)^2 k^2}{(\rho_1 + \rho_2)^2}} \quad (2.30)$$



Using the assumption that the spatial growth rate  $\gamma_s$  can be neglected (Iwasawa et al. 2015) meaning that  $\gamma_s = 0$  leading to  $k_i = 0$ . From there, it can be concluded that  $k$  is real number as its imaginary part is null. To assure the existence of temporal growth, Eq. (2.29) needs to possess an imaginary part that lead to the left part of this expression to be imaginary. Therefore, knowing that  $k = 2\pi/\lambda$ ,  $\gamma_t$  can be expressed as follows:

$$\gamma_t = \left[ \frac{\rho_1 \rho_2 (V_1 - V_2)^2}{(\rho_1 + \rho_2)^2} \left( \frac{2\pi}{\lambda} \right)^2 - \frac{\sigma}{\rho_1 + \rho_2} \left( \frac{2\pi}{\lambda} \right)^3 - \frac{D}{\rho_1 + \rho_2} \left( \frac{2\pi}{\lambda} \right)^5 \right]^{\frac{1}{2}} \quad (2.31)$$

In the right-hand side of Eq. (2.30), the first term is assumed to refer to the destabilizing effects of the phase velocity difference induced dynamic pressure drop, the second refers to the interfacial tension stabilizing effects and the third to the stabilizing effects of the elastic force induced by the mechanical strength of the crust.

For that formulation, it can be concluded that interface instability appears when the term under the square root is positive which happen when the first term in this expression is larger than the two others. As an addendum, it is also important to note that if the third term is neglected, the Kelvin-Helmholtz instability can be introduced easily (Haraldsson et al. 2001, Iwasawa et al. 2015b).

### iii. Solidification effects on interfacial instability

Following the results obtained in the previous section, it is possible to draw a relationship between  $\gamma_t$  and  $\lambda$  from Eq. (2.30), as shown in Fig. 2.5 according to the work of Iwasawa et al. (2015b). The graph is split in two regions: stable and unstable. The transition between stable and the beginning of the unstable region is marked by a specific wavelength value named as the neutral-stable wavelength  $\lambda_n$  (Itoh et al. 2004, Matsuo et al. 2008, Iwasawa et al. 2015b).

After that value, the temporal growth rate increase until reaching a maximum value reached for the most unstable wavelength  $\lambda_m$  (Itoh et al. 2004, Matsuo et al. 2008, Iwasawa et al. 2015). Those values are well shown in Fig 2.5. (a) under the KHI theory calculation. In the other hand, Fig 2.5. (b) shows the calculation done using the work of Iwasawa et al. (2015b) and illustrates the impact of solidification by showing the plot for  $D = 0$  and  $D = 1$  Nm. Solidification seems to reduce drastically the maximum value for the temporal growth rate while switching the unstable region to higher wavelength values as shown in Fig 2.5.

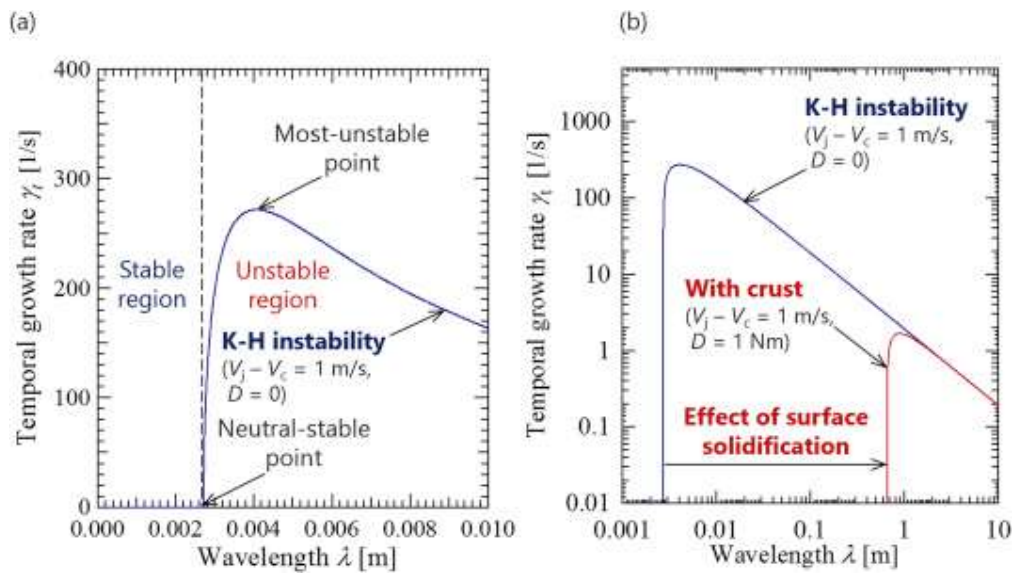


Fig 2.5. Calculated temporal growth rate against wavelength: (a) Kelvin-Helmholtz instability, (b) solidification effects (Iwasawa et al., 2015).

This conclusion is validated by the Fig. 2.6, which shows that as  $D$  increases,  $\lambda_n$  and  $\lambda_m$  increase as well, confirming the shifting effect of solidification on interfacial instability.

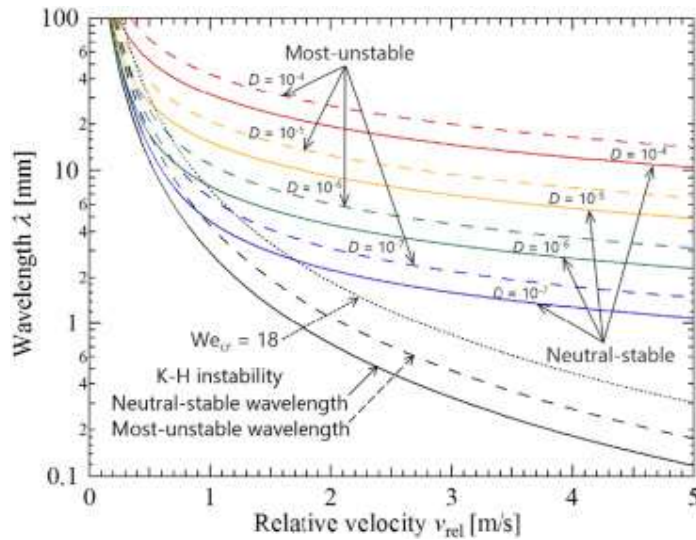


Fig 2.6. Calculated variations in wavelength against relative velocity, and effects of bending stiffness (Nm) (Iwasawa et al., 2015).

This concluded the literature review. In the current stage of the field, the following corium physical behaviors were and are still investigated to improve technologies such as EPR core catcher: Spreading, Jet breakup, fragmentation and Solidification.

One of the conclusions that can be draw from this review work is that past experiments have produced useful preliminary data but were built, in most cases, to help validate restrictive geometries and/or simulation software.

In the other hand, more current works tend to use those data as reference and go beyond, involving the different physics, such as jet breackup, in more complex cases. As such, the impact of those physics are and will be the scope of futures works.

As a part of the mentioned future work, the present study will put its focus on deepening the knowledge on corium jet break-up, spreading and solidification through experiments and simulation in the following chapters.

# Chapter 3: TEPCO Project

## 1. Introduction

The Great East Japan Earthquake occurred on March 11, 2011, struck all of on-site and off-site power sources at the Fukushima Daiichi Nuclear Power Plant (F1), which led to the INES (International Nuclear Event Scale) Level 7 accident. This event culminated with the meltdown of the reactor cores of Units 1 through 3 of the Fukushima Daiichi Nuclear Power Plant (F1).

Numerous studies have investigated the sequencing of this severe accident, the behavior of the created corium and the debris field, such as Andreeva et al. (2007), Espinosa-Paredes et al. (2012) and L. Li et al. (2013). But to deal with the removal of fuel debris accumulated in the Reactor Pressure Vessel (RPV) and Pressurized Containment Vessel (PCV), an in-depth post-accident thermal-hydraulic investigation needs to be conducted (Miwa et al., 2018).

As such, in December 2013, the International Research Institute for Nuclear Decommissioning (IRID) has issued "RFP (Request For Proposal) for Innovative Approach for Fuel Debris Retrieval" to investigate decommissioning methods other than the submersion-method, where the debris is completely covered by liquid coolant.

Following this initiative, Tokyo Electric Power Company (TEPCO) started the examination of the dry-method in 2014, where the fuel debris is cooled by the gas-phase alone. Compared to the well-known submersion-method which was used for the decommissioning of Japan Atomic Energy Agency (JAEA)'s Japan Power Demonstration Reactor (JPDR) and the Three Mile Island Nuclear Generation Station, the dry-method is a completely new approach that needs to be carefully examined, particularly the natural convection behavior with nitrogen injection.

Preceding and following the F1 accident, experimental and numerical researches on fuel debris have been actively carried out in Japan to help the decommissioning such Sugiyama et al. (2005), Su et al. (2006) and Huang T et al. (2012). Using pure molten metal to simulate fuel debris, spreading and deposition behaviors on both dry and wet surfaces were conducted by Ogura et al. (2018a, b). Matsumoto et al. (2017) investigated the spreading behavior of molten metal using scaling parameters.

From the industrial side of the R&D (Research and Development), as the IRID (International Research Institute for Nuclear Decommissioning) project progresses and gains maturity, more detailed insights of the accident timeline are now available. In the earlier works done by Nishihara (2012) and the report published by TEPCO (2011, 2015), structural and thermal behaviors, as well as the composition of fuel debris in the F1 reactor vessels, are well-summarized.

More recent works published by Yamaguchi et al. (2017) and Chen et al. (2018) upon those earlier works to deliver new insight on the risk assessment of the decommissioning. The TEPCO report published in 2015 (TEPCO, 2015) provides more information on the different debris retrieval methods.

As the knowledge on those methods are deepen, it is necessary to provide radioactive contamination information to assure their implementation and effectiveness. To do so, data on the reactor building thermal behavior should be investigated. Therefore, the current work aims to further deepen the available knowledge on F1 decommissioning by provide data on the reactor building thermal behavior through the accident.

To do so, the utilization of the accurate heat transfer model and carrying out a careful evaluation is a necessity. In the present study, three-dimensional thermal-hydraulic analysis for a steady-state and unsteady state were conducted for F1 building

using commercially available computational fluid dynamics (CFD) code STAR-CCM+ Ver.11 under the cooperation of Nuclear Damage Compensation and Decommissioning Facilitation Corporation (NDF).

The present chapter is organized in two main section. The first section will present the targeted area and the set-up used for the simulations while the second section will discuss on the simulations' results and their impact on Fukushima decommissioning project.

As a warning to the lecture, it is important to highlight that, for the sake of simulation efficiency, the present study treats the debris fields as a solid object, not as a porous media.

## NOMENCLATURE

$N_n$  Cell Number of mesh n [-]

$r_{nk}$  Mesh refinement factor between meshes n and k [-]

$\varphi_n$  Variable obtained with mesh n [depend of the variable]

p Apparent order [-]

$\varphi_{ext}^{kn}$  Extrapolated values from the values obtained with meshes n and k [depend of the variable]

$e_a^{kn}$  Approximate relative error between meshes n and k [-]

$e_{ext}^{kn}$  Extrapolated relative error between meshes n and k [-]

$GCI_{fine}^{kn}$  Fine-grid convergence index between meshes n and k [-]

## 2. Targeted area and simulation set-up

In this section, we will present the area selected for the scope of this project, the physical properties and boundary conditions necessary to simulate properly the Unit 1 of Fukushima Daichi under the accidental conditions. The investigated and simulated area shown in Fig. 3.1 consists of the following elements:

- Air, nitrogen and light water for the fluid media
- Stainless steel, carbon steel, concrete from the D/W, S/C, torus room and other structural elements of the reactor building as the solid media
- Fuel debris as a decay heat source from the  $^{134}\text{Cs}/^{137}\text{Cs}$  decay

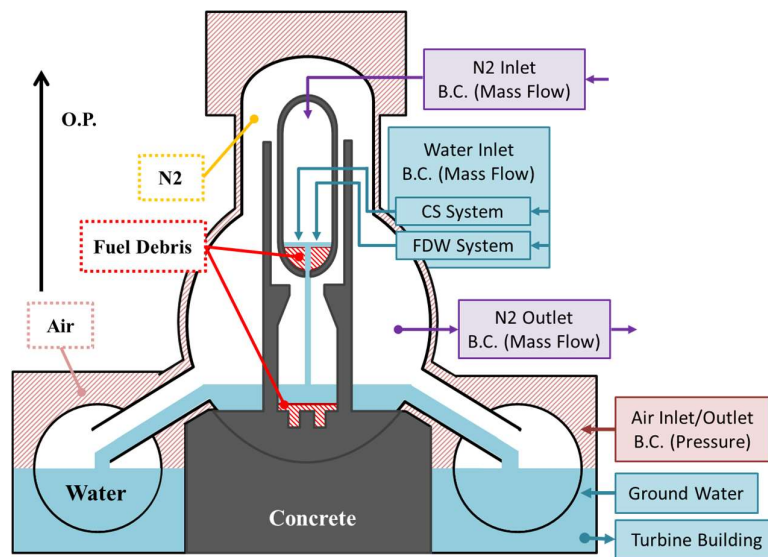


Fig 3.1: CFD Model for the Current Study (Mitsuda et al. 2019).

Currently, to cool the fuel debris, the inlet of cooling water is set on top of RPV fuel debris, injected from the feed water line (FWL) system and the Core Spray (CS) system, and is drained from the bottom of RPV to the pedestal floor. As for the PCV, cooling water flows into S/C through bend pipes and into the torus chamber, allowing us to set the water level at 2.5 m from the pedestal floor in Unit 1.

Groundwater temperature was set to 15 °C, identical to the actual Fukushima site measurement and set to flow through the west wall of the torus chamber and drain from the east wall after mixing with the cooling water in the torus chamber.

In the upper RPV, nitrogen is sealed from the head spray line and sucked out by the gas control equipment. Moreover, the flow rate for both cooling water and nitrogen was set to the average value obtained by the measurements. As for the groundwater, its flow rate was set to the same value as the cooling water inlet, so that the total flow of water ends up drained into the turbine building.

Also, a 5 cm air gap layer between the concrete of reactor building and PCV wall, is used for the heat dissipation from PCV. Finally, the air in the torus chamber flows upward through this air gap, while the air inlet temperature was set at 14 °C.

As for the fuel debris, it is assumed that all the debris were relocated to the lower part of the PCV. The shape of the debris, based on the previous studies, was assumed to follow the geometry shown in Figs. 3.2 and the properties were set as full solid elements of UO<sub>2</sub>.

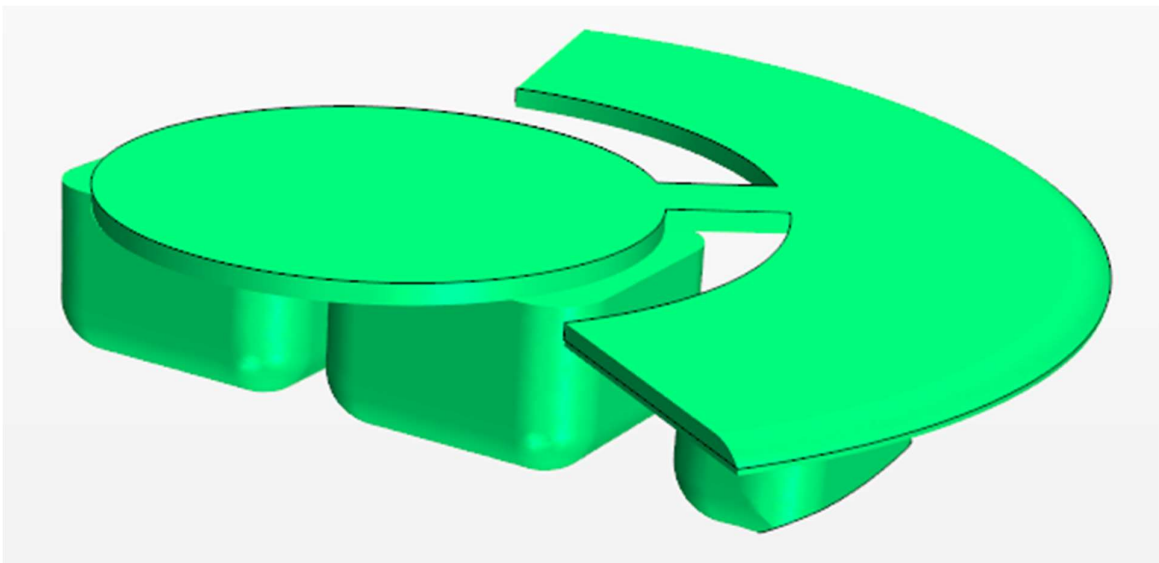


Fig 3.2: 3D Perspective Figure of the Fuel debris (Mitsuda et al. 2019).



Concerning the decay heat generated by the fuel debris, it is assumed that most of it are due to the debris located at the bottom part of the PCV. Numerous past studies (V.H.Ransom et al. 1980, W.Lyon et al. 1975, American National Standards Institute 1979, G. Breit et al. 1936, Samuel Glasstone et al. 1948, K. Way et al. 1952, Harold Etherington et al. 1958) have built standard equations to determine the decay heat,  $E(t)$  in MWth.time, of a nuclear reactor after shutdown such as the following on:

$$E(t) = 8.1 * 10^{-3} * P_0(t^{0.8} - (t + T_0)^{0.8} + T_0^{0.8}) \quad (3.1)$$

where refers to the reactor power level, the reactor shut downtime,  $t$  the time after the shutdown.

However, the above equation is only usable in the case of a proper shutdown using the control rods. Therefore, there was a need for assumption, answered using values provided by the JAEA code ORIGEN 2 and TEPCO data as shown in Fig 3.3. As the simulated scenario is dependable of time, two approaches are possible:

- ➔ Approach I: A step-by-step approach where each simulation realized is a steady state image of a point in severe accident's time. Besides having a lesser accuracy, this approach is quicker and required less computation power to run and converge.
- ➔ Approach II: A full-flesh unsteady approach where the heat of the debris field is set as a function of time built according to the data provided previously. Besides having a higher accuracy for the proposed situation, this approach is longer and required a high computation power to run and converge.

For the present project, as the goal was to provide quick reliable results, it was first elected to use the first approach to determine a tendency and then realized full-flesh unsteady simulations.

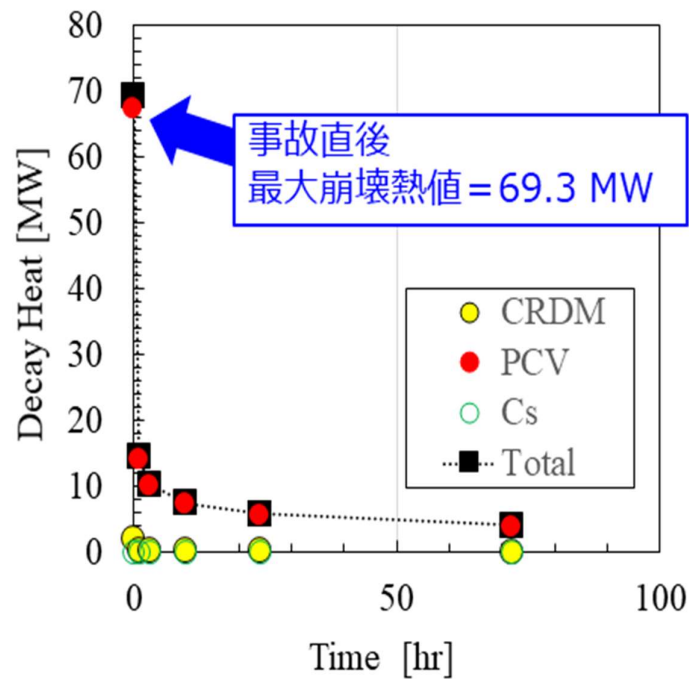


Fig. 3.3 Decay Heat Evolution registered by TEPCO through the F1 Accident (Mitsuda et al. 2019).

Hence, the information described above, as well as the complementary information on the simulation set-up, is summarized in Tables 3.1 to 3.6 were utilized in the current simulation with a numerical uncertainty of 0.7 % for the debris temperature and 3.1 % for the air atmosphere velocity as shown in Table 3.7.

Table 3.1 Simulation Set-up (Mitsuda et al. 2019).

Analysis Code	STAR-CCM+ (Ver.10)
Discretization	Finite-volume scheme
Analysis Approach	SIMPLE method

Cell Number	1.7 ~5.0 million
Mesh Size Distribution	<p>Air: 276211 Cells</p> <p>N2:3053757 Cells</p> <p>PCV: 51236 Cells</p> <p>PCV debris: 44414 Cells</p> <p>RPV: 497669 Cells</p> <p>Water: 602493 Cells</p> <p>Shroud: 17042 Cells</p> <p>Pedestal: 168176 Cells</p> <p>Lower Concrete: 112347 Cells</p>
Numerical Scheme	Second Order Scheme
Turbulence Model	<p>Realizable K-<math>\epsilon</math> model</p> <p>Wall function</p>
Wall Boundary Conditions	<p>Ground temp.: 287 K</p> <p>Outside air temp.: 287 K</p> <p>Ground water temp. : 286 K</p>
Pressure (Outlet)	Atmospheric

Table 3.2 Thermo-physical properties under normal pressure when temperature dependence is not considered (Analysis I) (Mitsuda et al. 2019).

Name of substance	$\rho$	$C$	$\lambda$	$\eta$	$\beta$	$Pr$
	Kg/m <sup>3</sup>	kJ/kgK	W/(mK)	$\mu\text{Pa} \cdot \text{s}$	1/K	—
Uranium oxide (UO <sub>2</sub> )	11000	0.280	10.0	-	-	-
Concrete	2240	0.750	1.60	-	-	-
Austenitic stainless steel (Shroud)	8060	0.480	15.1	-	-	-
Carbon steel	7830	0.434	63.9	-	-	-
<b>H<sub>2</sub>O</b>	998	4.18	0.620	889	3.91E-4	0.9
<b>N<sub>2</sub></b>	1.15	1.04	0.0256	17.9	0.0035	0.9
Air	1.18	1.00	0.0260	18.6	0.0035	0.9

Table 3.3 Thermo-physical properties of solid at normal pressure (Mitsuda et al. 2019).

Name of substance	$T$	$\rho$	$C$	$\lambda$
	K	Kg/m <sup>3</sup>	kJ/kgK	W/(mK)
Uranium oxide (UO <sub>2</sub> )	300	10960	0.237	8.21
	500		0.286	6.53
	800		0.3	4.73
	1300		0.322	3.17
	1800		0.369	2.53
Limestone concrete	293	2400	0.9	1.2
	600		0.93	0.8
	1000		1.63	1
	300	7920	0.449	16

Austenitic stainless steel SUS304SUS304 (18Cr-8Ni)	400	7850	0.511	16.5
	600		0.556	19
	800		0.62	22.5
	1000		0.644	25.7
1% Ni steel (0.4C-0.8Ni)	300	7850	0.47	51.2
	500		0.51	46.1
	800		0.57	36.9
Carbon steel for machine structure S35C (0.34C)	300	7850	0.465	43
	500		0.528	38.6
	800		0.622	27.7

Table 3.4 Thermo-physical properties of liquid and gas under normal pressure (Mitsuda et al. 2019).

Name of substance	$T$ $K$	$\rho$ $Kg/m^3$	$C$ $kJ/kgK$	$\lambda$ $W/(mK)$	$\eta$ $\mu Pa \cdot s$	$\beta$ $1/K$	$Pr$ —
$H_2O$	280	996.62	4.179	0.576	1435.4	9.0E-05	10.46
	300			0.6104	854.4	2.9E-04	5.85
	320			0.6369	577.2	0.00045	3.788
	340			0.6568	422.5	0.0059	2.694
	360			0.671	326.7	0.00072	2.064
$N_2$	100	1.1382	1.041	0.00941	6.87	0.003663	0.716

	20 0			0.01826	12.86		
	30 0			0.02598	17.87		
	40 0			0.03252	22.17		
	50 0			0.03864	26.02		
	60 0			0.0441	29.55		
Air	26 0	1.1763	1.007	Sutherland Law	Sutherland Law	0.00366 3	0.71 7
	30 0						
	32 0						

Table 3.5 Boundary Condition of Cooling Water and Nitrogen (Analysis I, II) (Mitsuda et al. 2019).

Unit	Continuum	Inflow / Outflow location	Flow rate	Temperature
			kg/s	°C
Unit 1	Nitrogen	RPV side N2 enclosed	0.00895	15.2
		PCV gas management system exhaust	0.00665	-
	Cooling water	Furnace water injection (FDW)	2.38	18.3
		Furnace water injection (CS)	2.00	18.1
	Groundwater	Torus room inflow	4.38	15.0

		Torus room outflow	8.76	-
	Air	Staircase inlet	-	15.2
	Cooling water	Furnace water injection (FDW)	0.582	18.1
		Furnace water injection (CS)	0.651	18.0
	Groundwater	Torus room inflow	1.23	15.0
		Torus room outflow	2.47	-
	Air	Staircase inlet	-	15.2

Table 3.6 Inflow / outflow locations of stagnant water and nitrogen (Mitsuda et al. 2019).

Unit	Continuum	Inflow / outflow location	Equivalent diameter	Remarks
1U nit	Nitrogen	RPV flange leak	0.0481 cm	Pressure outlet (atmospheric pressure)
		CRD tube leak	-	-
		Main steam relief safety valve (SRV203-3B)	4.161 cm	-
		Safety valve (SV203-4A)	7.0 cm	-
		Safety valve (SV203-4C)	1.7 cm	-
		PCV flange leak	0.0645 cm	Flow rate 0.00230kg / s
	Cooling water	RPV leakage	15 cm	-
		S / C leak	20 cm (4 spots)	-
	Ground water	S / C leak	20 cm (4 spots)	-
	Air	PCV flange leak	0.0645 cm	-
		Air gap leak	20 cm	Pressure outlet (atmospheric pressure)

Table 3.7 Simulation Discretization Error Calculations (Mitsuda et al. 2019).

	Debris Max Temperature	Air Atmosphere Max Velocity
$N_1$	4823345	4823345
$N_2$	4174354	4174354
$N_3$	3,996,205	3,996,205
$r_{21}$	1.25	1.25
$r_{32}$	1.2	1.2
$\varphi_1$	1005	0.687
$\varphi_2$	1012	0.708
$\varphi_3$	1018	0.638
$p$	0.236	6.3
$\varphi_{\text{ext}}^{21}$	876	0.68
$e_a^{21}$	0.007	0.031
$e_{\text{ext}}^{21}$	0.006	0.01
$GCI_{\text{fine}}^{21}$	0.161	0.0124

### 3. Results and Discussion

Using the approach mentioned in section 2, a set of simulations were built and can be assumed to be pictures through time of the reactor thermal behavior from the point when the corium reached the highest decay heat 69.3 MW up until its lowest decay heat value 2.5 MW. For each of 6 simulations, the resulting temperature profiles for each of them can found in Fig 3.4.



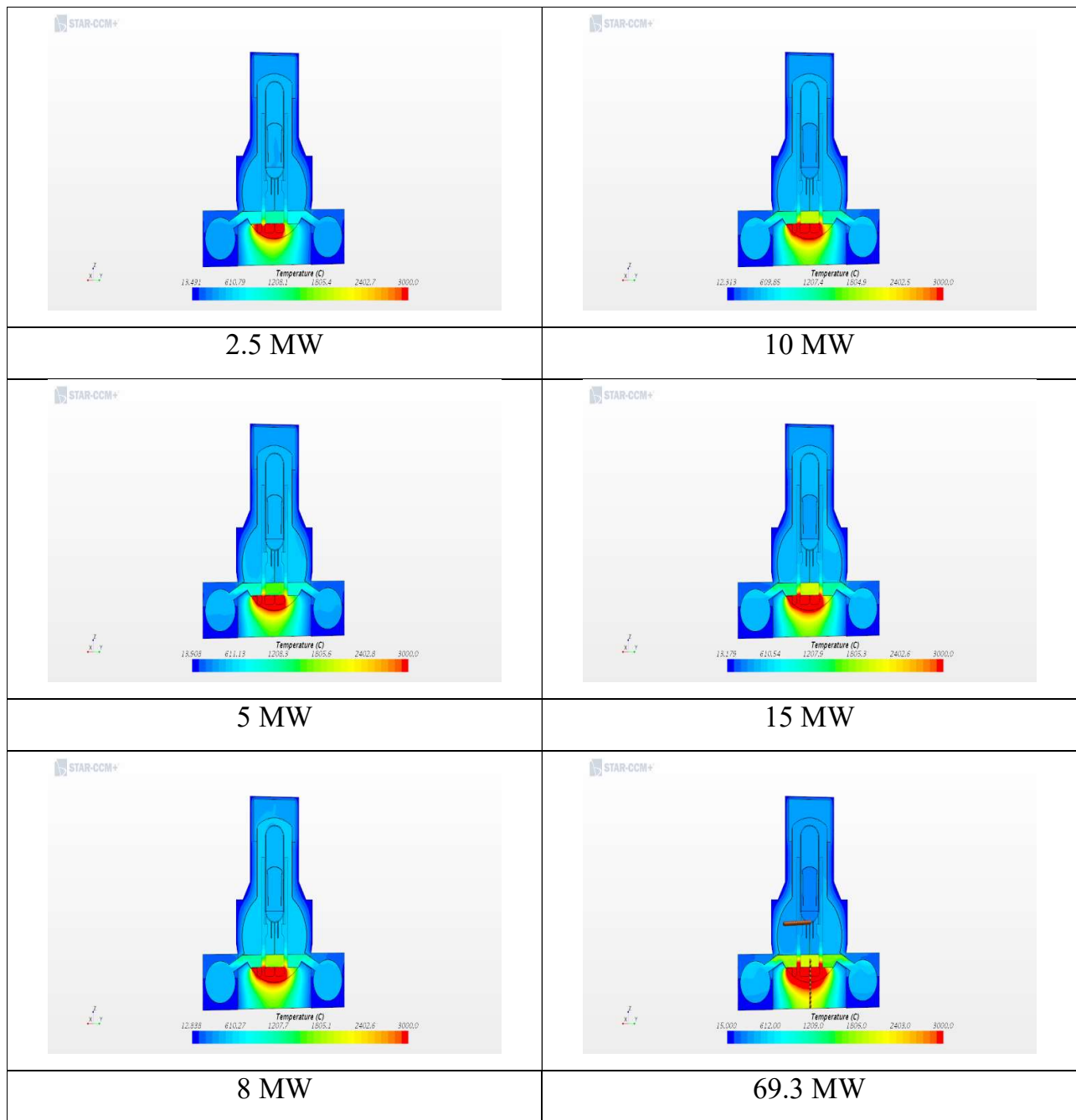


Fig. 3.4 Temperature profiles of the F1 accident simulations

A quick glance at those profiles leads to the following conclusion: most of the heat transfer took place in the bottom concrete section of the reactor building and only superficially went through the laterally surrounding concrete. To assess more thoroughly that assumption, two probes lines were built to retrieve the temperature data evolution along the z-axis and the y-axis. Those lines were designed to visualize the temperature of the bottom concrete for the first one and the surrounding concrete for the second one as

shown in Fig 3.5. Data were therefore collected from the 6 cases stipulated previously and sum up in the graphics shown in Fig 3.6.

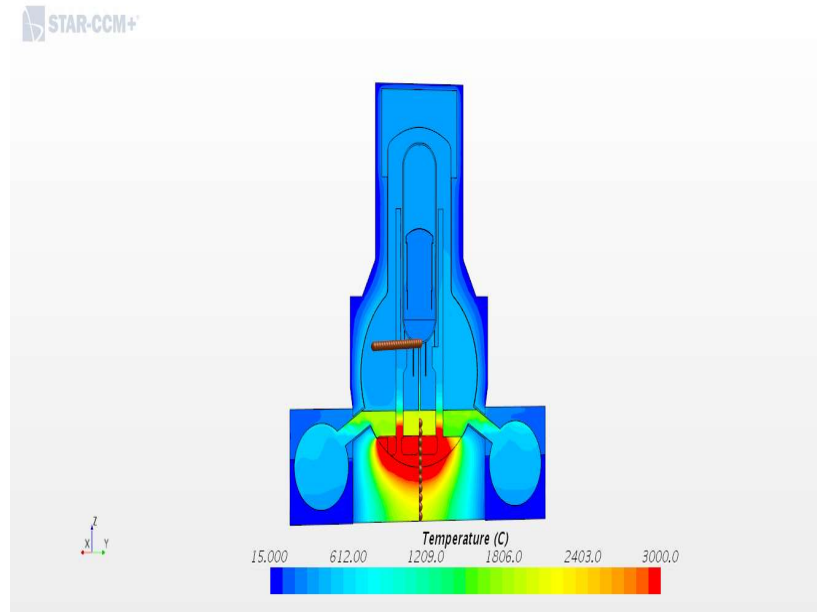


Fig. 3.5 Probe lines Conceptual scheme

With the help of Fig 3.6, we can conclude from the link underline by other studies between concrete temperature and radioactive contamination that most of it will be located deeply inside the bottom concrete and will be more superficial for the lateral one.

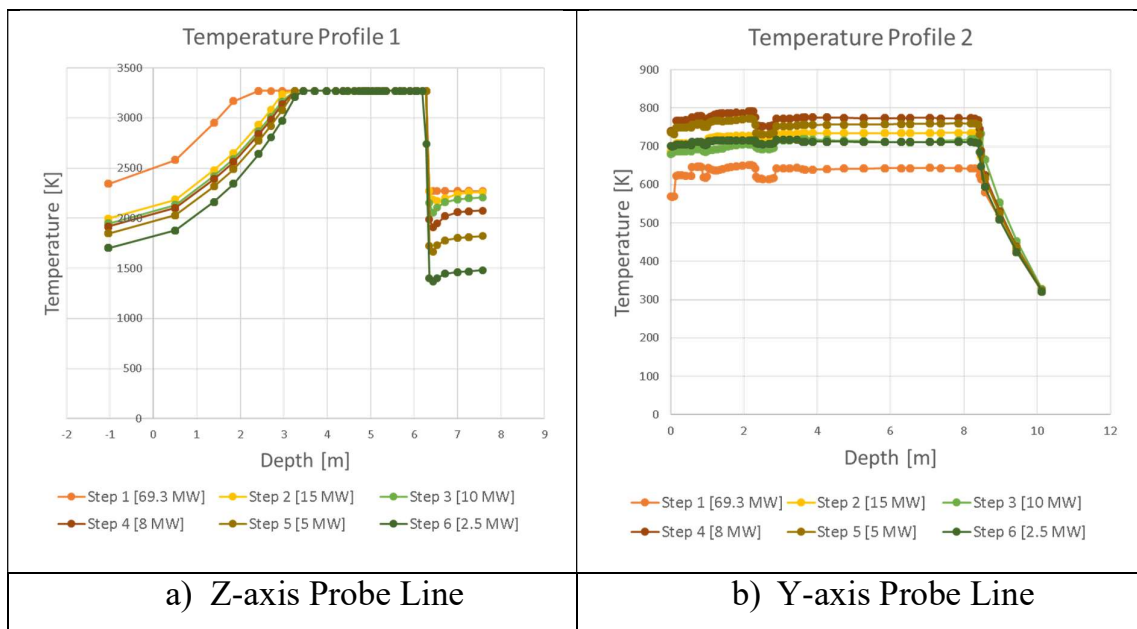
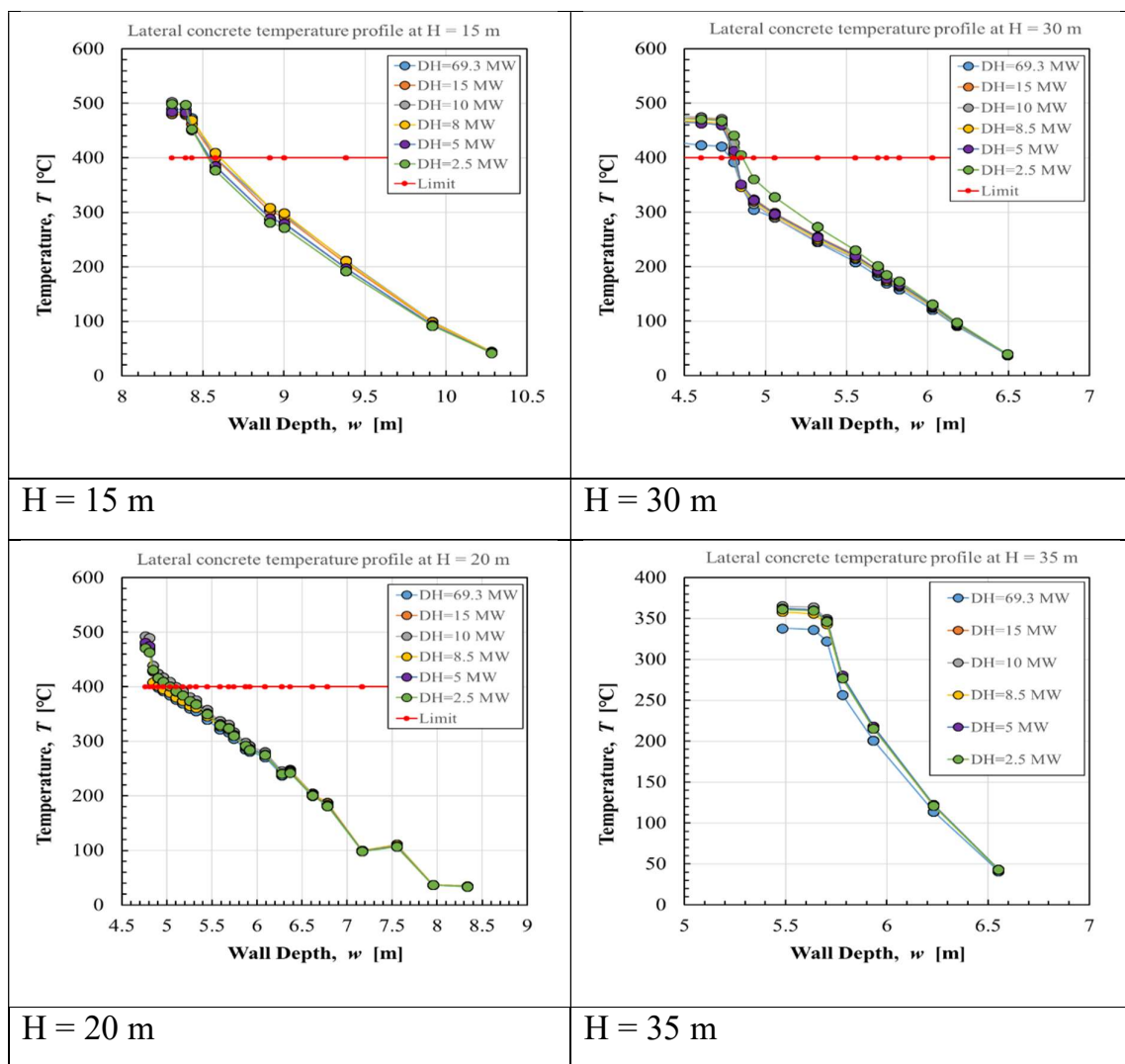


Fig. 3.6 Temperature profiles for bottom concrete and lateral concrete

According to that conclusion, our next efforts were put into the realization of more temperature profiles. The purpose of those extra profiles was to investigate more thoroughly the evolution of the lateral concrete temperature during the accident specially to see if the concrete had reach the critical temperature of 400 °C. That temperature was chosen according to the results of the other team part of this joined project as it was defined as the temperature limit for which, if the concrete is under it, the contamination considers only superficial. From that knowledge, the goal was to determine more precisely the section of the lateral concrete where the contamination will be the deepest. The mentioned results can be found in the Fig 3.7.



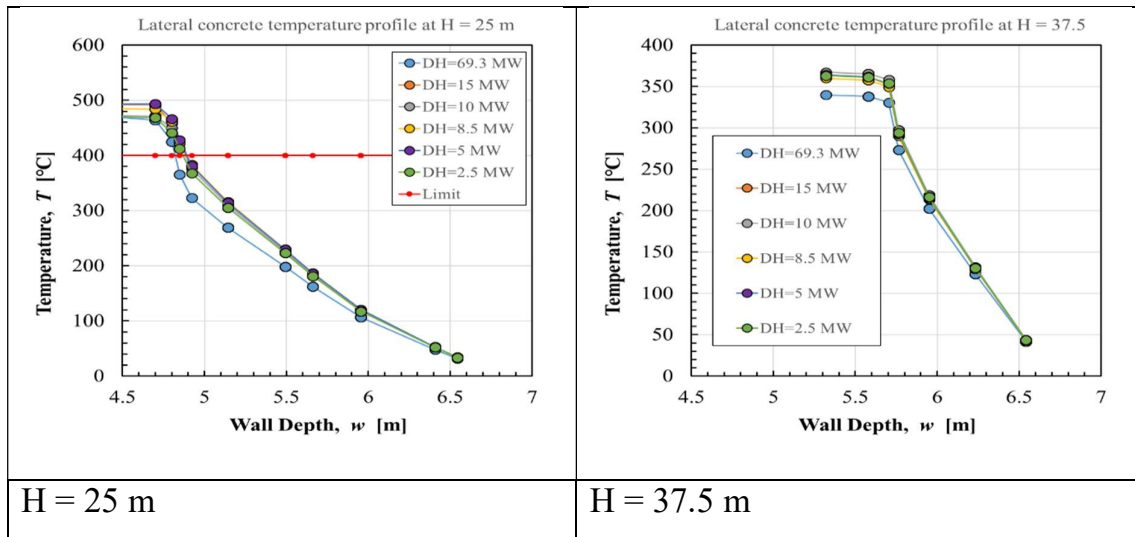


Fig. 3.7 Temperature profiles for lateral concrete at different height along the PCV

According to those results, as we get higher the temperature profile start slowly reach values under the  $400^{\circ}\text{C}$  limit. For the Fig 3.7, we can conclude that the first 25 cm around the PCV lower section were at a temperature superior to the limit for the duration of the accident. Therefore, it can be concluding that the radioactive contamination will be mainly located in that section of the reactor building while the other concrete structures will only be superficially contaminated.

However, it is important to mention that these results were obtained for a fixed setting of the debris field, both for its geometry and position. Therefore, any improvement on these two points will greatly help improving the simulation. Through that acknowledgement, the need to deepen the knowledge on debris field formation is underlined. It is to answer it that the experimental and simulations works of chapters 4 and 5 were realized.

# Chapter 4: Experimental Work

## 1. Introduction

One of the major challenges in nuclear thermal-hydraulics for the severe accident's evaluation and management is the ability to predict core meltdown behaviors (Dinh et al. (2000), Sehgal et al. (2012), Miwa et al. (2018), Sahboun et al. (2020)). Following the fuel meltdown and the displacement of the molten core, the corium goes through interactions with the remaining coolant within the reactor pressure vessel (RPV) and re-located at the bottom of the vessel. Depending on the conditions of RPV's vessel wall, the corium may be discharged to the lower level of the reactor building.

Therefore, to assure the integrity of the reactor building, it will be important to retain the spreading molten core in a confined space such as core-catcher. Large-scale experiments to investigate the spreading of the molten core over a flat area for the design enhancement of the core-catcher were conducted internationally since the Three-mile Island (TMI) accident (Dinh et al. (2000)).

Most of those experiments/simulations were focused on molten core spreading behavior and molten core concrete interaction (MCCI), and actual corium or simulant was utilized on the sacrificial material. In addition to the core catcher design, following the lessons learned from Fukushima-Daiichi accident, advancement in the severe accident code has become a crucial issue in thermal-hydraulic fields, especially to improve predictive capabilities of MCCI and molten metal spreading behaviors (Dinh et al. (2000)).

Moving forward on that account, Ogura et al. (2018a and b) took into account spreading under a downward jet on both dry and wet surfaces. The experimental facility, depicted in Figure 4.1 and Figure 4.2, was utilized for those works. The authors investigated the effective dimensionless numbers of molten metal spreading and deposition. Matsumoto et al. (2017), utilized an exact same test facility to develop a

scaling criterial coefficient for the molten Copper. A summary of previous experiments is tabulated in Table 4.1.

#### Nomenclature

$S$	Surface [ $\text{m}^2$ ]
$v_0$	Initial volume of molten material [ $\text{m}^3$ ]
$V_0$	Jet Velocity [ $\text{m/s}$ ]
$R_c$	Thermal contact resistance [?]
$Q$	Volumetric flow rate of molten metal through the experiment nozzle [ $\text{m}^3/\text{s}$ ]
$c_p$	Specific heat capacity [ $\text{J/kg/K}$ ]
$k$	Thermal conductivity [ $\text{W/m}\cdot\text{K}$ ]
$L$	Latent heat of melting [ $\text{kJ/kg}$ ]
$T_0$	Molten metal initial temperature [ $\text{K}$ ]
$T_p$	Plate initial temperature [ $\text{K}$ ]
$\Delta T$	Temperature difference between phases (here $\Delta T = T_0 - T_p$ ) [ $\text{K}$ ]
$KE_1$	Initial kinetic energy [ $\text{J}$ ]
$SE_1$	Surface energy of the liquid jet before impact [ $\text{J}$ ]
$SE_2$	Surface energy of the spread [ $\text{J}$ ]
$W$	Work done in deforming the jet under the influence of viscosity [ $\text{J}$ ]
$\Delta KE$	Loss of kinetic energy [ $\text{J}$ ]

Oh	Ohnesorge number [-]
Re	Reynolds number ( $Re = \frac{\rho V_0 D_0}{\mu}$ ) [-]
We	Weber number ( $We = \frac{\rho V^2 D_0}{\sigma}$ ) [-]
Pe	Peclet number ( $Pe = Re * Pr$ ) [-]
Pr	Prandtl number ( $Pr = \frac{\mu c_p}{k}$ ) [-]
Ste	Stefan number ( $Ste = \frac{c_p \Delta T}{L}$ ) [-]
Bi	Biot number ( $Bi = \frac{D_0}{k_{jet} R_c}$ ) [-]
$D_0$	Jet/Nozzle diameter [m]
$D_{max}$	Spread maximum diameter [m]
$\theta_a$	Advancing liquid-solid contact angle [°]
s	Solid layer average thickness [m]
$s^*$	Dimensionless Solid layer average thickness ( $s^* = \frac{s}{D_0}$ ) [-]
$d_s$	Diameter when the splat is at its maximum extension [m]
$H_{accidentfalling}$	Accident's falling height [m]
$D_{breach}$	Breach diameter [m]
$K_{accident}$	Accidental scaling coefficient [-]
H	Falling height [m]

$L_j$  Jet breakup length [m]

$m_d$  Molten material initial drop mass [kg]

$t_0$  Characteristic time [s]

$t_j$  Life time of the jet [s]

$t_j^*$  Dimensionless time [-]

#### Greek letters

$\alpha$  Volume fraction [-]

$\rho$  Density [ $\text{kg}/\text{m}^3$ ]

$\mu$  Viscosity [ $\text{Pa s}$ ]

$\sigma$  Surface tension [ $\text{N}/\text{m}$ ]

#### Subscripts

g Gas phase

l Liquid phase

j Jet

mod Value modified by jet-breakup



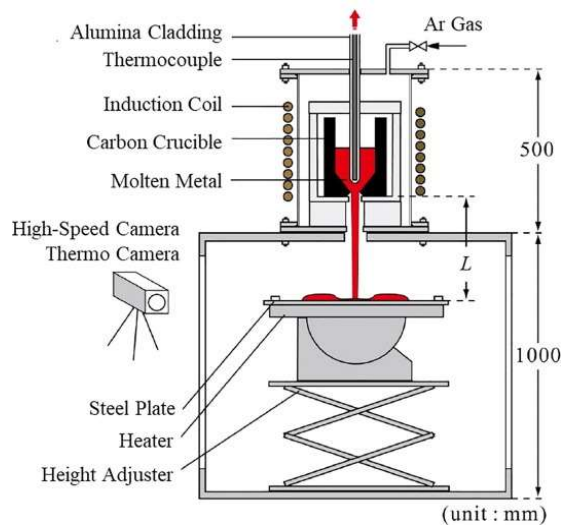


Fig 4.1. Schematic of the test section for molten metal spread experiment (Matsumoto et al. 2017, Ogura et al. 2018a and b, Sahboun et al. 2020)

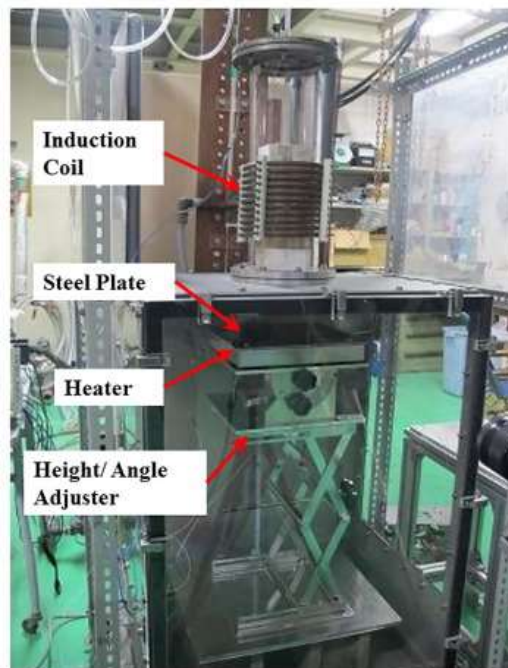


Fig 4.2. Pictorial view of the test section for molten metal spread experiment (Matsumoto et al. 2017, Ogura et al. 2018a and b, Sahboun et al. 2020)

In this chapter, the experimental and analytical investigations of the maximum spreading ratio of molten metal is carried out. The concept of maximum spreading ratio was adopted from the work done by Aziz and Chandra (2000), where the free-falling

molten droplet was utilized to investigate the splashing phenomenon. For the severe accident analysis, one of the important aspects is to obtain the maximum spreading/penetration of corium that follow a melt-through event.

The current study can be considered as a fundamental experiment to understand the key parameters associated to it, and the utilization of maximum spreading ratio concept to describe the spreading of the free-falling molten metal jet.

Table 4.1. Experimental programs on molten metal spreading (Sahboun et al. 2020)

	Institution	Geometry	Melt	Surface Condition	Injection Method
CORINE	CEA (France)	2D-channel	Simulants	Dry	Bottom Injection
BNL	BNL (USA)	2D area	Pb	Dry and Wet	Jet
S3E	KTH (Sweden)	1D, 2D area	Simulants	Dry and Wet	Bottom Injection
SPREAD	Hitachi Energy Research Lab. (Japan)	1D, 2D area	Thermite	Dry	Bottom Injection
KATS	KIT (Germany)	1D	Thermite	Dry and Wet	Bottom Injection
ECOKATS	KIT (Germany)	2D	Simulants	Dry	Bottom/Side Injection
COMAS	Siempelkamp (Germany)	1D, 2D - channel	Corium	Dry	Bottom Injection

FARO	JRC Ispra (European Commission)	19 degree sector/Debris Bed	Corium	Dry and Wet	Jet
VULCANO	CEA (France)	2D-channel	Corium	Dry	Bottom Injection
NSSL	Hokkaido University (Japan)	3D	Simulants	Dry and Wet	Jet/Free Fall

## 2. Experimental Conditions Description (Sahboun et al. 2020)

From Sehgal et al. (2012), it can be deduced that, during the displacement of the corium, the breach diameter  $D_{breac}$  could reach up to 40 cm. As for the accident's falling height  $H_{accidentfalling}$ , in the case of a Boiling Water Reactor (BWR), it could vary from 7 to 11 m and, in the case of a Pressured Water Reactor (PWR), it could vary from 1 to 2 m. Therefore, the accidental scaling coefficient  $K_{accident}$ , defined as  $K_{accident} = \frac{H_{accidentfalling}}{D_{breac}}$ , will vary from 17.5 to 27.5 from the BWR case and from 2.5 to 5 in the case of PWR.

As the present work follows the previous experiments performed at Hokkaido University (Miwa et al. (2018), Ogura et al. (2018a and b), Matsumoto et al. (2017) and Sahboun et al. (2020)), experiments were conducted with the test section shown in Fig 4.1 and Fig 4.2 under the set up tabulated in Table 4.2. By applying the previously mentioned accidental scaling coefficient to the experimental setting, it can be found that it varies from 8 to 125. Thus, it can be concluded that the geometrical setting is comparable to the BWR's.

For the selection of the specimen, utilization of pure metal was considered in this study. Since the aim of this study is to provide fundamental dataset for the severe accident code validation, samples with well-known physical properties were selected. To serve that purpose, molten Copper (Cu) and Tin (Sn) were chosen as simulants for molten core spreading safety assessment. The molten Cu was utilized in a previous study (Ogura et al. (2018a and b)). The Sn was utilized for the comparison, which has different physical properties, such as density and viscosity, as well as a lower melting temperature as show in Table 4.2.

Table 4.2. Experimental parameters for molten metal experiment. (Sahboun et al., 2020)

Fall height, $H$ [mm]	100.0–500.0
Nozzle outlet diameter, $D_0$ [mm]	4.0–12.5
Molten metal mass, $m_d$ [kg]	For Copper: from 0.075 to 0.45  For Tin: from 0.05 to 1.05
Molten metal initial temperature, $T_0$ [K]	For Copper: 1,380  For Tin: 510
Melt density, $\rho$ [kg/m <sup>3</sup> ]	Copper: 7,900  Tin: 7,000
Melt surface tension, $\sigma$ [mN/m]	Copper: 1,280  Tin: 544
Melt dynamic viscosity, $\mu$ [mPa s]	Copper: 4  Tin: 1.87
Plate initial temperature, $T_p$ [K]	373.0
Surrounding temperature [K]	293.0

The test section is separated into two parts: the upper section is the molten metal containment/generation section and the lower section contains spreading plates with adjustable height mechanism and temperature control with an embedded heater. Using the high-frequency induction heater installed at the upper portion, the simulant material melts inside a graphite crucible.

When the stimulant is fully liquefied, the molten metal flow is initiated by removing the plug located in the spreading nozzle, letting the simulant drop and spread over a steel plate in the lower section. The experiments were performed under an argon atmosphere at an atmospheric pressure to assure that oxidation is prevented. Experimental data, which consists of the maximum spreading area after the solidification and jet breakup length, was acquired through high-speed camera recording. A sample of this recording can be seen in the Fig 4.3.

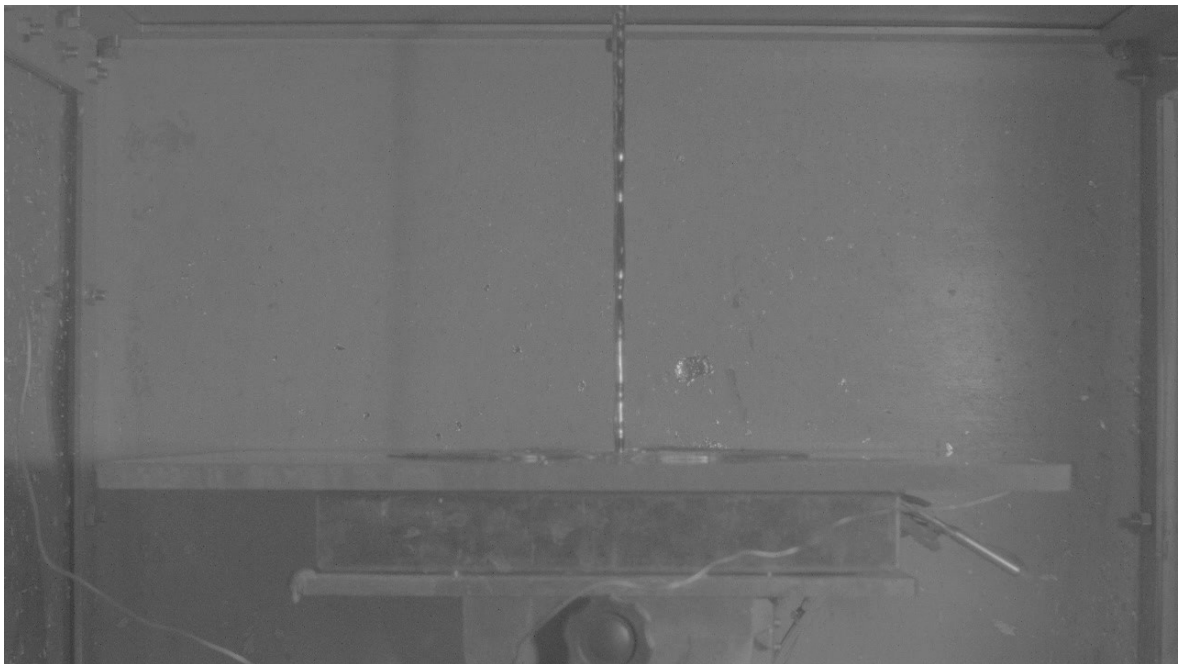


Fig 4.3. Lateral view of the experiment recording (Sahboun et al. 2020)

### 3. Maximum Spreading Ratio of Molten Metal

Previous works (Sahboun et al. 2019 and 2020) had allowed to determine that the jet instability involved in the experiment is a second-wind induced instability regime and the jet breakup length is a value that impact the maximum spreading ratio drastically.

Therefore, a methodology was developed for the evaluation of this impact with, as a first step, the calculation of characteristic numbers such as the Reynolds, Weber and Ohnesorge numbers to clarify which jet breakup formulation should be used, followed by a second step where the jet break-up length is calculated from the selected formulation. In the selected experimental setting, the tabulated Weber number varied between 57 and 1,019 for Copper cases and, between 114 and 2,030 for Tin cases. Knowing that  $Re > 10,000$  a.k.a turbulent condition for both samples, the theory developed by Sallam et al. (2002) allows inferring that the jet breakup is in the turbulent category and the correlation between jet breakup length  $L_j$  and jet diameter  $D_0$  can be expressed as:

$$\frac{L_j}{D_0} = C(We^{0.5})^{0.64} \quad (4.1)$$

where C is the non-dimensional coefficient assumed to be 8.51 for  $We \in [100; 10000]$  as described in Sallam et al. (2002) and Grant et al. (1996) papers. Experiments were done to validate the selected value of C and the results are tabulated in Table 4.3a and Table 4.3b. The conclusion that can be drawn from the result is that the selected value of  $C = 8.51$  allows an accurate prediction of the jet-breakup with an error margin of up to 10 %.

Table 4.3a Jet-breakup length formulation error assessment for  $C = 8.51$

(Tested material: Tin,  $D_0 = 4$  mm,  $H = 300$  mm,  $m_d = 0.35$  kg) (Sahboun et al. 2020)

	Set 1	Set 2	Set 3
Weber Number	218	218	218
Theoretical Value (mm)	209	209	209

Exp Value (mm)	194	218	207
Error (%)	8	4	0.77

Table 4.3b Jet-breakup length formulation error assessment for C = 8.5

(Tested material: Copper ,  $D_0 = 4$  mm,  $H = 300$  mm,  $m_d = 0.35$  kg) (Sahboun et al. 2020)

	Set 1	Set 2	Set 3
Weber Number	153	153	153
Theoretical Value (mm)	170	170	170
Exp Value (mm)	181	173	185
Error (%)	6	2	8

From there, the assumption used to include jet-breakup into the formulation for the maximum spreading ratio  $\xi_{max}$  is that the jet is fully driven by gravity, but the jet break-up impacts the velocity profile by changing the falling height H. The modified falling height  $H_{fmod}$  after break-up, as theorized in Sahboun et al. (2020), can be written in the following manner:

$$H_{fmod} = H * f\left(\frac{L_j}{H}\right) \quad (4.2)$$

From there, it is possible to write the modified velocity of the jet  $V_{mod}$  after the break-up as following:

$$V_{mod} = \sqrt{2gH_{fmod}} = \sqrt{f\left(\frac{L_j}{H}\right)} V_0 \text{ with } V_0 = \sqrt{2gH} \quad (4.3)$$

Where  $V_0$  is the original velocity of the jet before the break-up. Moreover, the function  $f$  is the relative position of the breakup along the original falling height  $H$  and can be defined as following:

$$f\left(\frac{L_j}{H}\right) = 1 - 0.5e^{-\frac{\left(\frac{L_j}{H}-0.5\right)^2}{2*M^2}} \quad (4.4)$$

**with  $M = 1$**

Therefore, the characteristic numbers such as Weber, Reynolds and Peclet numbers can be rewritten as:

$$We_{mod} = f\left(\frac{L_j}{H}\right) We_0 \text{ with } We_0 = \frac{\rho V_0^2 D_0}{\sigma} \quad (4.5)$$

$$Re_{mod} = \sqrt{f\left(\frac{L_j}{H}\right)} Re_0 \text{ with } Re_0 = \frac{\rho V_0 D_0}{\mu} \quad (4.6)$$

$$Pe_{mod} = \sqrt{f\left(\frac{L_j}{H}\right)} Pe_0 \text{ with } Pe_0 = Re_0 Pr \quad (4.7)$$



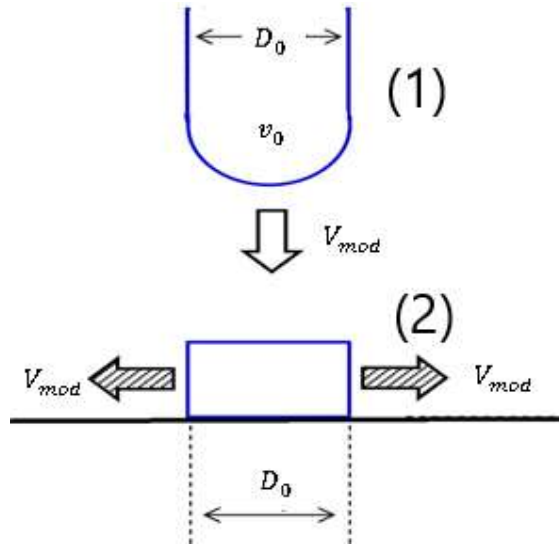


Fig 4.4. Schematic of jet impingement on solid surface (Sahboun et al. 2020)

Similar to the model proposed by Aziz et al. (2000), the formulation for the present study starts with a classic energy balance equation between state 1 (before the impact) and state 2 (after the impact) as shown in Fig 4.4. This energy balance can be expressed as follows:

$$KE_1 + SE_1 = SE_2 + W + \Delta KE \quad (4.8)$$

Where  $KE_1$  corresponds to the initial kinetic energy,  $SE_1$  the surface energy of the liquid jet before the impact,  $SE_2$  the surface energy of the spread,  $W$  the work done in deforming the jet under the influence of viscosity and  $\Delta KE$  the loss of kinetic energy.

In the case of state 1, the focus is put on the jet kinetic and surface energies. In this instance, the deformation of the molten material is assumed to happen mostly in the jet area of the flow, here approximated by a cylinder of diameter  $D_0$ , height  $H$  and terminated by a demi-sphere of diameter  $D_0$ . Therefore, the initial kinetic energy  $KE_1$  and the surface energy  $SE_1$  can be expressed as follows:

$$KE_1 = \left( \frac{1}{2} \rho V_{mod}^2 \right) \left( \frac{\pi}{12} D_0^3 + \frac{1}{4} \pi H D_0^2 \right) \quad (4.9)$$

$$SE_1 = \sigma \left( \frac{\pi}{2} D_0^2 + \pi H D_0 \right) \quad (4.10)$$

Following the impact, when investigating the maximum extension of the jet, the molten metal velocity is assumed to be zero meaning that the kinetic energy is zero. Hence, the surface energy  $SE_2$  can be expressed as follows:

$$SE_2 = \frac{\pi}{4} D_{max}^2 \sigma (1 - \cos(\theta_a)) \quad (4.11)$$

Where  $\theta_a$  is the advancing liquid-solid contact angle, assumed to be  $140^\circ$  in the current study, similarly to Aziz et al. (2000) work.

For the change in the energy state following the impact, the loss of kinetic energy is assumed to be due to the melt's solidification over the spreading plate. Therefore, this loss can be approximated by the following formulation:

$$\Delta KE = \left( \frac{\pi}{4} d_s^2 s \right) \left( \frac{1}{2} \rho V_{mod}^2 \right) \quad (4.12)$$

Where  $s$  is the solid layer average thickness and  $d_s$  the diameter when the splat is at its maximum extension, assumed to be approximately  $D_{max}/2$ .

As for the work  $W$  done in deforming the jet, it is assumed to be expressed by the following relation:

$$W = \frac{\pi}{3} \rho V_{mod}^2 D_0 D_{max}^2 \left( 1 + \frac{3H}{4D_0} \right) \left( \frac{1}{\sqrt{Re_{mod}}} \right) \quad (4.13)$$

By substituting Eqs (4.9) to (4.13) into Eq. (4.8), the following relation can be obtained:

$$\begin{aligned}
& \left(\frac{1}{2}\rho V_{mod}^2\right)\left(\frac{\pi}{12}D_0^3 + \frac{1}{4}\pi HD_0^2\right) + \sigma\left(\frac{\pi}{2}D_0^2 + \pi HD_0\right) \\
& = \frac{\pi}{4}D_{max}^2\sigma(1 - \cos(\theta_a)) \\
& + \frac{\pi}{3}\rho V_{mod}^2 D_0 D_{max}^2\left(1 + \frac{3}{4}\frac{H}{D_0}\right) \\
& + \left(\frac{\pi}{4}d_s^2 s\right)\left(\frac{1}{2}\rho V_{mod}^2\right)
\end{aligned} \tag{4.14}$$

From Eq. (4.14), it is possible to express the maximum spreading ratio as:

$$\begin{aligned}
\xi_{max} & = \frac{D_{max}}{D_0} \\
& = \sqrt{\frac{\frac{1}{2}\left(1 + 3\frac{H}{D_0}\right)We_{mod} + 12\left(\frac{1}{2} + \frac{H}{D_0}\right)}{We_{mod}s^* + 3(1 - \cos(\theta_a)) + 4\left(1 + 3\frac{H}{D_0}\right)\frac{We_{mod}}{\sqrt{Re_{mod}}}}}
\end{aligned} \tag{4.15}$$

Where  $Re$  is the Reynolds number defined as  $Re = V_0 D_0 / \nu$  and  $s^*$  the dimensionless solid layer thickness ( $s^* = s / D_0$ ). Using the approximate analytical solution developed by Poirier et al. (1994), the dimensionless solid layer thickness can be expressed as a function of the Stephan number, Peclet number and the thermal properties of the involved phases  $\gamma$  ( $\gamma = k\rho c_p$ ):

$$s^* = \frac{2}{\sqrt{\pi}} Ste \sqrt{\frac{t^* \gamma_{substrat}}{2\pi Pe \gamma_j}} \tag{4.16}$$

With the help of equation (4.16), it is possible to re-write equation (15) in the following fashion:

$$\xi_{max} = \sqrt{\frac{\frac{1}{2} \left(1 + 3 \frac{H}{D_0}\right) We_{mod} + 12 \left(\frac{1}{2} + \frac{H}{D_0}\right)}{We_{mod} \sqrt{\frac{3Ste}{4Pe_{mod}}} + 3(1 - \cos(\theta_a)) + 4 \left(1 + 3 \frac{H}{D_0}\right) \frac{We_{mod}}{\sqrt{Re_{mod}}}} \quad (4.17)$$

However, this new formulation has a main drawback of inability to predict accurately the impact of the molten material initial drop mass on the maximum spreading ratio as shown in Fig 4.5 and 4.6.

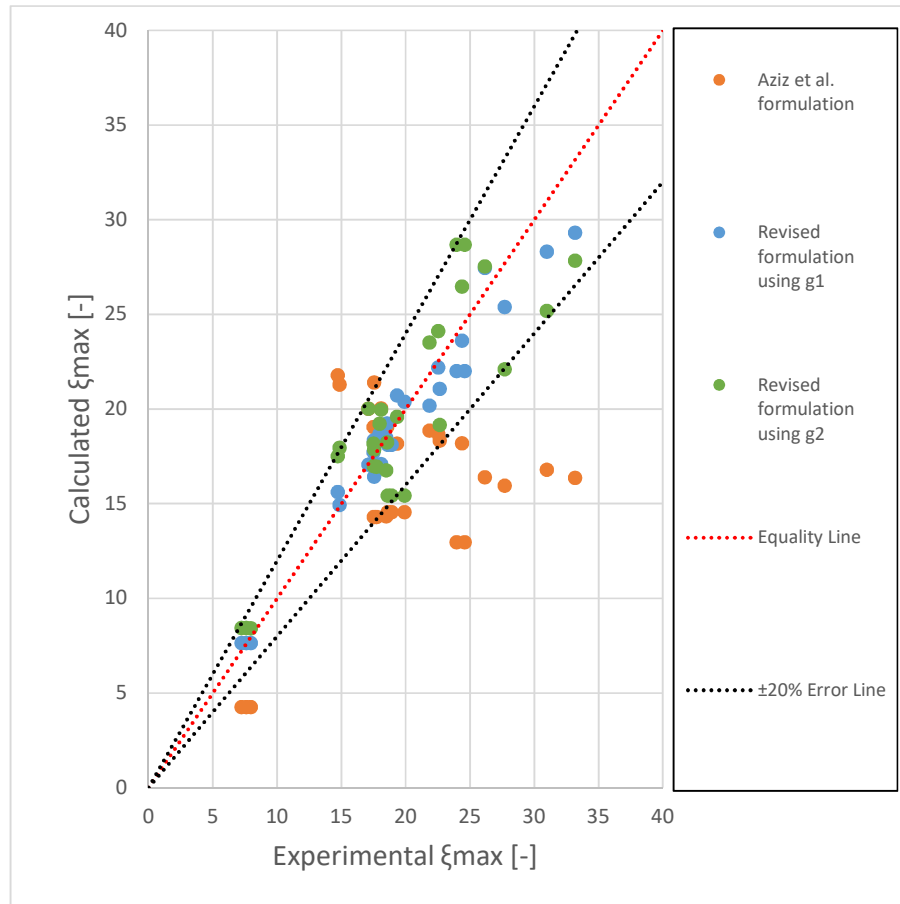


Fig 4.5. Prediction assessment of the different maximum spreading ratio formulations for Copper cases ( $D_n=D_0$ ) (Sahboun et al. 2020)

Therefore, the next step is to build a correction function  $g_1$  that modify the spreading expression as follows:

$$\xi_{max} = \frac{g_1(m_d, D_0)}{\sqrt{We_{mod} \sqrt{\frac{3Ste}{4Pe_{mod}} + 3(1 - \cos(\theta_a))} + 4 \left(1 + 3 \frac{H}{D_0}\right) \frac{We_{mod}}{\sqrt{Re_{mod}}}}} \left( \frac{1}{2} \left(1 + 3 \frac{H}{D_0}\right) We_{mod} + 12 \left(\frac{1}{2} + \frac{H}{D_0}\right) \right) \quad (4.18)$$

Where the function  $g_1$  is first defined as:

$$g_1(m_d, D_0) = a(D_0) * m_d^{b(D_0)} \quad (4.19)$$

Where a and b are coefficients dependent on the nozzle diameter  $D_0$  and molten material type.

In the original Aziz and Chandra's work (2000), the droplets used in their experiments had a limited time of existence and a small volume, meaning the interface deformation was of a time-scale small enough to consider it instantaneous. In the present work, the studied jet has a lifetime non-negligible, meaning that the interface will see deformation through the integrality of its existence.

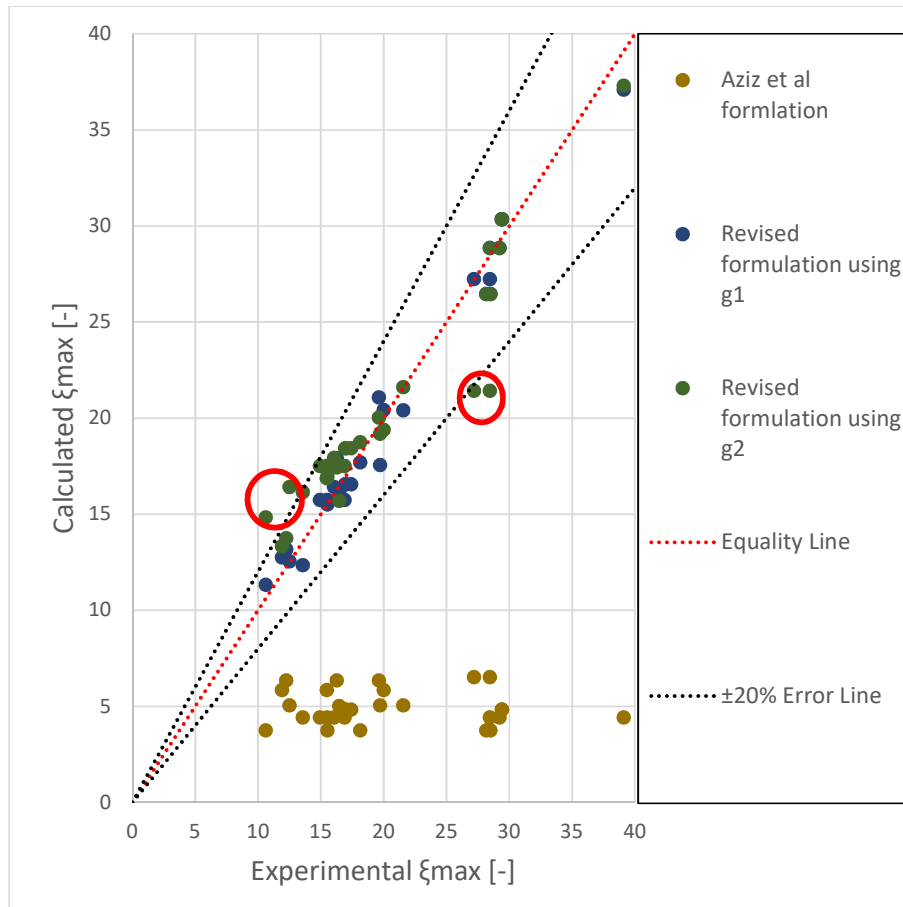


Fig 4.6. Prediction assessment of the different maximum spreading ratio formulations for Tin cases ( $D_n = D_0$ ) (Sahboun et al. 2020)

Therefore, from the experiment behavior, it is possible to interpret the function  $g_1$  as the empirical modification of the spreading expression to take into account the impact of the jet interface deformation over its lifetime.

In an attempt to simplify the maximum spreading ratio expression, a comparison of each component was realized. For this comparison, each component was named in the following matter:

$$A = \frac{1}{2} \left( 1 + 3 \frac{H}{D_0} \right) We_{mod} \quad (4.20)$$

$$B = 12 \left( \frac{1}{2} + \frac{H}{D_0} \right) \quad (4.21)$$

$$E = We_{mod} \sqrt{\frac{3Ste}{4Pe_{mod}}} \quad (4.22)$$

$$F = 3(1 - \cos(\theta_a)) \quad (4.23)$$

$$G = 4 \left(1 + 3 \frac{H}{D_0}\right) \frac{We_{mod}}{\sqrt{Re_{mod}}} \quad (4.24)$$

Using the data collected through the experiments for both Copper and Tin, it is possible to conclude that, in the ratio expressed in Eq 4.18, A and G are the dominant terms for respectively the numerator and denominator of the ratio. Therefore, it is possible to simplify Eq 4.18 in the following manner:

$$\xi_{max} \approx g_1(m_d, D_0) \frac{Re_{mod}^{\frac{1}{4}}}{2\sqrt{2}} \quad (4.25)$$

To refine the definition of the correction function, an attempt was made to build a dimensionless time  $t_j^*$  defined as the ratio between the jet's lifetime  $t_j$  and the characteristic time  $t_0$  which is defined as the ratio between the initial jet velocity  $V_0$  and the nozzle diameter  $D_0$ , in a similar fashion to Aziz et al. work (2000). Therefore, a proper definition of  $t_j$  is required and it can be written as:

$$t_j = \frac{v_0}{Q} \quad (4.26)$$

Where  $v_0$  is the initial volume of molten material and  $Q$  the volumetric flow rate of molten metal through the experiment's nozzle. Both of them can be written as:

$$v_0 = \frac{m_d}{\rho_{liqmetal}} \quad (4.27)$$

$$Q = V_0 * \pi * \frac{D_0^2}{4} \quad (4.28)$$

From there, it is possible to write  $t_j$  in the following manner:

$$t_j = \frac{4m_d}{\pi V_0 \rho_{liqmetal} D_0^2} \quad (4.29)$$

As for  $t_0$ , it can be written as:

$$t_0 = \frac{D_0}{V_0} \quad (4.30)$$

Therefore,  $t^*_j$  can be written as:

$$t^*_j = \frac{4m_d}{\pi \rho_{liqmetal} D_0^3} \quad (4.31)$$

From there, a comparison with the experimental data collected for Tin and Copper allows to build, with fair accuracy, the following refined formulation for the correction function:

$$g_2(t^*_j) \approx \varepsilon \sqrt{t^*_j} + \beta \quad (4.32)$$

Where  $\varepsilon$  and  $\beta$  are experimental coefficients only dependent of the molten material nature. Their values for the investigated materials in this paper, respectively Tin and Copper, can be found in Table 4.4.

Table 4.4: Experimental coefficient for the empirical function  $g_2$ (Sahboun et al. 2020)

	<b>Experimental coefficient <math>\varepsilon</math></b>	<b>Experimental coefficient <math>\beta</math></b>	<b>Linear Approximation Error R</b>



<b>Tin</b>	0.0776	0.9978	93.07%
<b>Copper</b>	0.1829	2.0600	85.93%

From the experiments, the measurements of each sample's maximum diameters were realized through the use of area measurement and equivalent diameter calculation on images such as Fig 4.7.

A comparison between the experimental and theoretical values of the maximum spreading ratio was built as shown in Figures 4.5 and 4.6, respectively for Tin and Copper. The predicted values using the function  $g$  initial formulation have, for both Tin and Copper cases, a  $\pm 20\%$  error margin or better.

While the predicted values using  $t^*_j$  have, for most, a  $\pm 20\%$  error margin but it is important to notice that for Tin cases, this margin is not respected for two cases, circled in red in Figure 4.6. Both cases are suspected to be extreme ones, knowing that the smallest drop mass (0.05 kg) and largest drop mass (1.05 kg) were used for the left and right circled data points respectively.



Fig 4.7. Tin Spreading Sample (Sahboun et al. 2020)

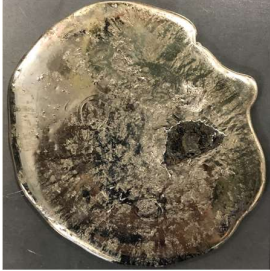





Therefore, it is assumed that they are illustrated the limitation of the build expression or experimental setting. Moreover, this error margin, in the case of Copper, seems to be greatly due to the linear approximation error of  $g_2$ . Moreover, as it was noted by Aziz et al. (2000), the gravity-driven spreading of molten material is subject to the formation of what is called fingers, more noticeable for Copper than for Tin, as shown in Table 4.5.

Adjusting the formulation provided by Aziz et al. (2000) to the studied geometry and involved phenomena, a formulation to determine the number of fingers in the case of a molten metal jet spreading can be written as followed:

$$N = \xi_{max} \sqrt{\frac{We_{mod}}{C_N t_j^*}} \quad (4.33)$$

Where the coefficient  $C_N$  is an empirical coefficient depending of the spreading surface, as reported in Bholas et al. (1999) and Tang et al. (2017) papers. With the current expression of the coefficient  $C_N$ , it was possible to build a comparison between the formulation proposed by Aziz et al. (2000) and the above formulation.

Table 4.5: Finger formation assessment for  $D_0 = 0.004\text{ m}$  and  $m_d = 0.4\text{ kg}$  (Sahboun et al. 2020)

	
<b>Tin Set 1</b>	<b>Copper Set 1</b>
	
<b>Tin Set 2</b>	<b>Copper Set 2</b>
	
<b>Tin Set 3</b>	<b>Copper Set 3</b>

As shown in Fig 4.8, the formulation from Aziz et al. (2000) over-predicted the finger number drastically compared to the built formulation. In its current form, the built formulation can predict the finger number for a given experimental configuration with an error margin of 20% at worst. Still, this error margin is highly dependent on the empirical

number  $C_N$ . Therefore, as the finger formation drastically impacts Copper spreading behavior, future experiments will be realized to provide an expression for the coefficient  $C_N$  as a function of the spreading plate average roughness  $R_a$ , similarly to Tang et al. (2017) work. From Wang et al (2002), Dhiman et al (2005), and Shakeri et al (2002) works, it was found that roughness impacts molten tin spreading by introducing a thermal contact resistance between the molten metal and the spreading plate. The value of this resistance varies greatly with the plate's roughness and can either enhance or prohibit the splashing phenomenon.

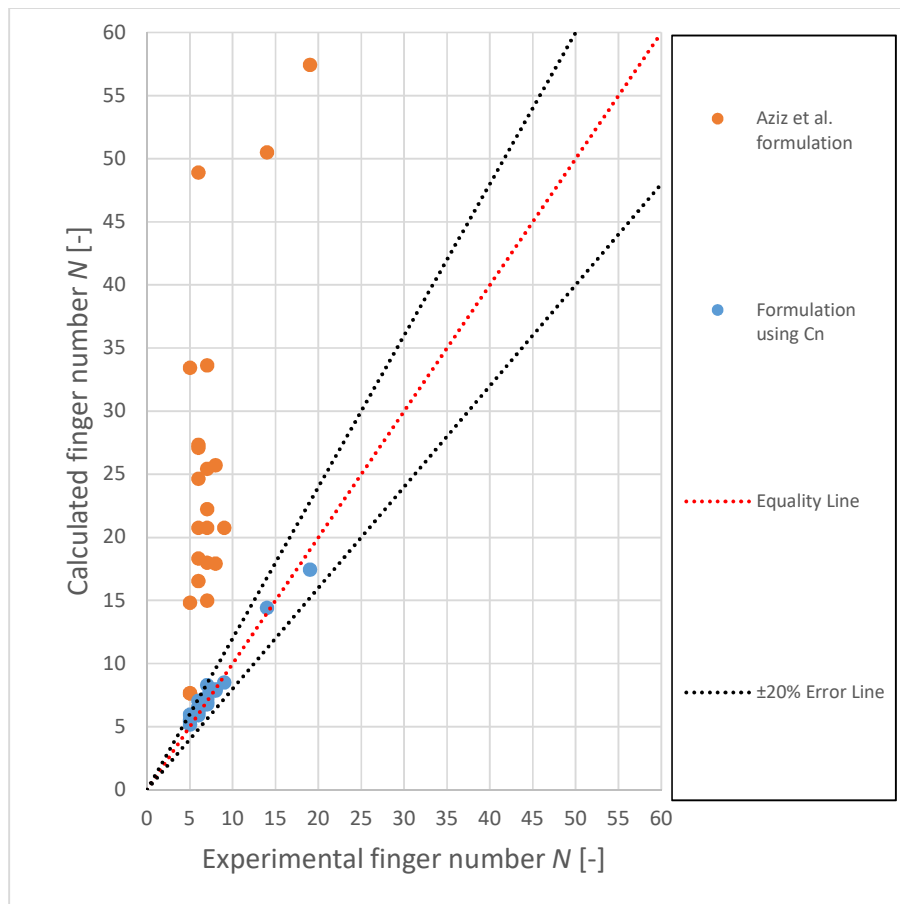


Fig 4.8. Prediction assessment of the finger number formulations for Copper cases (Sahboun et al. 2020)

Moreover, it was found that the roughness impacts finger formation greatly. It is especially apparent with Copper experiments as shown in Table 4.5. In those experiments, a roughness increase was characterized by a decrease in the finger number but an increase in their length.

According to this assessment, a revision of the maximum spreading is therefore necessary. Dhiman et al. (2005) proposed a more detailed formulation of the spread thickness  $s$  as a function of the thermal contact resistance  $R_c$  that is itself dependent on the spreading plate as mentioned previously. From that work, the spread thickness  $s$  can be written as follows:

$$s = \frac{2}{\sqrt{\pi}} \frac{(T_m - T_{sub})}{\rho_{jet} H_{f,j}} \sqrt{\gamma_{sub} t_j} \left( 1 - R_c \sqrt{\frac{\gamma_{sub}}{\pi t_j}} \ln \left( 1 + \frac{1}{R_c} \sqrt{\frac{\pi t_j}{\gamma_j}} \right) \right) \quad (4.34)$$

Using the Biot number defined as  $Bi = \frac{D_0}{k_j R_c}$ , it is possible to write the dimensionless thickness  $s^*$  in the following manner:

$$s^* = \frac{2}{\sqrt{\pi}} Ste \sqrt{\frac{\gamma_{sub} t_j^*}{\gamma_j Pe}} \left( 1 - \frac{1}{Bi} \sqrt{\frac{\gamma_{sub} Pe}{\gamma_j \pi t_j^*}} \ln \left( 1 + Bi \sqrt{\frac{\gamma_j \pi t_j^*}{\gamma_{sub} Pe}} \right) \right) \quad (4.35)$$

Preliminary results for the available experimental database with some assumption for the value of  $R_c$  (based on Wang et al (2002), Dhiman et al (2005) and Shakeri et al (2002) works) can be found in the following Fig 4.9 and 4.10:

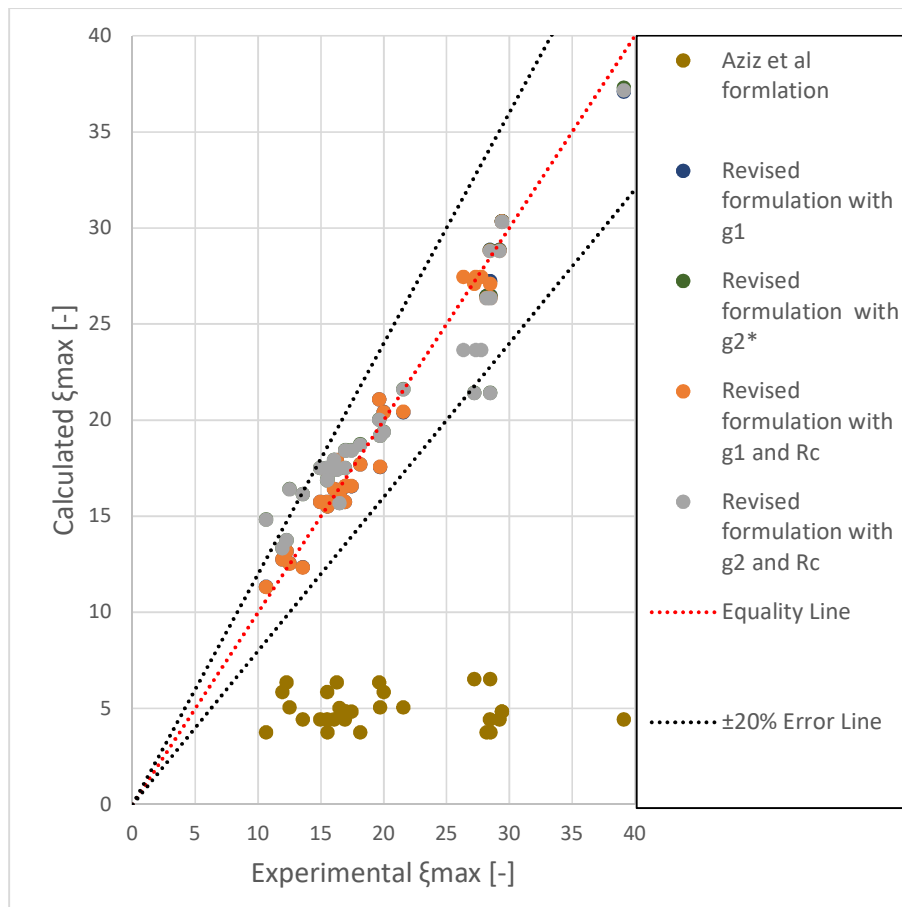


Fig 4.9 Prediction assessment of the different maximum spreading ratio formulations for Tin cases ( $D_n = D_0$ )

The conclusion that can be drawn is that, in the case of tin, the impact of the new formulation is small but improve the prediction slightly. In the other hand, for copper, the impact of the new formulation is significant and can lead, if the value of  $R_c$  is known with a higher accuracy, to an improvement of the formulation accuracy.

On a side-note, Bhola et al. (1999) proposed an additional formulation on a phenomenon complementary of the fingers formation: recoil. Only observed partly in the experiments for the smallest drop mass, it is still important to investigate this phenomenon.

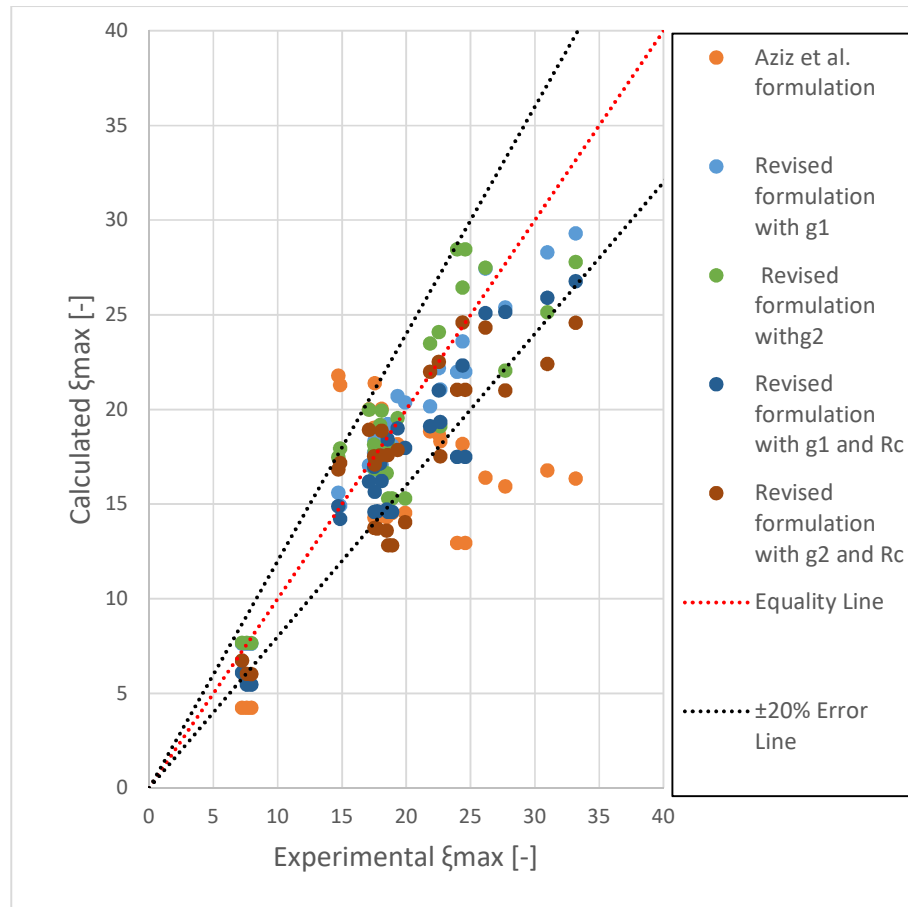


Fig 4.10. Prediction assessment of the different maximum spreading ratio formulations for Copper cases ( $D_n=D_0$ )

In this extend, it was elected to use the normalized residual surface energy  $\Psi$  defined by Bhola et al. (1999) in the following manner:

$$\Psi = \frac{SE_2}{KE_1 + SE_1} \quad (4.36)$$

Using the formulation built for  $KE_1$ ,  $SE_1$  and  $SE_2$ , it is possible to rewrite  $\Psi$  in the following fashion:

$$\Psi = \xi_{max}^2 \frac{1 - \cos(\theta_a)}{\left(2 + 4\frac{H}{D_0}\right) + \frac{1}{6}\left(1 + 3\frac{H}{D_0}\right) We_{mod}} \quad (4.37)$$

With the available data, it was possible to build a comparison on potential recoil behavior between copper and tin cases as shown in Fig 4.11.

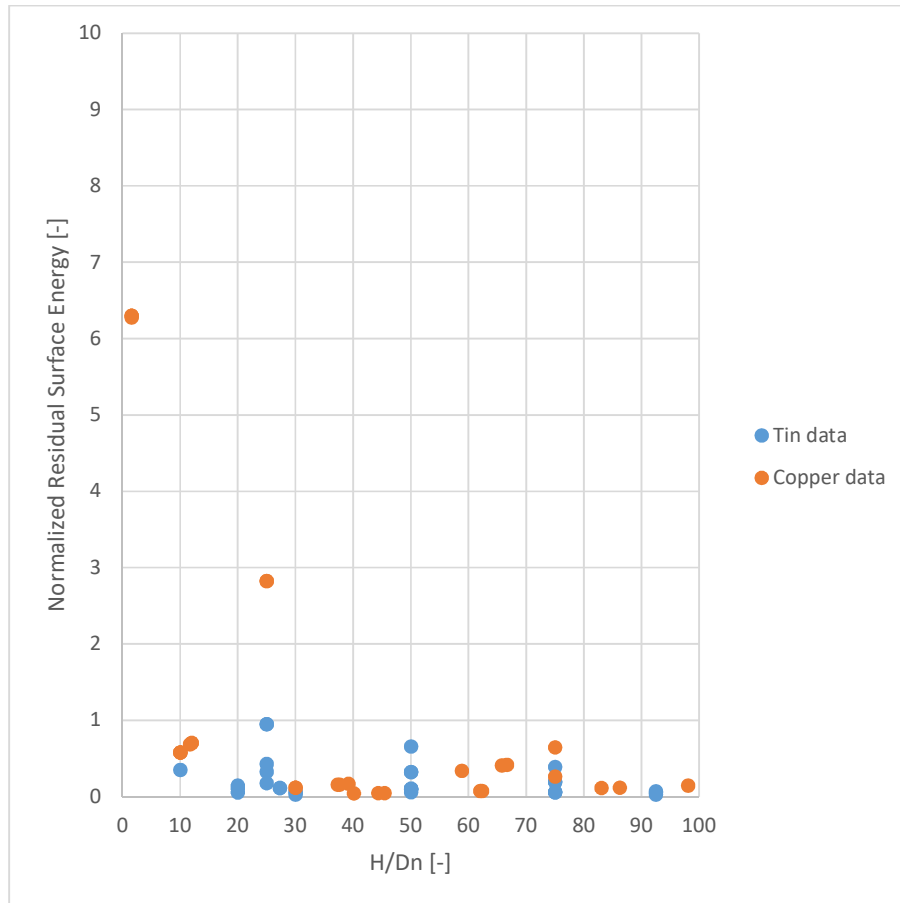


Fig 4.11. Recoil as a function of the accidental coefficient ( $Dn=D_0$ )

For Fig 4.11, it can be concluding that, as the accidental coefficient grows, the corresponding residual surface energy decreases, meaning that recoil has fewer chances to occur in those configurations.



However, in the case of a small accidental coefficient, this residual energy is non-negligible and could be detrimental to the spreading assessment.

In addition to the finger formation, two other minor phenomena were seen in the Copper experiments: splashing and melt-through. For the splashing, it can be linked, similarly to the finger formation, to the spreading plate roughness as it was illustrated by Tang et al. (2017) work. However, its impact on the spreading is negligible and only registered as a mass loss inferior to 5% for all the Copper's samples.

As for the melt-through, the assumption is that a high heat transfer happens in the impingement region, meaning that the spreading plate in this area could and has reached, in some of the Copper experiment, the melting point. It is in accord with Zuckerman et al. (2006) work. This melt-through depth is of the order of a few millimeters and for a circular area of diameter 5 times the size of the nozzle diameter  $D_0$  at worst. However, its impact on the spreading is negligible but could be of interest for future studies.

# Chapter 5: Simulation Work

## 1. Introduction

As it is common knowledge now, one of the major drawbacks of nuclear energy during the severe accident is the ability to predict core meltdown and its spreading/solidification behaviors. The conclusion of such event is often, as past accident and related research projects have shown from Three Mile Island (TMI) (Dinh et al., 2000) to Fukushima (Miwa et al., 2018), the displacement of the molten core, also known as corium, to the lower region of the reactor building and in some cases, the lost to the outside world of the molten core.

Therefore, to assure the safety of the public and the non-release of radio-active elements to the environment, it will be important to add to the reactor building a feature that retain and keep the spreading molten core in a confined and cooled state. Such a feature was devised through the years under the name of core-catcher. The principal behind it is the following: allow the molten core to spread in a large plane area installed adjacent to the Containment Vessel (CV).

Experimentation and simulation to investigate the spreading of the molten core over plane area for the design and enhancement of the core-catcher technology were conducted in different countries by a multitude of agencies and Universities (Dinh et al., 2000) since TMI.

Most of those experiments/simulations were focused on getting information on molten core spreading behavior and boundary condition for molten core concrete interaction (MCCI). As such, most of the core spreading experiments were performed using actual corium or simulant on sacrificial material from side or bottom injection as summarized in Table 5.1.

At the same time, those experiments also reached a step that allow them to define scaling coefficient for molten core spreading especially for the spreading length. Like it is underlined previously, those works were done under simplified condition or physics meaning that the corresponding scaling coefficient are therefore less realistic. That was true up until recently, as the works done previously in Hokkaido University by Matsumoto et al. (2017) and Ogura et al (2018 a, b) took into account spreading under downward jet on dry and wet flat surface meaning that work included gravity driven spreading plus collisional impact between spreading material and the surface as shown in Fig 5.1. In the continuation of such a work, in this chapter, the focus will be to simulate such spreading with the commercial software Star CCM+ and secondly extend the previous experimental work for those simulations' validation.

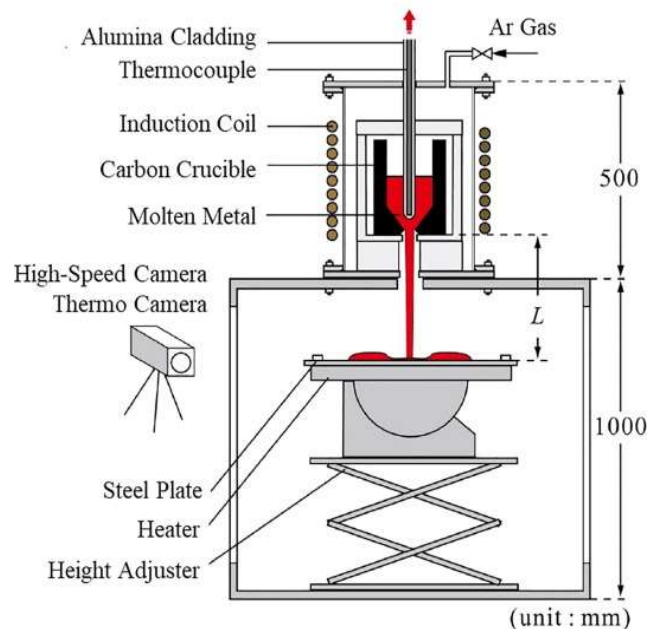


Fig. 5.1. Schematic of the test section for molten metal spread experiment (Matsumoto et al. 2017, Ogura et al. 2018a and b, Sahboun et al. 2020)

Table 5.1. Experimental programs on molten metal spreading (Dinh et al, 2000)

	Institution	Geometry	Melt	Surface Condition	Injection Method
CORINE	CEA (France)	2D-channel	Stimulants	Dry	Bottom Injection
BNL	BNL (USA)	2D area	Pb	Dry and Wet	Jet
S3E	KTH (Sweden)	1D, 2D area	Stimulants	Dry and Wet	Bottom Injection
SPREAD	Hitachi Energy Research Lab. (Japan)	1D, 2D area	Thermite	Dry	Bottom Injection
KATS	KIT (Germany)	1D	Thermite	Dry and Wet	Bottom Injection
ECOKATS	KIT (Germany)	2D	Stimulants	Dry	Bottom/Side Injection
COMAS	Siempelkamp (Germany)	1D, 2D - channel	Corium	Dry	Bottom Injection
FARO	JRC Ispra (European Commission)	19 degree sector/Debris Bed	Corium	Dry and Wet	Jet
VULCANO	CEA (France)	2D-channel	Corium	Dry	Bottom Injection

## NOMENCLATURE

$A$	Surface Area	$[\text{m}^2]$
$S$	Surface	$[\text{m}^2]$
$V$	Volume	$[\text{m}^3]$
$v$	Velocity	$[\text{m/s}]$
$c_p$	Specific heat capacity	$[\text{J/kg/K}]$
$s_{\alpha_i}$	Source or sink term	$[-]$
$Ca$	Capillary Number	$[-]$
$Oh$	Ohnesorge number	$[-]$
$Re$	Reynolds number	$[-]$
$We$	Weber number	$[-]$
$D$	Jet diameter	$[\text{m}]$
$\theta_k$	Kistler contact angle	$[\circ]$
$\theta_s$	Static contact angle e	$[\circ]$
$f_{Hoff}$	is the Hoffman function	$[-]$
$N_n$	Cell Number of mesh n	$[-]$
$r_{nk}$	Mesh refinement factor between meshes n and k	$[-]$
$\varphi_n$	Variable obtained with mesh n	$[\text{depend of the variable}]$
$p$	Apparent order	$[-]$

$\varphi_{ext}^{kn}$  Extrapolated values from the values obtained with meshes n and k [depend of the variable]

$e_a^{kn}$  Approximate relative error between meshes n and k [-]

$e_{ext}^{kn}$  Extrapolated relative error between meshes n and k [-]

$GCI_{fine}^{kn}$  Fine-grid convergence index between meshes n and k [-]

### Greek letters

$\alpha$  Volume fraction [-]

$\rho$  Density [kg/m<sup>3</sup>]

$\mu$  Viscosity [Pa s]

$\sigma$  Surface tension [N/m]

### Subscripts

g gas phase

l liquid phase

j jet

n, k Mesh index number with n≠k

## 2. Simulation Model Description

First and foremost, as it is previously mentioned, the focus of this study are molten metal spreading simulation and the validation of those simulations against up-to-date experiments. To be more precise, as this chapter's work follows the work done in Hokkaido University by Ogura et al. (2018a and b), the scope is to investigate the

spreading of molten Copper (Cu) and Zinc (Zn) as simulants for molten core spreading safety assessment. To do so, experiments were conducted with the experimental apparatus shown in Fig.5.2 under the conditions summarized in Table 5.2.

As it is, the experiment is separated in two sections: the first one will be the molten metal containment/generation section and the second one be the lower spreading section. Under the action of a high frequency induction heater, the simulant material is melt inside a graphite crucible. When the simulant is fully liquefied, the molten metal flow is initiated by removing the bottom plug located in the spreading nozzle, letting the simulant drop and spread over a steel plate in the lower section.

Everything was done under an argon atmosphere kept at an atmospheric pressure to assure that oxidation of the different metals is prevented. Data are therefore acquired through the recording by a high speed camera. Concerning the simulation, the current work used the experimental conditions and the apparatus geometry to build the simulated volume and its boundary conditions under Star CCM+ CAD software as shown in Fig 5.3.

Table 5.2. Experimental parameters for molten metal experiment. (Sahboun et al, 2020)

<b>Fall height, H [mm]</b>	100.0–500.0
<b>Nozzle outlet diameter, <math>D_0</math> [mm]</b>	4.0–12.5
<b>Molten metal mass, M [kg]</b>	<b>For Copper:</b> from 0.075 to 0.45 kg  <b>For Tin:</b> from 0.05 to 1.05 kg
<b>Molten metal initial temperature, <math>T_0</math> [K]</b>	<b>For Copper:</b> 1,373.77  <b>For Tin:</b> 505.08
<b>Plate initial temperature, <math>T_0</math> [K]</b>	373.0
<b>Surrounding temperature [K]</b>	293.0

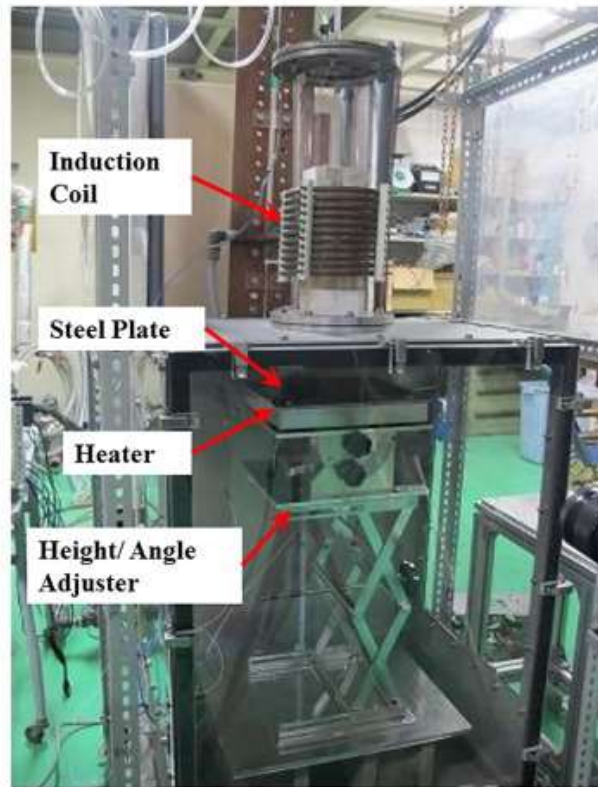


Fig. 5.2. Pictorial view of the test section for molten metal spread experiment (Matsumoto et al. 2017, Ogura et al. 2018a and b, Sahboun et al. 2020)

As well as the geometry and boundary conditions were given to the simulation, different models were selected from the wild array of possibilities in Star CCM+ mainly models for turbulence, solidification and multiphase flow phenomena as shown in Table 5.3.



Fig. 5.3. Volume Mesh used for Simulation



Table 5.3 Molten metal spreading Simulation Set-up

<b>Analysis code</b>	STAR-CCM+ (Ver.11)
<b>Discretization</b>	Finite-volume scheme
<b>Analysis approach</b>	Double precision
<b>Cell number</b>	Over 1.000.000
<b>Selected Model</b>	Realizable K- $\epsilon$ Eulerian Multiphase Implicit Unsteady Melting-Solidification Volume of Fluid (VOF) Continuum Surface Force (CSF)
<b>Wall Boundary Condition</b>	Container temp.: 505.08 K (for Tin cases) or 1373.77 k (for Copper cases) Spreading plate temp.: 373 K
<b>Pressure (Outlet)</b>	Atmospheric Air temp. : 293 K

In the present setting, we work with two immiscible phases (air and the molten metal) in a free fall and free surface situation with the solidification of one of the two phases. As we work with Star CCM+, it was found that only the Volume of Fluid (VOF) model allows us to simulate this setting. Therefore, in the current study, we choose this model for the multiphase flow phenomena as it has shown numerous advantages in its past

uses for molten core safety assessment studies (Dinh et al., 2000 and Kim et al. 2003 to 2016).

The VOF model, as treated in Star CCM+ User Guide, consist in the assertion that the usual set of equations are solved for an equivalent fluid whose physical properties are calculated as functions of the physical properties of its constituent phases and their volume fractions. Those properties are calculated as following:

$$\rho = \sum_i \alpha_i \rho_i \quad (5.1)$$

$$\mu = \sum_i \alpha_i \mu_i \quad (5.2)$$

$$c_p = \sum_i \frac{\rho_i}{\rho} \alpha_i c_{p_i} \quad (5.3)$$

Completed by a transportation equation for the volume fraction  $\alpha_i$  build in the following fashion:

$$\frac{\partial}{\partial t} \int_V \alpha_i dV + \int_s \alpha_i (\vec{v} - \vec{v}_g) \cdot \vec{dA} = \int_V \left( s_{\alpha_i} - \frac{\alpha_i}{\rho_i} \frac{D\rho_i}{Dt} \right) dV \quad (5.4)$$

where  $s_{\alpha_i}$  is the source or sink of the i-th phase, and  $\frac{D\rho_i}{Dt}$  is the material or Lagrangian derivative of the phase densities  $\rho_i$ . If a non-zero sharpening factor is specified, an additional term is added to the VOF transport equation:

$$\vec{\nabla} \cdot (\vec{v}_{c_i} \alpha_i (1 - \alpha_i)) \quad (5.5)$$

where:

- $\alpha_i$  is the volume fraction of phase i

- $\vec{v}_{c_i}$  is defined as follows:  $\vec{v}_{c_i} = C_a * |\vec{v}| \frac{\vec{\nabla}\alpha_i}{|\vec{\nabla}\alpha_i|}$

- $C_a$  is the sharpening factor that is specified in the Volume of Fluid (VOF) node properties.

- $\vec{v}$  is the fluid velocity

If there is a large time variation of phase volume fractions  $\alpha_i$ , there is a large time variation of the mixture density  $\rho$  which features in the continuity equation. Since this unsteady term cannot be linearized in terms of pressure and velocity, it acts as a large source term which can be “unpleasant” for a numerical treatment within a segregated solution algorithm. Therefore, the continuity equation is rearranged in the following, non-conservative form:

$$\int_s (\vec{v} - \vec{v}_g) \cdot d\vec{A} = \sum_i \int_V \left( s_{\alpha_i} - \frac{\alpha_i}{\rho_i} \frac{D\rho_i}{Dt} \right) dV \quad (5.6)$$

In the case when phases have constant densities and have no sources, the continuity equation reduces to  $\vec{\nabla} \cdot \vec{v} = \mathbf{0}$ .

In addition, as this study works with free-interface flow, it is necessary to include a formulation for the surface tension force. As a reminder, the surface tension force is a tensile force tangential to the interface separating two fluids, in the present case molten metal and air. It works to keep the fluid molecules at the free surface in contact with the rest of the fluid.

The surface tension force is an interfacial force, which is modeled as a volumetric force using the Continuum Surface Force (CSF) approach built by Brackbill et al. (1992).

In this approach, the magnitude of the surface tension force depends mainly on the nature of the fluid pair and on temperature. For a curved interface, the surface tension force  $\vec{f}_\sigma$  can be resolved into two components:

$$\vec{f}_\sigma = \vec{f}_{\sigma,n} + \vec{f}_{\sigma,t} \quad (5.7)$$

$$\vec{f}_{\sigma,n} = \sigma K \vec{n} \text{ and } \vec{f}_{\sigma,t} = \frac{\partial \sigma}{\partial t} \vec{t} \quad (5.8)$$

Where  $\sigma$  is the surface tension coefficient,  $\vec{n}$  is the unit vector normal to the free surface and directed from the liquid to gas,  $\vec{t}$  is the unit vector in the tangential direction to the free surface, and  $K$  is the mean curvature of the free surface. For a constant surface tension coefficient  $\sigma$ , the tangential force is zero and the surface tension results in a force normal to the interface ( $\vec{f}_\sigma = \vec{f}_{\sigma,n}$ ). When the surface tension coefficient varies along the surface, which can be caused by temperature differences, the tangential part does not vanish. In this case, Marangoni or Bernard convection can develop tangential to the free surface.

In the VOF multiphase model case, the surface tension force is calculated according to the CSF model. That is, it uses the smooth field of the phase volume fraction  $\alpha_i$  to calculate a vector normal to the interface:

$$\vec{n} = \vec{\nabla} \alpha_i \quad (5.9)$$

The curvature of the interface can be therefore expressed in term of the divergence of the unit normal vector  $\vec{n}$ , as follows:

$$K = -\vec{\nabla} \cdot \frac{\vec{\nabla} \alpha_i}{|\vec{\nabla} \alpha_i|} \quad (5.10)$$

Now the normal component of the surface tension force  $\vec{f}_{\sigma,n}$  can be expressed as:

$$\overrightarrow{f_{\sigma,n}} = -\sigma \vec{\nabla} \cdot \frac{\vec{\nabla} \alpha_i}{|\vec{\nabla} \alpha_i|} \vec{\nabla} \alpha_i \quad (5.11)$$

In the case of a variable tension coefficient, the tangential force is evaluated as:

$$\overrightarrow{f_{\sigma,t}} = (\vec{\nabla} \sigma)_t |\vec{\nabla} \alpha_i| \quad (5.12)$$

Where  $(\vec{\nabla} \sigma)_t$  is the gradient of the surface tension coefficient in the tangential direction.

As the present study treats also melt-solidification, it is important to provide a model for solidification in the simulation. To do so, the simulation setting includes the Melting-Solidification model implemented in Star CCM+ software. This model does not track the liquid-solid interface explicitly. Instead, it uses an enthalpy formulation to determine the distribution of the solidified portion of the liquid-solid phase.

For basic melting-solidification, the enthalpy of the liquid-solid  $h_{ls}^*$  includes the latent heat of fusion  $h_{fusion}$ :

$$h_{ls}^* = h_{ls} + (1 - \alpha_s^*) h_{fusion} \quad (5.13)$$

Where  $h_{ls}$  is the sensible enthalpy,  $\alpha_s^*$  the relative solid volume fraction defined as the portion of the volume of liquid-solid which is in the solid state. In the enthalpy model, the relative solid volume fraction  $\alpha_s^*$  is a function of temperature:

$$\alpha_s^* = \begin{cases} 1 & \text{if } T^* < 0 \\ f(T^*) & \text{if } 0 < T^* < 1 \\ 0 & \text{if } 1 < T^* \end{cases} \quad (5.14)$$

Where  $T^*$  is the normalized temperature that is defined as:

$$T^* = \frac{T - T_{solidus}}{T_{liquid} - T_{solidus}} \quad (5.15)$$

The function  $f(T^*)$  is called the fraction solid curve. For a linear dependence  $\alpha_s^*$  and  $T^*$ , the solidification path is defined as:

$$f(T^*) = 1 - T^* \quad (5.16)$$

If melting and solidification take place at one temperature, as it is the case with pure metal such as Tin and Copper, a linear solidification path is assumed and a small temperature interval of 0.002 K is automatically introduced. Moreover, the physical properties for the molten metal were devised as field functions build according of the fitting equations found in Assael et al. (2010) and summarized in Table 5.4a and 5.4b.

Table 5.4a Physical Properties Simulation Set-up for Copper (Cu)

<b>Physical Properties</b>	<b>Star CCM+ User Field Function</b>
<b>Dynamic Viscosity</b>	$\mu = 0.004 \text{ Pa} \cdot \text{s}$
<b>Specific Heat</b>	$c_p = 400 \text{ J/kgK}$ .
<b>Density</b>	If Temp $\leq 1373.77 \text{ K}$ then $\rho = 8960 \text{ kg/m}^3$ . Otherwise $\rho = 8020 \text{ kg/m}^3$ .
<b>Thermal Conductivity</b>	If Temp $\leq 1373.77 \text{ K}$ then $\kappa = 394 \text{ W/mK}$ . Otherwise $\kappa = 180 \text{ W/mK}$ .
<b>Contact Angle</b>	$\theta_a = 140^\circ$

Table 5.4b Physical Properties Simulation Set-up for Tin (Sn)

<b>Physical Properties</b>	<b>Star CCM+ User Field Function</b>
<b>Dynamic Viscosity</b>	$\mu = 0.002 \text{ Pa} \cdot \text{s}$
<b>Specific Heat</b>	$c_p = 209.34 \text{ J/kgK}$ .
<b>Density</b>	If Temp $\leq 505.08 \text{ K}$ then $\rho = 7265 \text{ kg/m}^3$ .

	Otherwise $\rho = 6990 \text{ kg/m}^3$ .
<b>Thermal Conductivity</b>	If Temp $\leq 505.08 \text{ K}$ then $\kappa = 70 \text{ W/mK}$ .  Otherwise $\kappa = 27 \text{ W/mK}$ .
<b>Contact Angle</b>	$\theta_a = 140^\circ$

### 3. Results and Discussion

Having elected the models, the geometry and the boundary conditions, simulations were realized for the investigated molten metal spreading phenomenon. The models selected for the current Star-CCM+ simulations are tabulated in Table 5.3. Cell number was decided to be slightly over 1 million according to a mesh sensitivity analysis. To simulate the multiphase phenomena involving molten metal, solid metal and surrounding air environment, Volume of Fluid Model (VOF) was selected, as it has shown numerous advantages in its past uses for molten core safety assessment studies (Dinh et al., 2000). Moreover, the physical properties for the molten metal were devised as field functions created according to the fitting equations found in Assael et al. work (2010) and summarized in Table 5.4a and 5.4b.

In this section, the simulation of Copper and Tin spreading, similar to Fig 5.5, using Star CCM+ and its comparison with experimental data set, such as Fig 5.4, acquired through chapter 3 will be explained. Beside the benchmark exercise, the goal is to investigate the reliability of such simulation for cases with and without finger formation. As it is a common approach, a numerical uncertainty analysis (Celik, I., 1993 and Roache et al. 1986) was performed to assure that the simulations do not suffer any numerical induced inaccuracy. The result of this analysis can be found in Table 5.5.

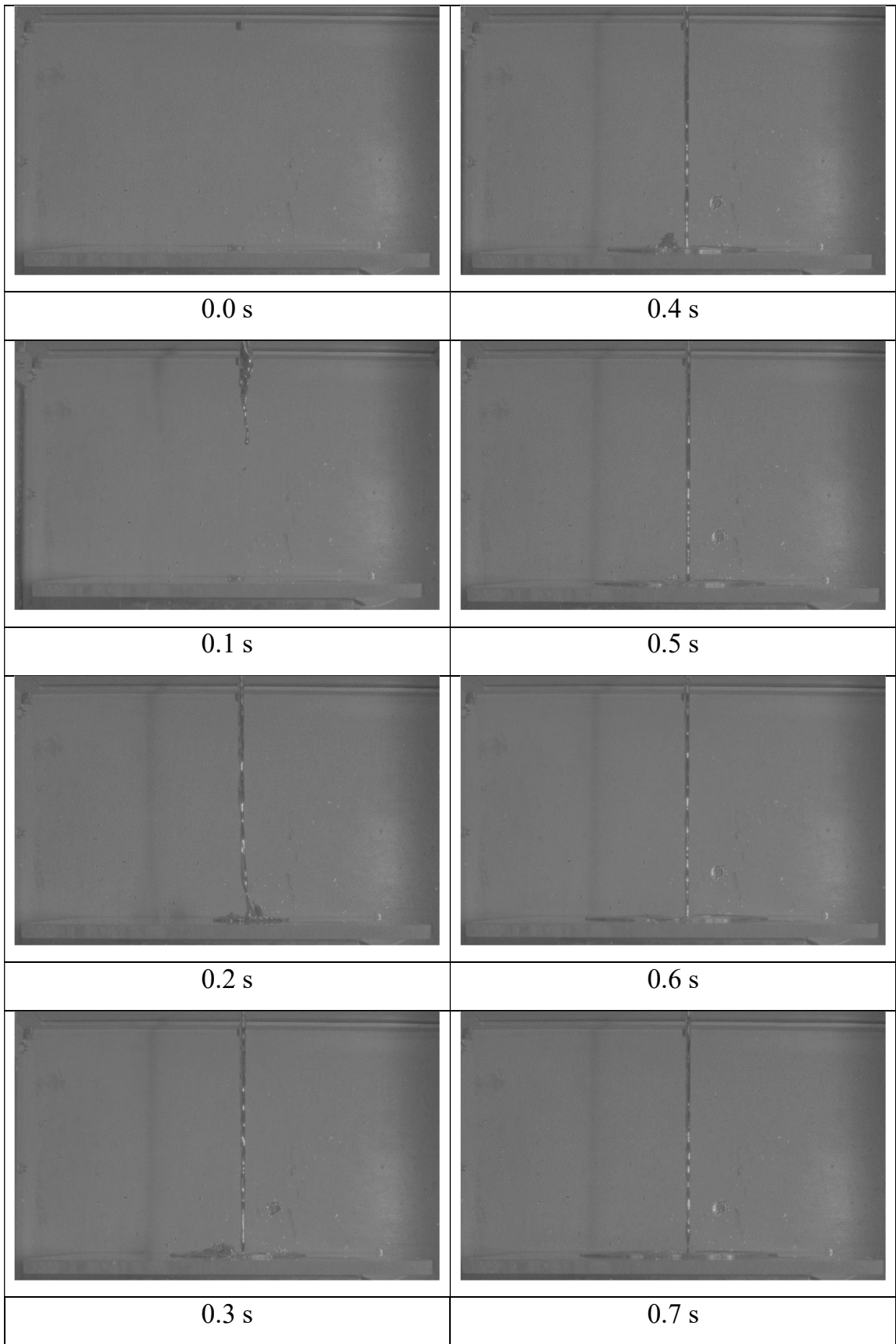


Fig. 5.4. Experimental Spreading transient



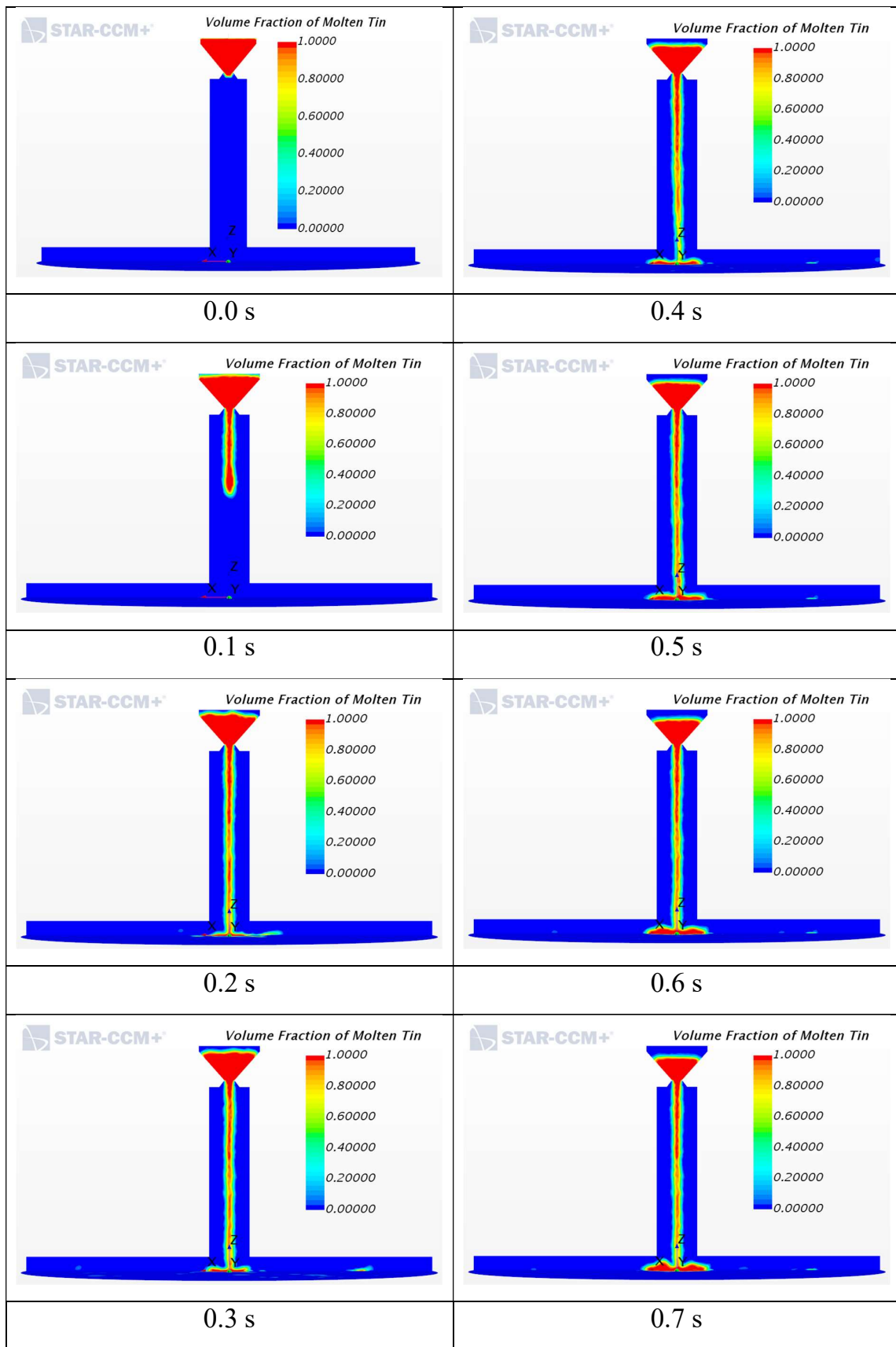


Fig. 5.5. Simulations Volume fraction results

Table 5.5 Simulation Discretization Error Calculations

	Temperature Value at z = 0.001 m	Temperature Value at z = 0.02 m
<b>N<sub>1</sub></b>	704,687	704,687
<b>N<sub>2</sub></b>	1,314,033	1,314,033
<b>N<sub>3</sub></b>	2,743,010	2,743,010
<b>r<sub>21</sub></b>	1.33	1.33
<b>r<sub>32</sub></b>	1.25	1.25
<b>φ<sub>1</sub></b>	317	1370
<b>φ<sub>2</sub></b>	318	1350
<b>φ<sub>3</sub></b>	304	1250
<b>p</b>	14.3	6.7
<b>φ<sub>ext</sub><sup>21</sup></b>	317	1380
<b>e<sub>a</sub><sup>21</sup></b>	0.00177	0.0176
<b>e<sub>ext</sub><sup>21</sup></b>	2.92*10 <sup>-5</sup>	0.00299
<b>GCI<sub>fine</sub><sup>21</sup></b>	3.65*10 <sup>-5</sup>	0.00374

As referenced in Celik et al. work (1993), the tabulated values are built for mesh sizes  $h_1$ ,  $h_2$  and  $h_3$  with  $h_1 < h_2 < h_3$ . From there, the fine-grid convergence index  $GCI_{fine}^{21}$  is calculated and permits to conclude that the simulations are free of such inaccuracy, as the lector can see with the numerical uncertainty of 0.374% at worst.

From there, the first step was to validate the simulation against the experimental data collected so far. The simulations were built to view the spreading phenomenon first. Therefore, the setting of those simulations was chosen to exclude the molten jet breakup. For tin, it was elected to set the nozzle diameter  $D_0$  equal to 10 mm and a mass of 350 g. In addition, the falling height was set to 100, 200, and 300mm as used in the experimental setting. The comparison with the experimental data can be seen in Table and Fig 5.6a.

As for copper, it was elected to set the nozzle diameter  $D_0$  equal to 8 mm and a mass of 400 g. In addition, the falling height was set to 100 and 300 mm as used in the experimental setting. The comparison with the experimental data can be seen in Table and Fig 5.6b.

Table 5.6a Comparison of Maximum Spreading and Thickness between experiments and simulations for Tin (Sn)

<b>Hf (mm)</b>	<b>Max Spreading Exp (mm)</b>	<b>Max Spreading Simulation (mm)</b>	<b>Spreading Error (%)</b>	<b>Thickness Exp (mm)</b>	<b>Thickness Simulation (mm)</b>		<b>Thickness Error (%)</b>	
<b>100</b>	164.61	160	2.8	2.37	2.67		12.66	
<b>200</b>	154.8	120	22.48	2.58	Inner Ring	Outer Ring	Inner Ring	Outer Ring
					10	2.8	287.6	8.53
<b>300</b>	162.5	134	17.54	2.37	4.26		79.75	

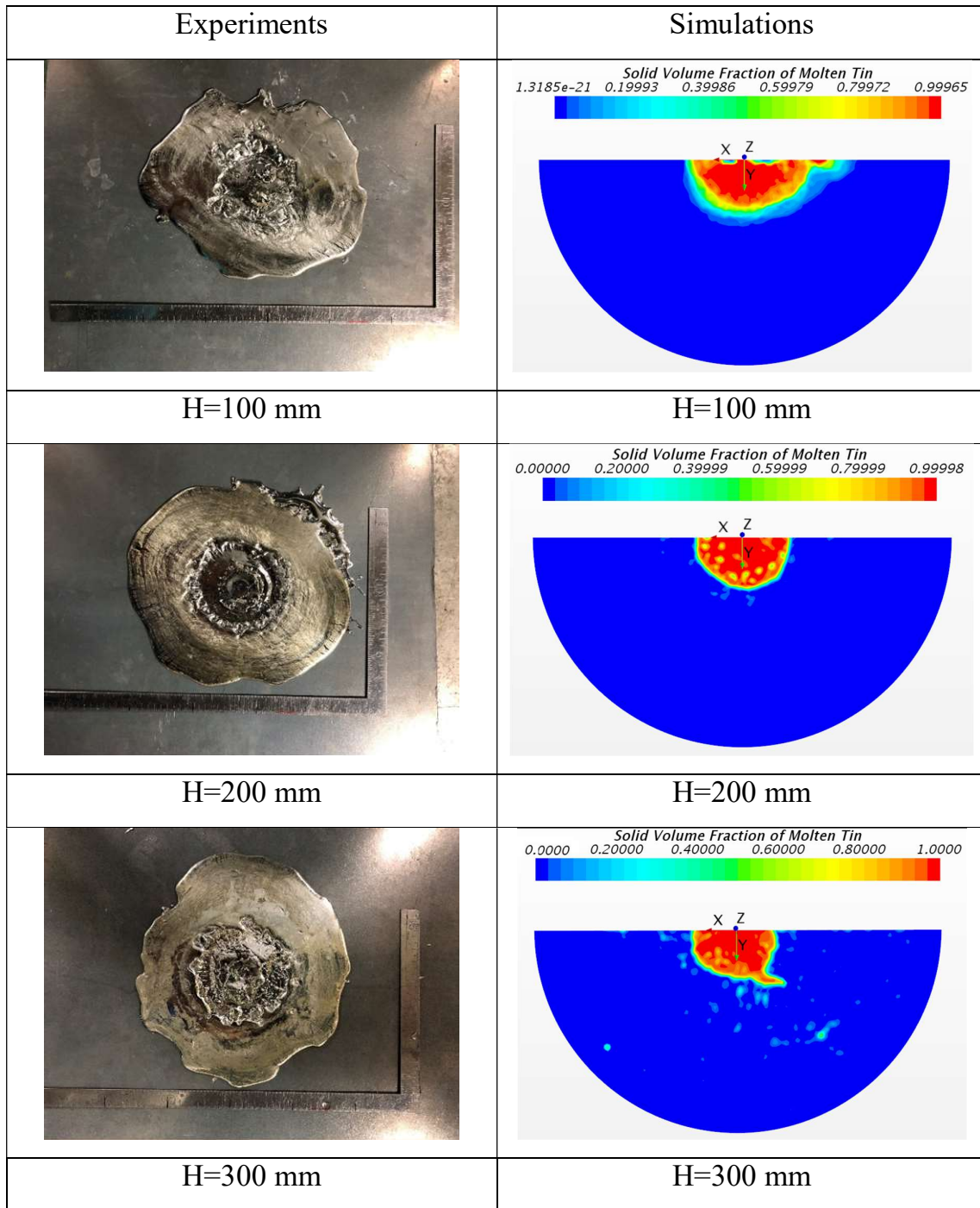


Fig 5.6a Comparison between experimental and simulation spreading for Sn

Table 5.6b Comparison of Maximum Spreading and Thickness between experiments and simulations for Copper (Cu)

<b>Hf (mm)</b>	<b>Max Spreading Exp (mm)</b>	<b>Max Spreading Simulation (mm)</b>	<b>Spreading Error (%)</b>	<b>Thickness Exp (mm)</b>	<b>Thickness Simulation (mm)</b>	<b>Thickness Error (%)</b>
<b>100</b>	145.7	103.5	28.96	4.32	4.84	12.04
<b>300</b>	143.28	110.1	23.16	5.04	5.65	12.1

The next step in this simulation investigation is to include jet-breakup in the setting. Therefore, extra simulations were devised for a nozzle diameter of 5.5 mm and a falling height of 500 mm for a mass of 350 g for tin as a first step in this direction. This set-up has proven to exhibit the jet-breakup phenomenon through the experimental data collection done in chapter 3. The preliminary results can be seen in Table 5.7.

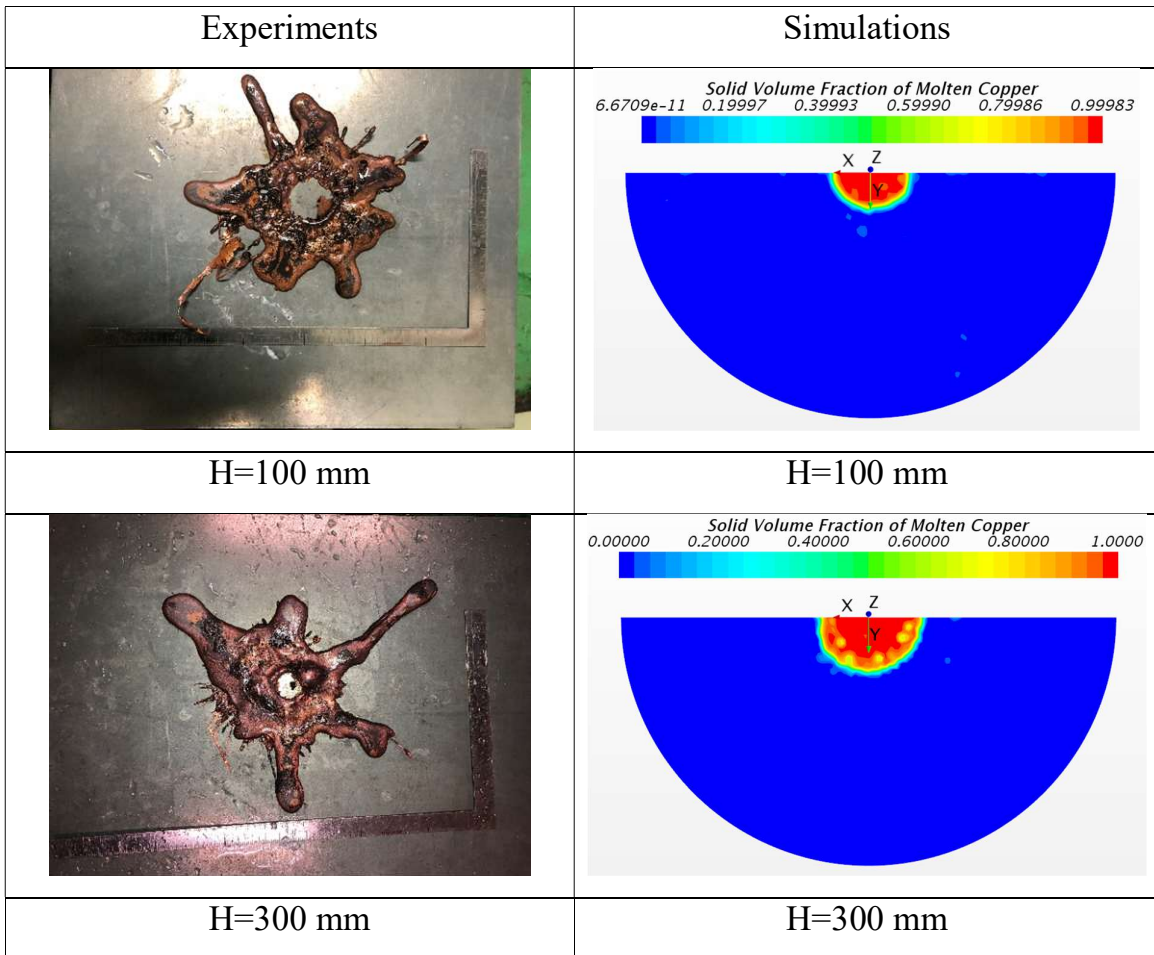


Fig 5.6b Comparison between experimental and simulation spreading for Cu

Table 5.7 Preliminary results for Jet Breakup Simulation

Molten material type	Max Spreading Exp (mm)	Max Spreading Simulation (mm)	Spreading Error (%)	Jet breakup length Exp (mm)	Jet breakup length Simulation (mm)	Jet breakup length Error (%)
Tin	Splashing predominant			374	400	6.95

In most cases, finger formation is absent from the simulations. Most of the simulations seem to exhibit splashing through the molten material jet life as shown in Fig 5.7. Moreover, the spreading maximum length seems to be under-predicted and the thickness seems to be over-predicted by the simulations for both copper and tin. As for jet-breakup, jet instability was observed and a partial breakup was observed in the transient section of the simulation (jet formation beginning and end).

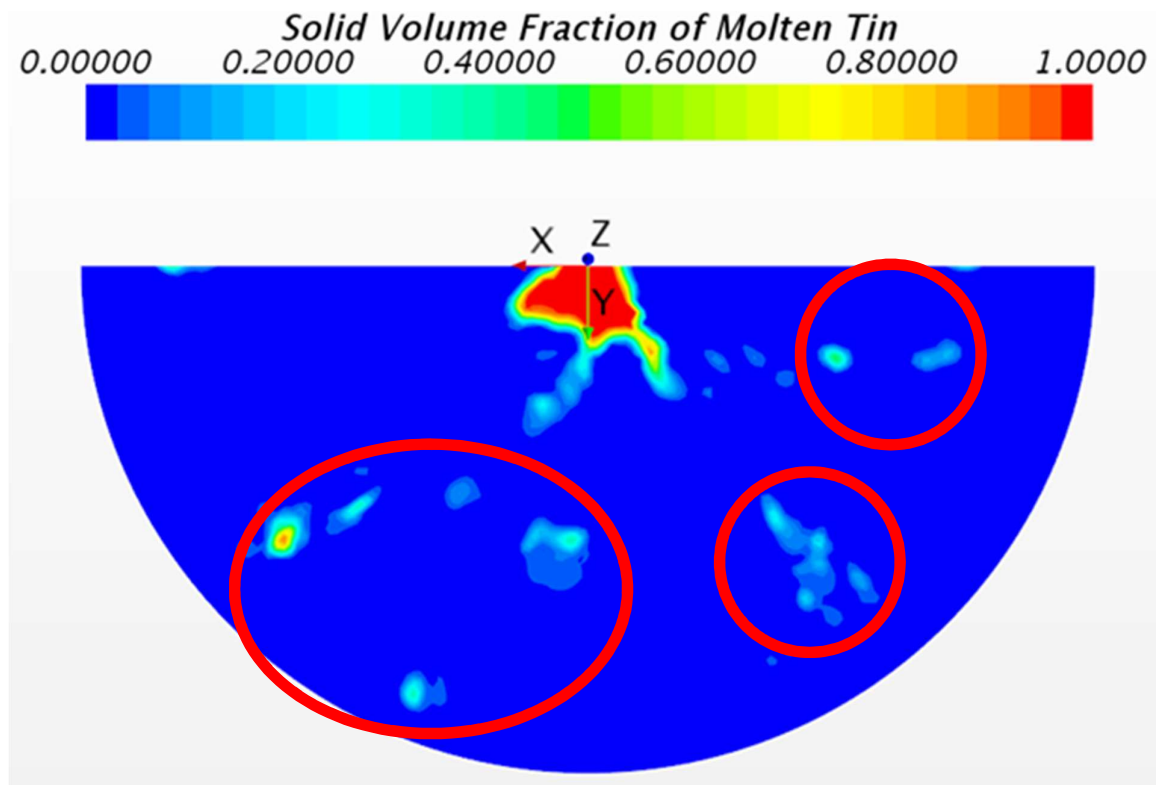


Fig 5.7. Example of splashing through simulation (circled in red).

As for the dedicated jet-breakup simulations, in the case of tin simulation, the jet-breakup occurs at a height close to the predicted value but splashing seems predominant in this configuration. A potential explanation for this behavior could be the smaller surface tension and/or the heat loss involved in this case. More precise simulations for both tin and copper to investigate this phenomenon will be the next step for this study.

In the current setting, simulations consider the spreading plate as a no-slip wall in terms of boundary conditions. Any interaction between the spread and the spreading plate is therefore seen by the models used as just a heat transfer between molten material and wall. This configuration does not take into account the roughness of the spreading surface and any thermal resistance and/or liquid-wall interaction that it could generate as it was reported in Tang et al. (2017) work.

A way to improve the prediction effectiveness of Star CCM+ for jet spreading assessment would be to include the roughness of the spreading plate in the simulation setting. As the roughness modifies primarily the heat transfer between molten material and plate, the first way to introduce this in the simulation setting will be to use a user-defined thermal resistance function or locally modified the heat transfer between spread and plate. A second way to introduce roughness in the simulation will be to modify the geometry of the spreading plate. The idea will be to change the flat geometry of the spreading plate to a saw or wave type of pattern. Such a setting was successfully used in Ahmed et al. (2002) work but will likely require a higher calculation power than the one currently available to the present study.

#### 4. Optional models and Prediction Enhancement

In the present study, even if a good agreement was reached between simulations and experiments' results, there are still ways for improvements. One of the primary improvements concerns the mesh size, time-step, and the scheme's order used. Even if they were validated by an uncertainty analysis and a convergence criterion verification, both the mesh size, the time-step, and the scheme's order were also selected to enable a certain reactivity from Star CCM+, meaning be able to get results in a reasonable amount of time (few days) with the available calculation power (2 cores). Therefore, the first way to enhance the simulations will be to refine those coefficients, meaning smaller mesh, time-step, and higher scheme's order. But, by doing so, the calculation time, for the current allocated computation power, will increase drastically.



Another way to improve the simulations will be to use additional models to involve physics neglected by simplification. Assumptions were made during the current study such as the constant value for the contact angle and the pure element type for the molten materials. A way to compensate those assumptions will be to use the corresponding optional models available in Star CCM+. According to Star CCM+ User Guide, to be able to use a dynamic contact angle, it is necessary to have access to the triple line velocity. The triple line velocity is the line where the wall and both fluid phases are in mutual contact. This quantity is related to the dimensionless Capillary Number  $Ca$  as:

$$Ca = \frac{V\mu}{\sigma} \quad (5.17)$$

Where  $V$  is the triple line velocity,  $\mu$  the dynamic viscosity of the primary phase (usually a liquid phase, here molten material phase),  $\sigma$  the surface tension coefficient.

The triple line velocity is defined as:

$$V = -\langle \vec{V} \cdot \vec{n}_t \rangle \quad (5.18)$$

Where is the relative velocity of the fluid and the corresponding wall at the triple line, the normalized wall tangent pointing in the same direction as the volume fraction gradient of the primary phase  $\nabla\alpha$ .

STAR CCM+ implements the Kistler correlation, which is an empirical dynamic contact angle correlation based on the Capillary Number  $Ca$  and utilizing the Hoffman function. The Kistler contact angle is defined as:

$$\theta_k = f_{Hoff}(Ca + f_{Hoff}^{-1}(\theta_s)) \quad (5.19)$$

Where  $\theta_s$  is the static contact angle and  $f_{Hoff}$  is the Hoffman function:

$$f_{Hoff}(x) = \cos^{-1}\left(1 - 2 \tanh\left(5.16 \left(\frac{x}{1 + 1.31x^{0.99}}\right)^{0.706}\right)\right) \quad (5.20)$$

As previously mentioned, it is assumed that the molten materials used in the simulations are pure, meaning that they are composed of one type of species, here Cu and Sn respectively. But by using that assumption, oxidation and therefore more complex flow behavior are not taken into account in the simulation. Even if the experiments used to validate those simulations are done under argon gas 's atmosphere to prevent oxidation, this seems to have its limits in the current experimental setting, especially for the high-temperature Copper's cases. Moreover, as those simulations are built for nuclear safety assessment, it is important to be able to draw them closer to the real corium spreading case where oxidation is detrimental.

A way to include those phenomena in the simulation setting could be to use the Surface Chemistry formulation, Slurry Viscosity and/or Mushy Zone Permeability models available in Star CCM+. According to the User Guide, for the Surface Chemistry formulation, the oxidation equations for the different simulant materials should be provided to enable Star CCM+ to simulate the reaction that is assumed to happen at the interface between the air and the molten material. As the simulation runs with non-pure substances or alloys, as it is the case if true corium is selected, Slurry Viscosity and /or Mushy Zone Permeability models enable to simulate the slurry formation that it is bound to happen in such configuration.

As mentioned, for impure substances, the melting and solidification can take place over a temperature range. In this case, the liquidus and solidus are not at the same temperature. In the temperature interval between them, the liquid is partly solidified, that is the solid and liquid phases exist simultaneously, like a slurry.

The presence of solidified crystals in the liquid increases the flow resistance. This increased resistance is modeled by the slurry viscosity model where the increased flow resistance results from an increase in viscosity of the phase mixture. In the early stages of

solidification of an alloy, small crystals nucleate and grow in the melt. The mixture of the two phases is called a slurry. These crystals move with the liquid without interacting with each another. The Slurry Viscosity model is applied for low values of the solid volume fraction ( $\alpha_s^* < \alpha_{cr}$ ) whereby the upper limit of applicability is given by the critical solid fraction  $\alpha_{cr}$ . In Star CCM+, for the used Metzner method, the variation in viscosity of the mixture is expressed as a function of the solid volume fraction  $\alpha_s^*$ :

$$\mu^* = \mu_l \left[ 1 - \left( \frac{\alpha^* F_\mu(\alpha_s^*)}{A_{crystal}} \right) \right]^{-2} \quad (5.21)$$

Where  $\mu^*$  is the effective viscosity of the mixture,  $\mu_l$  is the dynamic viscosity of the liquid,  $A_{crystal}$  is a crystal constant which depends on the aspect ratio and surface roughness of the crystal.  $F_\mu$  is a switching function for Metzner Slurry Viscosity and Carman-Kozeny Mushy Zone Permeability model.

The Carman-Kozeny permeability model provides a mushy zone for flow resistance, eliminating the need to set up porous media. In addition, the Carman-Kozeny Mushy Permeability method updates the velocity field in the melting and solidification process. For high solid volume fractions, equi-axed grains grow and start to agglomerate and to form dendritic regions.

Dendrites also grow from cooled solid surfaces or the solidification front into the melt. A partially solidified stationary region permeated with dendrites is called a “mushy zone”. A common engineering application for this model is high-pressure die casting where melt is pressed through ducts with wall temperatures below solidus temperature at high velocities. The melt solidifies at the walls and dendrites grow from the solidification front into the melt.

This partially solidified region causes an additional pressure loss in the duct that influences the melt mass flow. This pressure loss can be simulated using the Carman-Kozeny Mushy Permeability method. The resistance (active only in cells with a solid volume fraction

greater than zero) is applied to all regions to which the respective physics continuum is assigned.

The flow resistance in a mushy zone can be modeled similar to an isotropic porous medium. Therefore, to quantify the permeability, the Carman-Kozeny equation for flow through a porous medium is used:

$$K = \frac{(1 - \alpha_s^*)^3}{\alpha_s^{*2} F_K c_s} \quad (5.22)$$

In this expression,  $K$  is the permeability and  $\alpha_s^*$  is the non-dimensional solid volume fraction  $c_s = \frac{c}{d^2}$  where  $c$  is a shape constant, with a default value of 180, that is divided by the secondary dendrite arm spacing  $d$  and a non-dimensional switching function  $F_K$ .

The Metzner slurry viscosity model and the Carman-Kozeny mushy zone permeability model are typically used in combination. Both models cover different ranges of solidification state. The applicability of each model depends on the extent to which the liquid has solidified. The state of solidification is expressed by the solid volume fraction  $\alpha_s^*$ . The critical solid fraction  $\alpha_{cr}$  separates the applicability ranges of the two models as shown in Table 5.8.

$\alpha_s^* \leq \alpha_{cr}$	Metzner Slurry Viscosity Model
$\alpha_s^* > \alpha_{cr}$	Carman-Kozeny Mushy Zone Permeability Model

Table 5.8. Models Applicability Ranges

The switching function for the slurry viscosity model is:

$$F_\mu(\alpha_s^*) = 0.5 - \frac{\tan^{-1}[s(\alpha_s^* - \alpha_{cr}^*)]}{\pi} \quad (5.23)$$

Where  $s$  is a switching function constant.

The switching function for the mushy zone permeability model is the inverse of Eq (5.23):

$$F_K(\alpha_s^*) = 1 - F_\mu(\alpha_s^*) = 0.5 + \frac{\tan^{-1}[s(\alpha_s^* - \alpha_{cr}^*)]}{\pi} \quad (24)$$

However, by implementing all those model, the simulation physical precision will increase but it will be at the expend of computation speed.

Therefore, it can be concluding that the setting used in the current study could be more useful for emergency safety assessment during a severe accident. The above-mentioned optional models could be implemented either for decommissioning purposes in the case of a damaged NPP or safety assessment in the case of either safety improvement for older generation NPP and/or safety design's testing such as spreading in a core catcher.

## Conclusions and Future Directions

On one hand, through the collaboration project with TEPCO, simulations were built to understand the thermal behavior of the reactor building through the Fukushima Daichi's severe accident. The conclusion that can be drawn, under the 400 C limit, most of the potential highly contaminated area will be located in the lower section of the PCV and the depth of this contamination is roughly 25 cm. This information will be valuable for the decommissioning of Fukushima. Through this achievement, we were able to contribute to the decommissioning effort of the Fukushima Daiichi Nuclear Power Plant.

On the other hand, the purpose of the present study was to improve the decommissioning of damaged NPP, such as Fukushima Daichi, and Nuclear Safety Assessment. From there, the focus of this study was narrowed down to investigate the debris field formation and its geometry. To realize that objective, the present work was divided into two parts. First, through experiments, the investigation was focused on providing formulations that will help predict with higher accuracy the debris field geometry, especially its maximum spreading length. Second, through simulations, the investigation attempted to provide insights on the key parameters for debris field formation simulations.

Thus, experiments were carried out using molten copper and tin, as simulants for corium, to investigate the link between the instability of the gravity-driven molten metal jet and the impinging followed by its spreading over a flat area. From the collected data, formulations for the maximum spreading ratio and fingers number  $N$  were built which allow for predictions with a 20% error margin at worst. Moreover, those formulations allow us to take into account the impact of the jet's breakup, its geometry, the initial drop mass, and the spreading plate's surface roughness on the spreading pattern. It was also concluded that, if used for Safety Assessment, the improved formulations for  $\xi_{max}$  and  $N$  will allow predicting the debris field's formation with more accuracy. That achievement allows us to provide ways to refine the debris field's geometry for simulation's purposes and therefore improve the Nuclear Safety Assessment of a LOCA and its Decommissioning.

As for the simulation part, it was also found that the simulation under-estimated the maximum spreading length and over-estimated the spread thickness for a fixed value of Nozzle diameter. Another point that can be noted for the copper simulation is that, for the selected setup, finger formation is not apparent in the simulation even if this phenomenon is registered in the experiment. For these observations, it was possible to conclude that the experiment/simulation difference could be generated by the absence of a spreading plate's surface roughness in the simulation setting. That assessment allows us to underline the importance of the spreading plate's surface roughness as a key parameter for molten metal spreading simulation. Through that, the knowledge on the key parameters useful for debris field formation simulation was deepened. It also allows us to refine the boundary/initial conditions used for Safety Assessment and Decommissioning's simulations.

Therefore, a way to improve the prediction effectiveness of Star CCM+ for jet spreading assessment will be to include the roughness of the spreading plate in the simulation setting. As the roughness modifies primarily the heat transfer between molten material and plate, a way to introduce this in the simulation setting will be to use a user-defined thermal resistance function or locally modified the heat transfer between spread and plate.

A second way to introduce roughness in the simulation will be to modify the geometry of the spreading plate. The idea will be to change the flat geometry of the spreading plate to a saw or wave type of pattern.

Therefore, the next direction in which this topic should be to investigate the impact of the spreading plate's roughness on the molten material's spreading pattern more thoroughly in both experiments and simulations.

## References

- [1] Abe et al. 2004, Study on thermal hydraulic behavior during molten material and coolant interaction. Nucl. Eng. Des.230, 277–291.
- [2] Abe et al., 2005, Study on the quench behavior of molten fuel material jetted into coolant. Transactions of the Japan Society of Mechanical Engineers, Series B 71, 947–953 (in Japanese).
- [3] Abe et al., 2006, Fragmentation behavior during molten material and coolant interactions. Nucl. Eng., Des. 236, 1668–1681.
- [4] Allelein et al., 1999, Simulation of core melt spreading with LAVA: theoretical background and status of validation, OECD Workshop on Ex-Vessel Debris Coolability, Karlsruhe, Germany, 15–18
- [5] Alsmeyer et al., 1996, “Overview on the Results of the RCA Project on Molten Core – Concrete Interactions”, FISA-95 Proceedings, Luxemburg EUR 16896 EN, pp.231-255.
- [6] American National Standards Institute, “American National Standard for Decay Heat Power in Light Water Reactors “, ANSI/ANS 5.1, August 1979.
- [7] A.M.Ahmed, R.H.Rangel, “Metal droplet deposition on non-flat surfaces: effect of substrate morphology”, International Journal of Heat and Mass Transfer, Volume 45, Issue 5, February 2002, Pages 1077-1091
- [8] M. Andreeva, M.P. Pavlova, P.P. Groudev, Overview of plant-specific severe accident management strategies for Kozloduy nuclear power plant, WWER-1000/320,2007, Annals of Nuclear Energy
- [9] Assael et al, Marc J. Assael, Agni E. Kalyva, Konstantinos D. Antoniadis, R. Michael Banish, Ivan Egry, Jiangtao Wu, Erhard Kaschnitz, and William A. Wakeham, Reference Data for the Density and Viscosity of Liquid Copper and Liquid Tin, 2010, Journal of Physical and Chemical Reference Data 39, 033105



- [10] Aziz et al., 2000, Impact, recoil and splashing of molten metal droplets, International Journal of Heat and Mass Transfer, Volume 43, Issue 16, Pages 2841-2857
- [11] Bang et al., 2003, Experimental study of melt jet breakup in water. J. Nucl. Sci. Technol. 40, 807–813.
- [12] Bang et al., 2017, Experiment and Modeling of Jet Breakup in Fuel-coolant Interactions. In: Proceedings of the 8th European Review Meeting on Severe Accident Research (ERMSAR-2017), pp. 1–14 Warsaw, Poland.
- [13] Bholra, R., Chandra, S. Parameters controlling solidification of molten wax droplets falling on a solid surface, Journal of Materials Science (JMS), 1999 October, vol 34, p 4883–4894.
- [14] G. Breit et al., Phys. Rev. 49, p. 519, 1936.
- [15] Bürger et al., 1985, Effect of Solid Crust on the Hydrodynamic Fragmentation of Melt Droplets. Institut für Kernenergetik und Energiesysteme der Universität Stuttgart Report No. IKE 2 TF-74.
- [16] Bürger et al., 1986, Effect of Solid Crusts on the Hydrodynamic Fragmentation of Melt Drops. Science and Technology of Fast Reactor Safety. BNES, London, pp. 503–508.
- [17] Brackbill, J. U., Kothe, D. B., and Zemach, C. 1992. A Continuum method for modeling surface tension, J. Comp. Physics, 100, pp. 335-354.
- [18] Cao et al., 2002, A thermal fragmentation model induced by surface solidification. J. Nucl. Sci. Technol. 39, 628–636.
- [19] Celik, I., 1993, “Numerical Uncertainty in Fluid Flow Calculations: Needs for Future Research,” ASME JOURNAL OF FLUIDS ENGINEERING, 115, pp. 194-195.
- [20] Cherdron et al., 2005, ECO Steam Explosion Experiments documentation and Evaluation of Experimental Data. FZKA-7011.

- [21] Cho et al., 1991, Experimental investigations with respect to the modelling of fragmentation in parallel shear flows of liquids. In: Proceedings of the Sprays and Aerosols Conference, pp. 165–169 Guildford, UK.
- [22] Cho et al., 1997, Experiments on interactions between zirconium-containing melt and water (ZREX): hydrogen generation and chemical augmentation of energetics. In: Proceedings of the OECD/CNSI Specialists Meeting on Fuel-coolant Interactions 2. pp. 595–608 Tokai-mura, Japan.
- [23] Cho et al., 1998, Experiments on Interactions between Zirconium-containing Melt and Water. NUREG/CR-5372.
- [24] Chu et al., 1995, Ex-vessel melt coolant interactions in deep water pool: studies and accident management for Swedish BWRs. Nucl. Eng. Des. 155, 159–213.
- [25] Chudanov et al., 1994. Model of spreading on the concrete substrate during severe accidents at nuclear plants, in: ARS'94, Pittsburgh, PA.
- [26] Cagnet et al., 1994, “VULCANO: A Large Scale UO<sub>2</sub> Program to Study Corium Behavior and Cooling for Future Reactors,” OECD/CNSI/NEA Workshop on Large Molten Pool Heat Transfer, pp. 521-529.
- [27] Cagnet et al., 1997, “Main Results of the COMAS5a Benchmark (CROCO, THEMA, MELTSPREAD, LAVA, CORFLOW, MECO Codes)”, Presented to CSC Project Meeting, Cadarache.
- [28] Cagnet et al., 2001, Corium Spreading and Coolability (CSC Project), Nucl. Eng. Des., 209 (2001), pp. 127-138
- [29] Corradini et al., 1981, Phenomenological modeling of the triggering phase of small-scale steam explosion experiments. Nucl. Sci. Eng. 78, 154–170
- [30] Denham et al., 1994, Experiments on the mixing of molten uranium dioxide with water and initial comparison with CHYMES code calculations. Nucl. Eng. Des. 146, 97–108.
- [31] Dinh et al., 1999, Experimental and analytical studies of melt jet-coolant interactions: a synthesis. Nucl. Eng. Des. 189, 299–327.

- [32] Dinh et al., 2000, Core melt spreading on a reactor containment floor. Prog. Nucl. Energy 36, 405–468.
- [33] Dombrovsky et al., 2008, The effect of thermal radiation on the solidification dynamics of metal oxide melt droplet. Nucl. Eng. Des. 238, 1421–1429.
- [34] Ehrhard et al., 1996, “Spreading of Melts in the Presence of Solidification,” International Conference on Nuclear Engineering (ICONE-4), Vol. 1B, pp. 935-941.
- [35] Epstein et al., 1977, Stability of a submerged frozen crust, J. Heat Tran., pp. 527-532
- [36] Epstein et al., 1985, Steam film instability and the mixing of core-melt jets and water. In: ANS Proceedings of National Heat Transfer Conference, pp. 277–284 Colorado, USA.
- [37] Epstein, Fauske et al., 2001, Applications of the turbulent entrainment assumption to immiscible gas-liquid and liquid-liquid systems. Chem. Eng. Res. Des. 79, 453–462.
- [38] Gilberto Espinosa-Paredes, Lluís Batet, Alejandro Nuñez-Carrera, and Jun Sugimoto, Severe Accident Analysis in Nuclear Power Plants, 2012, Science and Technology of Nuclear Installations
- [39] Harold Etherington et al., “Nuclear Engineering Handbook”, McGraw-Hill Book Co., 1958.
- [40] Farmer et al., 1990, The MELTSPREAD 1 code for analysis of transient spreading on containment, ANS Winter Meeting, Washington, DC.
- [41] Fauske et al., 1973, On the mechanism of uranium dioxide-sodium explosive interactions. Nucl. Sci. Eng. 51, 95–101.
- [42] Fauske, Epstein et al., 2001. Applications of the turbulent entrainment assumption to immiscible gas-liquid and liquid-liquid systems. Chem. Eng. Res. Des. 79, 453–462.
- [43] Fauske et al., 2002, Assessment of the FBR core disruptive accident (CDA): the role and application of general behavior principles (GBPs). J. Nucl. Sci. Technol. 39, 615–627.

- [44] Fieg et al., 1996, “Simulation Experiments on the Spreading Behavior of Molten Core Debris”, Proceedings of the 1996 National Heat Transfer Conference, in the session “Fundamental Phenomena in Severe Accidents”, Houston, Texas, August 3-6, HTC-Vol.9, pp.121-129.
- [45] Fink and Griffiths, 1990, “Radial Spreading of Viscous-Gravity Currents with Solidifying Crusts “, Journal of Fluid Mechanics, Vol. 221, pp. 485-509.
- [46] Foit et al., 2002, Spreading on ceramic and concrete substrates in KATS experiments, Proceedings of the Annual Meeting on Nuclear Technology, Stuttgart, pp. 211-215
- [47] Foit et al., 2004, Spreading under variable viscosity and time-dependent boundary conditions: estimate of viscosity from spreading experiments, Nucl. Eng. Des., pp. 239-253
- [48] Foit et al., 2006, Large-scale ECOKATS experiments: Spreading of oxide melt on ceramic and concrete surfaces, Nuclear Engineering and Design, Volume 236, Issue 24, Pages 2567-2573
- [49] G.-X.Wang, E.F.Matthys, 2002, Experimental determination of the interfacial heat transfer during cooling and solidification of molten metal droplets impacting on a metallic substrate: effect of roughness and superheat, International Journal of Heat and Mass Transfer, Volume 45, Issue 25, December 2002, Pages 4967-4981
- [50] Gabor et al., 1992, Molten aluminum alloy fuel fragmentation experiments. In: Proceedings of the 5th International Topical Meeting on Nuclear Reactor Thermal Hydraulics (NURETH-5), pp. 1–16 Salt Lake City, Utah, USA.
- [51] Gabor et al., 1994, Molten aluminum alloy fuel fragmentation experiments. Nucl. Eng. Des. 146, 195–206. Hall, R.W., Fletcher, D.F., 1995. Validation of CHYMES: simulant studies. Nucl. Eng. Des.155, 97–114.
- [52] Samuel Glasstone et al., “Nuclear Reactor Engineering “, D.Van Nostrand and Company, 1967.
- [53] Grant R.P., Middlemen S., Newtonian jet stability. AIChE J., 1966 July, vol 2, Issue 4, p 669–678.

- [54] Greene et al., (1988), “Experimental Studies on Melt Spreading, Bubbling Heat Transfer and Coolant Layer Boiling,” Proceedings of 16th Water Reactor Safety Meeting, NUREG/CP-0096, pp.341-358.
- [55] Hall et al., 1995, Validation of CHYMES: simulant studies. Nucl. Eng. Des. 155, 97–114.
- [56] Haraldsson et al., 2000, Breakup of Jet and Drops during Premixing Phase of Fuel Coolant Interactions. PhD thesis. The Royal Institute of Technology, Sweden.
- [57] Haraldsson et al., 2001, Effect of solidification on drop fragmentation in liquid-liquid media. Heat Mass Tran. 37, 417–426.
- [58] Hohmann et al., 1995, FCI experiments in the alumina oxide/water system. Nucl. Eng. Des. 155, 391–403.
- [59] Hong et al., 2013, Status of the OECD-SERENA project for the resolution of ex-vessel. J. Energy Power Eng. 7, 423–431.
- [60] Hong et al., 2015, An investigation on size distribution and physical characteristics of debris in TROI FCI tests. Nucl. Technol. 191, 122–135.
- [61] Hong et al., 2016, Fuel-coolant interaction test results under different cavity conditions. Nucl. Technol. 196, 538–552.
- [62] Huber et al., 1996, PREMIX, Documentation of the Results of Experiments PM01 to PM06. FZKA-6370.
- [63] Huhtiniemi et al., 1997a, FCI experiments in the corium/water system. Nucl. Eng. and Des. 177, 339–349.
- [64] Huhtiniemi et al., 1997b, Results of recent KROTOS FCI tests: alumina versus corium melts. Nucl. Eng. Des. 189, 379–389.
- [65] Huhtiniemi et al., 2001, Insight into steam explosion with corium melts in KROTOS. Nucl. Eng. Des. 204, 391–400.
- [66] Huppert et al., 1982, “The Propagation of Two- Dimensional and Axisymmetric Viscous Gravity Currents, Over a Rigid Horizontal Surface”, Journal of Fluid Mechanics, Vol. 121. pp. 43-58.

- [67] Hidaka et al., 2002, Verification for flow analysis capability in the model of three dimensional natural convections with simultaneous spreading, melting and solidification for the debris coolability analysis module in the severe accident analysis code ‘SAMPSON’, (II), J. Nucl. Sci. Technol., 39, pp. 520-530
- [68] Huang T, Tian W, Zhang Y, et al. Analysis of the particulate debris bed quenching during top and bottom flood[J]. International Conference on Nuclear Engineering, Proceedings, ICONE, 2014.
- [69] Itoh et al., 2004, Internal-shear mode instabilities on high-speed liquid jet, (1) characteristics of linear solutions. J. Nucl. Sci. Technol.41, 802–808.
- [70] Iwasawa et al., 2015a, Jet breakup behavior with surface solidification. Transactions of the JSME 81, 1–15 (in Japanese).
- [71] Iwasawa et al., 2015b., Effects of surface solidification on fragmentation behavior of molten material jet. Transactions of the JSME 81, 1–20 (in Japanese).
- [72] Iwasawa and Abe,2018, Melt jet-breakup and fragmentation phenomena in nuclear reactors: A review of experimental works and solidification effects, Progress in Nuclear Energy,Volume 108, September 2018, Pages 188-203
- [73] Journeau et al., 2003, Ex-vessel corium spreading: results from the VULCANO spreading tests, Nucl. Eng. Des., 223 pp. 75-102
- [74] Journeau et al., 2006, The VULCANO VE-U7 corium spreading benchmark, Prog. Nucl. Energy, 48, pp. 215-234
- [75] Jung et al.,2016, Experimental revisit of melt jet breakup length correlations for fuel-coolant interactions. In: Proceedings of the 11thInternational Topical Meeting on Nuclear Reactor Thermal Hydraulics, Operation and Safety (NUTHOS-11), pp. 1–13 Gyeongju, Korea.
- [76] Japan Society of Mechanical Engineers (JSME), Progress in Heat Transfer New Series, vol. 1, Yokendo-publishing Co. Ltd (1995), pp. 28-34 (in Japanese)
- [77] Kaiser eta., 1997, Melt water interaction tests (PREMIX tests PM10 and PM11). In: Proceedings of the OECD/CNSI Specialists Meeting on Fuel-coolant Interactions, pp. 646–657 Tokai-mura, Japan.

- [78] Kaiser et al., 1999, PREMIX Tests PM12, PM13, and PM14 Documentation and Evaluation of Experimental Data. FZKA-6370.
- [79] Kaiser et al., 2001, PREMIX Experiments PM12-pm18 to Investigate the Mixing of a Hot Melt with Water. FZKA-6380.
- [80] Karbojian et al., 2009, A scoping study of debris bed formation in the DEFOR test facility. Nucl. Eng. Des. 239, 1653–1659.
- [81] Kazimi et al., (1989), “On the Liner Failure Potential in MARK-I Boiling Water Reactors”, Nucl.Sci. Eng., Vol.103, 59.
- [82] Kim et al., 2003, An experimental study on intermediate steam explosions experiments with molten zirconia and corium in the TROI facilities. In: Proceedings of the 10th International Conference on Nuclear Thermal Hydraulics (NURETH-10), pp. 1–6 Seoul, Korea.
- [83] Kim et al., 2004, An effect of corium composition variations on occurrence of a spontaneous steam explosion in the TROI experiments. In: Proceedings of the 6th International Topical Meeting on Nuclear Reactor Thermal Hydraulics, Operation and Safety (NUTHOS-6), pp. 1–13 Nara, Japan.
- [84] Kim et al., 2005, Triggered steam explosion experiments in the TROI facility. In: Proceedings of the 2005 International Congress on Advances in Nuclear Power Plants (ICAPP’05), pp.223–231 Seoul, Korea.
- [85] Kim et al., 2008, Steam explosion experiments using nuclear reactor materials in the TROI facilities. Heat Tran. Eng. 29, 748–756.
- [86] Kim et al., 2011, Triggered steam explosion with corium melts of various compositions in a two-dimensional interaction vessel in the TROI facility. Nucl. Technol. 176, 372–386.
- [87] Kim et al., 2016, Composition of jet breakup in fully-flooded and partially flooded reactor cavity. In: Proceedings of the 11th International Topical Meeting on Nuclear Reactor Thermal Hydraulics, Operation and Safety (NUTHOS-11), pp. 1–10 Gyeongju, Korea.

- [88] Kobayashi et al.,2014, Analytical evaluation of debris cooling and spreading behaviors at molten core in severe accident”, ICONE22-30035. In: Proceedings of the 22nd International Conference on Nuclear Engineering, Prague, Czech Republic, July 7-11.
- [89] Kondo et al.,1995, Experimental study on simulated molten jet-coolant interactions. Nucl. Eng. Des. 155, 73–84.
- [90] Kudinov et al.,2008, An experimental study on debris formation with corium simulant materials. In: Proceedings of the 2008 International Congress on Advances in Nuclear Power Plants (ICAPP’08), pp. 1–9 CA, USA.
- [91] Kudinov et al., 2010, The DEFOR-S experimental study of debris formation with corium simulant materials. Nucl. Technol. 170, 219–230.
- [92] Kudinov et al.,2013, Agglomeration and size distribution of debris in DEFOR-A experiments with Bi<sub>2</sub>O<sub>3</sub>-WO<sub>3</sub> corium simulant melt. Nucl. Eng. Des. 263, 284–295.
- [93] Kudinov et al.,2015, Experimental investigation of debris bed agglomeration and particle size distribution using WO<sub>3</sub>-ZrO<sub>2</sub> melt. In: Proceedings of the 16th International Topical Meeting on Nuclear Reactor Thermal Hydraulics (NURETH-16), pp. 1–9 Chicago, IL, USA.
- [94] Li et al., 1998, Fragmentation behavior of melt drop in coolant; effect of melt solidification. In: Proceedings of the 3rd International Conference on Multiphase Flows (ICMF3), (Lyon, France).
- [95] L. Li, M. Wang, W. Tian, G. Su, S. Qiu, Severe accident analysis for a typical PWR using the MELCOR code, 2013, Progress in Nuclear Energy
- [96] Li et al.,2017, Experimental studies on breakup and fragmentation behavior of molten tin and coolant interaction. Science and Technology of Nuclear Installations 2017, 1–14.
- [97] Lian Chen, Kun Han, Tao Li Daogui Tian, Ying Chen, Huajian Chang, Xinchun Xu, Jie Pei, Jinlong Zhang, Tao Zhang “Three-dimensional experiment of heat transfer for molten oxidic pool” Progress in Nuclear Energy, Volume 103, (March 2018)



- [98] Lu et al., 2016, Visual investigation on the breakup of high superheated molten metal during FCI process. *Appl. Therm. Eng.* 98, 962–975.
- [99] W.Lyon et al.,” WREM: Water Reactor Evaluation Model, Revision 1”, Nuclear Regulatory, Commission, May 1975.
- [100] Ma et al., 2016, In-Vessel Melt Retention of Pressurized Water Reactors: Historical Review and Future Research Needs, *Engineering*, Volume 2, Issue 1, Pages 103-111
- [101] Magallon et al.,1995, High pressure corium melt quenching tests in FARO. *Nucl. Eng. Des.* 155, 253–270.
- [102] Magallon et al., 1997, “FARO Spreading Test LS-26”, CSC Project Internal Communication
- [103] Magallon et al., 1999, Lessons learnt from FARO/TERMOS corium melt quenching experiments. *Nucl, Eng. Des.* 189, 223–238.
- [104] Magallon et al., 2001, Corium melt quenching tests at low pressure and subcooled water in FARO. *Nucl. Eng. Des.* 204, 369–376.
- [105] Manickam et al., 2014, Simultaneous visual acquisition of melt jet breakup in water by high speed videography and Radiography. In: *Proceedings of the 10th International Topical Meeting on Nuclear Reactor Thermal Hydraulics, Operation and Safety (NUTHOS-10)*, pp. 1–13 Okinawa, Japan.
- [106] Manickam et al., 2016, On the influence of water subcooling and melt jet parameters on debris formation. *Nucl. Eng. Des.* 309,265–276.
- [107] Manickam et al.,2017, On the fragmentation characteristics of melt jets quenched in water. *Int. J. Multiphase. Flow* 91, 262–275.
- [108] Matsumoto et al.,2017, Scaling analysis of the spreading and deposition behaviors of molten-core-simulated metals. *Ann. Nucl. Energy* 108, pp.79–88.
- [109] Mathai et al., 2015, Investigation of fragmentation phenomena and debris bed formation during core meltdown accident in SFR using simulated experiments. *Nucl. Eng. Des.* 292, 87–97.

- [110] Matsuba et al., 2013, Fundamental experiment on the distance for fragmentation of molten core material during core disruptive accidents in sodium-cooled fast reactors. Nuclear Safety and Simulation 4, Progress in Nuclear Energy 108 (2018) 188–203.
- [111] T. Matsumoto, K. Sakurada, S. Miwa, H. Sakashita, and M. Mori “Scaling Analysis of the Spreading and Deposition Behaviors of Molten-Core-Simulated Metals” Annals of Nuclear Energy (2017) Vol. 108, pp. 79-88
- [112] Matsuo et al., 2008, Study on jet breakup behavior at core disruptive accident for fast breeder reactor. Nucl. Eng. Des. 238, 1996–2004.
- [113] Mitchell et al., 1981, Intermediate Scale Steam Explosion Phenomena: Experiments and Analysis. NUREG/CR-2145, SAND81-0124.
- [114] Mitsuda, Hikaru; Sahboun, Nassim; Miwa, Shuichiro; Mori, Michitsugu; Kikuchi, Ryo; Miyoshi, Katsumasa, Evaluation of the in-vessel heat transfer for the debris removal of the Fukushima Daiichi nuclear power plant, Progress in Nuclear Energy, Vol. 119 (2020), pp. 103185
- [115] S. MIWA, Y. Yamamoto and G. Chiba, “Research Activities on Nuclear Reactor Physics and Thermal-hydraulics in Japan after Fukushima Daiichi Accident” Journal of Nuclear Science and Technology (2018) Vol. 55, 575-598. DOI: 10.1080/00223131.2017.1417177
- [116] Moody et al., 1989, “First Order Analyses of Molten Corium Heat Transfer”, ANS Proceedings of 1989, National Heat Transfer Conference, Philadelphia, pp.217-224.
- [117] Moriyama et al., 2005, Coarse break-up of a stream of oxide and steel melt in a water pool. JAERI-Research 2005–2017.
- [118] Morris et al., Dec. 1997, “Report on FAR0 Spreading Test L-26”, EU JRC, Ispra, presented to FAR0 Experts Group and CSC Project Meetings.
- [119] Murayama, "Estimating the destruction of pressure vessel (RPV) based on Unit 1 accident scenario," Tohoku University Fluid Science Institute, 2015.

- [120] Na et al., 2014, Pre-mixing visualization in fuel/coolant interaction without a free fall of the corium melt. In: Proceedings of the 9th Japan-Korea Symposium on Nuclear Thermal Hydraulics and Safety (NTHAS9), (Buyeo, Korea).
- [121] Na et al., 2016, Fuel-coolant interaction visualization test for in-vessel corium retention external reactor vessel cooling (IVR-ERVC) condition. Nucl. Eng. Technol. 48, 1–8.
- [122] K. NISHIHARA and H. Iwamoto, K. Suyama, “Estimation of Fuel Compositions in Fukushima-Daiichi Nuclear Power Plant”, JAEA-Data/Code, (2012)
- [123] Nishimura et al., 2002, Thermal fragmentation of a molten metal jet dropped into a sodium pool at interface temperatures below its freezing point. J. Nucl. Sci. Technol. 39, 752–758.
- [124] Nishimura et al., 2005, Thermal interaction between molten metal jet and sodium pool: effect of principal factors governing fragmentation of the jet. Nucl. Technol. 149, 189–199.
- [125] Nishimura et al., 2010, Fragmentation mechanism of a single molten copper jet penetrating a sodium pool -transition from thermal to hydrodynamic fragmentation in instantaneous contact interface temperatures below its freezing point-. J. Nucl. Sci. Technol. 47, 219–228.
- [126] No and Ishii, 1991, “Scaling Studies on Spreading of Molten Corium in Mark-1 Boiling Water Reactors”, ANS Meeting.
- [127] Ogura et al., 2018, Experimental study on molten metal spreading and deposition behaviors on wet surface, Progress in Nuclear Energy Volume 106, Pages 72-78
- [128] Ogura et al., 2018, Experimental Study on Molten Metal Spreading and Deposition Behaviors. Annals of Nuclear Energy, 118, 353-362.
- [129] Park et al., 2001, Stem explosion experiments in the “Test for Real Corium Interaction with water (TROI). In: Transactions of the International Conference on Structural Mechanics in Reactor Technology, pp. 1–8 Washington DC, USA.

- [130] Park et al., 2008, An investigation of the particle size responses for various fuel-coolant interactions in the TROI experiments. Nucl. Technol. 161, 45–56.
- [131] Park et al., 2013, Thermal-hydraulic aspects of FCI in TROI corium/water interaction tests. Nucl. Eng. Des. 263, 419–430.
- [132] Pillai et al., 2016, Experimental simulation of fragmentation and stratification of core debris on the core catcher of a fast breeder reactor. Nucl. Eng. Des. 301, 39–48.
- [133] Pilch et al., 1987, Use of breakup time data and velocity history data to predict the maximum size of stable fragments for acceleration-induced breakup of a liquid drop, Int. J. Multiphas. Flow, pp. 741-757
- [134] Poirier D. R., Poirier E. J., Heat Transfer Fundamentals for Metal Casting, 2nd ed., Minerals, Metals and Materials Society, Warrendale, 1994, PA, pp. 41–42.
- [135] Rajeev Dhiman, Sanjeev Chandra, 2005, Freezing-induced splashing during impact of molten metal droplets with high Weber numbers, International Journal of Heat and Mass Transfer, Volume 48, Issues 25–26, December 2005, Pages 5625-5638
- [136] V.H.Ransom et al., “RELAPS5/MODI Code Manual Volume 1: System Models and Numerical Methods”, EGG-2070, November 1980.
- [137] Roache, P. J., Ghia, K. N., and White, F. M., 1986, “Editorial Policy Statement on the Control of Numerical Accuracy,” ASME JOURNAL OF FLUIDS ENGINEERING, 108, p.
- [138] Saeid Shakeri, Sanjeev Chandra, 2002, Splashing of molten tin droplets on a rough steel surface, International Journal of Heat and Mass Transfer, Volume 45, Issue 23, November 2002, Pages 4561-4575
- [139] Sahboun N., Miwa S., Sawa K., DEVELOPMENT AND INVESTIGATION OF THERMAL-HYDRAULIC BEHAVIOR OF NEW REACTOR SAFETY FEATURES: INVESTIGATION ON MOLTEN METAL 3D SIMULATION, Paper Presented at: ICONE-27, 2019 May 19-24, Tsukuba, Japan.
- [140] Nassim Sahboun, Shuichiro Miwa, Kazuhiro Sawa, Yasunori Yamamoto, Yuta Watanabe, and Tomomasa Ito, Molten metal jet impingement on a flat spreading

surface, 2020, Journal Nuclear Science and Technology.

<https://doi.org/10.1080/00223131.2020.1764406>

- [141] Sallam K.A., Dai Z., Faeth G.M., Liquid breakup at the surface of turbulent round liquid jets in still gases., *Int. J. Multiphase Flow*, 2002 March, vol 28, p 427–449.
- [142] Saito et al., 1988, Experimental study on penetration behaviors of water jet into Freon-11 and liquid nitrogen ANL Proceedings: National Heat Transfer Conference ,173-183
- [143] Schins et al., 1986, Boiling and fragmentation behavior during fuel-sodium interactions, *Nucl. Eng. Des.*, pp. 221-235
- [144] Sehgal et al., 1997, “Experimental Investigation of Melt Spreading in One-Dimensional Channel”, RIT/NPS Research Report for European Union EU-CSC-IDI-97, 86~.
- [145] Sehgal et al., 2006, Stabilization and termination of severe accidents in LWRs, *Nuclear Engineering and Design*, Volume 236, Issues 19–21, Pages 1941-1952
- [146] Sehgal B.R, *Nuclear Safety in Light Water, Reactor Severe Accident Phenomenology*, Academic Press Inc, 2012, Chapter 4, Late Containment failure, p 307-424
- [147] Sehgal et al. 2016, Severe accident progression in the BWR lower plenum and the modes of vessel failure, *Annals of Nuclear Energy*, Volume 93, Pages 28-34
- [148] Spindler and Veteau, 2006a, the simulation of melt spreading with THEMA code. Part 1. Model, assessment strategy and assessment against analytical and numerical solutions, *Nucl. Eng. Des.*, 236, pp. 415-424
- [149] Spindler and Veteau, 2006b, the simulation of melt spreading with THEMA code. Part 2. Assessment against spreading experiments, *Nucl. Eng. Des.*, 236, pp. 425-441
- [150] Steinwarz et al., 1997, “Investigation on the Phenomenology of Ex-Vessel Core Melt Behavior”, Presented to Joint INV/EXV Clusters Meeting, Roma.

- [151] Steinwarz et al., 2001, Investigations on the phenomenology of ex-vessel core melt behavior (COMAS), Nuclear Engineering and Design, Volume 209, Issues 1–3, Pages 139-146
- [152] Su, G., Sugiyama, K.-I., Aoki, H., Kimura, I., Experimental study on coolability of particulate core-metal debris bed with oxidization, (II) fragmentation and enhanced heat transfer in zircaloy debris bed, Journal of Nuclear Science and Technology, 2006, 43(5): 537-545.
- [153] Sugiyama et al., 1999, Thermal interaction in crusted melts jets with large-scale structures, Nucl. Eng. Des., pp. 329-336
- [154] Sugiyama et al., 2000, A breakup mechanism of high-temperature melt jets (observation in a molten tin jet) Transactions of the Japan Society of Mechanical Engineers, Series B, pp. 1507-1513, (in Japanese)
- [155] Sugiyama et al, 2002, Research on the Fundamental Process of Thermal-hydraulic Behaviors in Severe Accident -breakup and Cooling of Molten Material Jets Japan Atomic Energy Research Institute, JAERI-Tech, pp. 2002-2010
- [156] Sugiyama, K.-I., Aoki, H., Su, G., Kojima, Y., Experimental study on coolability of particulate core-metal debris bed with oxidization, (i) fragmentation and enhanced heat transfer in zircaloy-50 wt%ag debris bed, Journal of Nuclear Science and Technology, 2005, 42(12): 1081-1084.
- [157] Suzuki et al., 1993, “Fundamental Experiment and Analysis for Melt Spreading on Concrete Floor,” Proceedings of 2nd ASME/JSME Nuclear Engineering Conference, Vol. 1, pp. 403-407.
- [158] Suzuki et al, 2014, An experimental study on local fuel–coolant interactions by delivering water into a simulated molten fuel pool, Nuclear Engineering and Design, Volume 275, Pages 133-141
- [159] Takahashi et al.,2015, Fundamental study on heavy metal freezing behavior for stop of water leakage form LWE containment vessel. Prog. in Nucl. Energy 82, 184–190.

- [160] Tang C., Qin M., Weng X., Zhang X., Zhang P., Li J., Huang Z., Dynamics of droplet impact on solid surface with different roughness, *Int. J. Multiphase Flow*, 2017 November, vol 96, p 56-69
- [161] Theofanous et al., 1993, "The Probability of Liner Failure in a Mark-I Containment, Parts I-III. Part II: Melt Release and Spreading Phenomena," *Nuclear Technology*, Vol. 101, pp. 299-384.
- [162] Tobita et al., 2016, Development of the evaluation methodology for the material relocation behavior in the core disruptive accident of sodium-cooled fast reactors. *J. Nucl. Sci. Technol.* 53, 698–706.
- [163] Tokyo Electric Power Company, Nuclear Emergency Response Headquarters Government · TEPCO Integrated Countermeasures Office, "Tokyo Electric Power Fukushima Daiichi Nuclear Power Station · Route for Convergence of Step 2 Step 2 Completion Report," 2011.
- [164] Tokyo Electric Power Company, "On the core state of Fukushima Daiichi Nuclear Power Plant No. 1 to 3," 2011.
- [165] TEPCO Corporation, Hiroshi Miyata, "About the accident at Fukushima Daiichi Nuclear Power Plant (Unit 1)," Nuclear Safety Group, Nuclear Safety Department, Nuclear Safety Group, 2012.
- [166] Tokyo Electric Power Company, "Estimation of the state of the core and containment vessel by MAAP code," 2013.
- [167] Tokyo Electric Power Company, Inc. "Estimation of the state of core and containment vessel of Fukushima Daiichi Nuclear Power Station No. 1 to 3 and investigations on unsolved problems Part 3 Progress Report," 2015.
- [168] The Tokyo Electric Power Company, "TEPCO Reports Latest Findings of Technical Inquiry into How Accident at Fukushima Unfolded", (2015)
- [169] The Tokyo Electric Power Company, "Fukushima Nuclear Accident Analysis Report", (2011)
- [170] Tokyo Electric Power Company, Estimation of core damage situation of TEPCO Fukushima Daiichi Nuclear Power Station Units 1 to 3, 2011.

- [171] Tokyo Electric Power Company, "Survey status related to state estimation in core/containment vessel," 2015.
- [172] TEPCO, "On the situation inside the containment vessel based on atmospheric gas measurement results - Behavior of hydrogen, xenon, krypton," 2012. [Online]. Available: <http://www.tepco.co.jp/nu/Fukushima-np/images/handouts-120723-06-j.pdf>.
- [173] TEPCO, Nuclear Damage Compensation and Decommissioning Facilitation Corporation, "Technical Strategic Plan 2015 for Decommissioning of the Fukushima Daiichi Nuclear Power Station of Tokyo Electric Power Company: Towards Amendment of the Mid-and-Long-Term Roadmap in 2015" (2015)
- [174] Tokyo Electric Power Company, Inc. "Estimation of the state of core and containment vessel of Fukushima Daiichi Nuclear Power Plant No. 1 to 3, and investigation on unresolved problem Part 4 Progress Report," 2015.
- [175] Tokyo Electric Power Company, Inc. "Fukushima Daiichi 1, 1 - 3 With regard to the temperature behavior at the time of changing the water injection amount so far," 2014.
- [176] TEPCO, "On installation of permanent monitoring instruments in the reactor containment vessel of Unit 3 of Fukushima Daiichi Nuclear Power Station," 2015.
- [177] Tokyo Electric Power Company, Inc. "Results of PCV equipment hatch survey of Fukushima Daiichi Nuclear Power Station Unit 3 (on results of survey by small camera)," 2015.
- [178] Tromm et al., 2000, Dry and wet spreading experiments with prototypic material at the FARO facility and theoretical analysis, Alsmeyer (Ed.), Proceedings of the OECD Workshop on Ex-Vessel Debris Coolability, Karlsruhe, Wissenschaftliche Berichte FZKA-6475, pp. 178-188
- [179] Tyrprekl et al., 2014, Material effect in the nuclear fuel-coolant interaction: analysis of prototypic melt fragmentation and solidification in the KROTOS facility. Nucl. Technol. 186, 527–532.
- [180] S. Untermeyer et al., USAEC Report ANL-4790, 1952.



- [181] Uršič et al.,2010, Material properties' influence in fuel-coolant interaction codes. *J. Eng. Gas Turbines Power* 132, 1–7.
- [182] Uršič et al.,2011, Improved solidification influence modelling for Eulerian fuel-coolant interaction codes. *Nucl. Eng. Des.* 241, 1206–1216.
- [183] Veteau et al., 1994, “CORINE Program,” OECD/CSNI/NEA Workshop on Large Molten Pool Heat Transfer, pp. 531-548.
- [184] Wan-SikYeon et al.,2012, CFD analysis of core melt spreading on the reactor cavity floor using ANSYS CFX code *Nuclear Engineering and Design*, Volume 249, Pages 90-96
- [185] K. Way et al., *Phys. Rev.* 70, p. 1318,1948.
- [186] Wei et al., 2016, Experimental investigation of the effect of control rod guide tubes on the breakup of a molten metal jet in the lower plenum of a boiling water reactor under isothermal conditions. *J. Visual* 19, 1–12.
- [187] Wittmaack, 1997, CORFLOW: a code for the numerical simulation of free-surface flow, *Nucl. Technol.*, 116, pp. 158-180
- [188] Akira Yamaguchi, Sunghyon Jang, Kazuki Hida, Yasunori Yamanaka, Yoshiyuki Narumiya “Risk Assessment Strategy for Decommissioning of Fukushima Daiichi Nuclear Power Station” *Nuclear Engineering and Technology* Volume 49, Issue 2, (March 2017)
- [189] Yamano et al.,1995, Phenomenological studies on melt-coolant interactions in the ALPHA program. *Nucl. Eng. Des.* 177,369–389.
- [190] J. Yang, D. Y. Lee, S. Miwa, and S.W. Chen “Overview of Filtered Containment Venting in Nuclear Power Plants in Asia” *Annals of Nuclear Energy*, Vol. 119 (2018), pp. 87-97.
- [191] Yang et al., 1987, Solidification effects of the fragmentation of molten metal drops behind a pressure shock wave. *J. Heat Tran.* 109, 226–231.
- [192] Zhang et al., 2009, Fragmentation of a single molten metal droplet penetrating sodium pool I copper droplet and the relationship with copper jet. *J. Nucl. Sci. Technol.* 46, 453–459.

- [193] Zuckerman N., Lior N., Jet Impingement Heat Transfer: Physics, Correlations and Numerical Modeling, *Advances in Heat Transfer*, 2006, vol 39, p 565-631.